UC San Diego

UC San Diego Electronic Theses and Dissertations

Title

Bays and Bivalves: Circulation of Low-inflow Estuaries and Impacts on Oyster Communities in Southern California

Permalink

https://escholarship.org/uc/item/0xt0t04x

ISBN

9798173723536

Author

Anidjar, Niv Orent

Publication Date

2026-11-03

Peer reviewed|Thesis/dissertation

eScholarship.org Powered by the California Digital Library
University of California

UNIVERSITY OF CALIFORNIA SAN DIEGO

Bays and Bivalves: Circulation of Low-inflow Estuaries and Impacts on Oyster Communities in Southern California

A dissertation submitted in partial satisfaction of the
requirements for the degree Doctor of Philosophy

in

Oceanography

by

Niv Orent Anidjar

Committee in charge:

Professor Sarah N Giddings, Chair
Professor Patty Ahn
Professor Morgan Levy
Professor Luke P Miller
Professor BT Werner

2026

Copyright

Niv Orent Anidjar, 2026

All rights reserved.

The Dissertation of Niv Orent Anidjar is approved, and it is acceptable in quality and form for publication on microfilm and electronically.

University of California San Diego

2026

DEDICATION

Thank you to my human and more-than-human friends and family. To the sand that gets in my socks when I walk on the beach. To the lingering light that shines through the shoaling waves at sunset. To the moon that turns the tides.

EPIGRAPH

You don't need a weatherman
to know which way the wind blows

Bob Dylan, "Subterranean Homesick Blues" (1965)

TABLE OF CONTENTS

Dissertation Approval Page iii

Dedication iv

Epigraph v

Table of Contents vi

List of Figures viii

List of Tables xi

Acknowledgements xii

Vita xiii

Abstract of the Dissertation xiv

Introduction 1

Chapter 1 Behavioral Response of Oyster Valve Gape to Ecological Conditions in an Intermittently Closed Estuary 9
1.1 Introduction 10
1.2 Methods 13
1.2.1 Field Site 13
1.2.2 Instrumentation 15
1.2.3 Data Analysis 17
1.3 Results 22
1.3.1 Distributions of Oyster Valve Gape and Environmental Time Series 22
1.3.2 Spearman Correlations 27
1.3.3 Solar Phase Distributions 30
1.3.4 Tidal Phase Distributions 31
1.3.5 Joint Distributions 33
1.3.6 Multivariate Models 35
1.4 Discussion 38
1.5 Conclusions 43
1.5.1 Funding 43
1.6 Authors' Contributions 44
1.7 Acknowledgements 44

Chapter 2 Seasonally Inverse Tidally-Averaged Circulation in a Low-Inflow Estuary . 46
2.1 Introduction 46
2.2 Methods 49
2.2.1 Study Site Description 49

2.2.2 San Diego Bight Model . . . 49
2.2.3 Analysis . . . 52
2.3 Results . . . 55
2.3.1 Validation . . . 55
2.3.2 Environmental Conditions . . . 61
2.3.3 Longitudinal Property Structure . . . 62
2.3.4 Estuarine Total Exchange Flow and Transport-weighted Properties . . . 66
2.3.5 Circulation Strength . . . 69
2.4 Discussion . . . 71
2.4.1 Physical Interpretation . . . 71
2.4.2 Implications for Climate Variability . . . 72
2.4.3 Future Work . . . 73
2.4.4 Applications for SDB Management . . . 74
2.4.5 TEF Numerical Issues in LIEs . . . 74
2.5 Conclusion . . . 75
2.6 Acknowledgements . . . 76

Chapter 3 Recruitment and Residence in San Diego Bay . . . 77
3.1 Introduction . . . 78
3.2 Methods . . . 80
3.2.1 Study Sites . . . 80
3.2.2 Data Collection . . . 81
3.2.3 Recruitment Data Analysis . . . 85
3.2.4 San Diego Bight Model Setup and Validation . . . 86
3.2.5 Lagrangian Particle Tracking . . . 86
3.2.6 Residence Time . . . 87
3.2.7 Recruitment and Residence Time . . . 89
3.3 Results . . . 90
3.3.1 Oyster Recruitment . . . 90
3.3.2 Residence Times . . . 96
3.4 Discussion . . . 97
3.4.1 Recruitment Temporal Variability . . . 97
3.4.2 Recruitment Spatial Variability . . . 98
3.4.3 Residence Time Interannual Variability . . . 99
3.5 Conclusion . . . 99
3.6 Authors' Contributions . . . 100
3.7 Acknowledgements . . . 101

Chapter 4 Conclusion . . . 102

Bibliography . . . 106

LIST OF FIGURES

Figure 1.1. Maps and schematics of Los Peñasquitos Lagoon (LPL) study site. 15

Figure 1.2. Time series and distributions of *Crassostrea gigas* valve gape. 24

Figure 1.3. Time series of 30 minute processed environmental variables measured in or near to Los Peñasquitos Lagoon from late November 2019 through April 2020. 25

Figure 1.4. Time series of 30 minute processed data from the LPL mooring from late November 2019 through April 2020. 26

Figure 1.5. Cross correlations between each oyster valve gape time series and each environmental variable at the tidally averaged time scale in LPL. 28

Figure 1.6. Cross correlations of the high-frequency (shorter than tidally averaged, longer than 30 minute processed) residuals of the tidally averaged time series of oyster valve gape and each environmental variable in LPL. 29

Figure 1.7. Cross correlations of the 30 minute processed time series of oyster valve gape and each environmental variable in LPL. 30

Figure 1.8. Top panel: solar phase distributions of oyster valve gape fraction in LPL. . 31

Figure 1.9. Top panel: tidal phase averaged oyster valve gape in LPL. 33

Figure 1.10. Joint distributions of median oyster valve gape as a function of salinity and oxygen in LPL. 35

Figure 1.11. Model learning curves, showing six different skill metrics for each of the four models as a function of the training dataset length. 37

Figure 1.12. Top panel: model predictions for February 29 2020 through April 9 2020 of 6-hour half-Hamming filtered mean surface oyster valve gape fraction, trained on 70% of time series (December 26 2019 - February 28 2020). . . 38

Figure 2.1. A Map of the portion of the San Diego Bight model bathymetry around San Diego Bay. 51

Figure 2.2. Tidally filtered observed and modeled **(a)** temperature , **(b)** salinity, and **(c)** water level. Observations are shown at the four locations labeled in Fig. 2.1, along with co-located model values. 57

Figure 2.3. Tidally averaged observed and modeled velocities at the channel and shoal moorings shown in Fig. 2.1**(a)**. 59

Figure 2.4. Comparison of modeled (in light blue) and observed (in dark blue) tidal constituents at the NOAA monitoring station on the northeast side of SDB. 60

Figure 2.5. Relevant environmental variables over the three year model period. 61

Figure 2.6. Monthly median freshwater transport [$m^3 s^{-1}$] in model years 2017 through 2019. The shaded areas show the 75th and 25th percentile for each month. 61

Figure 2.7. Cross-sectionally averaged modeled water properties (**(a)** salinity, **(b)** temperature, **(c)** density), and **(d)** compensation ratio c, over the three year model period. 62

Figure 2.8. Average modeled water properties (**(a)** and **(b)** salinity, **(c)** and **(d)** temperature, **(e)** and **(f)** density) along the thalweg over two time periods. 64

Figure 2.9. Time series of quantities at the mouth (section 1) of SDB. 66

Figure 2.10. Differences between inflowing and outflowing transport-weighted mean properties (**(a)** salinity, **(b)** temperature, **(c)** density), and **(d)** inward volume transport for model years 2017-2019. 67

Figure 2.11. Time mean inward and outward volume transport through each SDB cross section for four exchange conditions. 70

Figure 2.12. Maximal exchange (tidal inflow rate) against inward volume transport for SDB model cross sections 1 (panel **(a)**) and 15 (panel **(b)**). 71

Figure 3.1. Yearly average recruitment density at each deployment site for *M. gigas* (blue) and *O. lurida* (orange), shown on a map of SDB, alongside environmental data sources. 82

Figure 3.2. Images of oyster recruitment field setup. 83

Figure 3.3. Map of a subset of the model domain showing SDB. 88

Figure 3.4. Particle release time for all three years (2017, blue; 2018, yellow; 2019, green) with respect to the tide. 89

Figure 3.5. Comparison of summer (April-September) modeled surface temperature (left) and salinity (right) for years 2017 through 2019 at the five recruitment sites. 90

Figure 3.6. Recruitment density by site over time. Each row corresponds to a site (labeled on Fig. 3.1), ordered top to bottom from closest to SDB's mouth to furthest. 92

Figure 3.7. Environmental variables in and near SDB, showing seasonal median values (April - September, recruitment tile deployment season, solid black lines; November - February, previous winter season, dashed black lines) and interquartile ranges (IQRs, vertical bars). 94

Figure 3.8. Residence curves showing the percent of particles from each bin (as labeled in Fig. 3.3, with bin 1 closest to the mouth, and bin 15 at the head) still remaining inside the bay. 96

Figure 3.9. Residence times **(a)** τ_{full} and **(b)** τ_{bin} for years 2017 (solid blue), 2018 (dashed yellow), and 2019 (dotted green) as a function of along-channel distance from SDB's mouth. 97

LIST OF TABLES

Table 2.1. Skill scores for modeled temperature, salinity and water level, co-located with data sources. Skill scores for the hourly values are given along with scores for the tidally filtered values in parentheses. 57

Table 2.2. Validation of the principal axis model velocities co-located with each ADCP deployment. 58

Table 3.1. Recruitment tiles by year and site. Each cell lists the tile count at each tidal elevation deployed at that site that year. 84

Table 3.2. Linear regressions of each median predictor against log transformed *M. gigas* and *O. lurida* recruitment densities. 95

Table 3.3. Linear regressions of each IQR predictor against log transformed *M. gigas* and *O. lurida* recruitment densities. Values for *O. lurida* are shown in parentheses in each cell. Relationship column shows the sign of the fit. Asterisk and bold denote $p < 0.05$. 95

ACKNOWLEDGEMENTS

I would like to acknowledge Professor Sarah N Giddings for her support as my advisor. Thank you for your kindness and support, as well as your understanding of life in all of its complexities and interconnectedness.

I would also like to acknowledge all current and former members of the Giddings Lab. All of you have helped me stay focused, sane, and thoughtful. Special thanks in no particular order to Victoria Boatwright, Helen Zhang, and Sierra Byrne, and Alex Simpson, for your friendship, your care, and your critical feedback.

Chapter 1, in full, is a reprint of the material as it appears in Estuaries and Coasts, 2026. Anidjar, Niv; Giddings, Sarah N.; Neira, Carlos; Sugihara, George; Levin, Lisa A.; Goodrich, Kristen A.; Crooks, Jeff; Wheeler, Duncan; McCormick, Lillian R.; Miller, Luke P., https://doi.org/10.1007/s12237-026-01759-6. The dissertation author was the primary investigator and author of this paper.

Chapter 2, in full, is currently being prepared for submission for publication of the material. Anidjar, Niv; Giddings, Sarah N.; Rodriguez, Angelica. The dissertation author was the primary investigator and author of this material.

Chapter 3, in full, is currently being prepared for submission for publication of the material. Anidjar, Niv; Giddings, Sarah N; Zacherl, Danielle C.; Bowers-Doerning, Chelsea M. The dissertation author was the primary investigator and author of this material.

VITA

2019	Bachelor of Science in Oceanic and Atmospheric Sciences, University of California San Diego
2024	Master of Science in Oceanography, University of California San Diego
2026	Doctor of Philosophy in Oceanography, University of California San Diego

PUBLICATIONS

Anidjar, N., Giddings, S. N., Neira, C., Sugihara, G., Levin, L. A., Goodrich, K. A., Crooks, J., Wheeler, D., McCormick, L. R., & Miller, L. P. (2026). Behavioral Response of Oyster Valve Gape to Ecological Conditions in an Intermittently Closed Estuary. Estuaries and Coasts, 49(6), 175. https://doi.org/10.1007/s12237-026-01759-6

Harding, K. J., Nagarkar, M., Wang, M., Ramsing, K., **Anidjar, N.**, Giddings, S., Brahamsha, B., & Palenik, B. (2025). Temporal and Spatial Dynamics of Synechococcus Clade II and Other Microbes in the Eutrophic Subtropical San Diego Bay. Environmental Microbiology, 27(2), e70043. https://doi.org/10.1111/1462-2920.70043

ABSTRACT OF THE DISSERTATION

Bays and Bivalves: Circulation of Low-inflow Estuaries and Impacts on Oyster Communities in Southern California

by

Niv Orent Anidjar

Doctor of Philosophy in Oceanography

University of California San Diego, 2026

Professor Sarah N Giddings, Chair

Many estuaries in the Mediterranean climate of Southern California are low-inflow estuaries (LIEs), where minimal freshwater input only intermittently drives the buoyancy gradient. LIEs therefore have circulation structures and ecological communities distinct from classical estuaries, and face stressors including mouth closure from sill buildup, and slow flushing pollution. This dissertation characterizes the biological and hydrodynamic components of two Southern California LIEs, Los Peñasquitos Lagoon (LPL) and San Diego Bay (SDB). In LPL, *in situ* oyster valvometry and environmental observations distinguished the behavior of near-surface and near-bottom *Magallana gigas* oysters on tidal, diurnal, and tidally averaged time scales.

Near-surface oysters responded strongly to salinity and dissolved oxygen, opened and closed in phase with solar insolation, and closed consistently during low tides, whereas near-bottom oysters responded weakly to measured variables, with a lagged response to insolation and a weak response to tidal phase. In SDB, a high-resolution hydrodynamic model of the tidally averaged exchange flow verified previously observed salinity and temperature regimes and revealed their seasonally varying circulation. During summer, SDB exhibited classical thermally driven circulation near the mouth, with warm outflows over colder bottom inflows, and inverse circulation near the head, with salty bottom outflows. Fall cooling drove entire-bay inverse circulation, broken by late winter and spring river flows driving entire-bay classical circulation. These circulation cells are sensitive to atmospheric forcing; the dry year 2018 showed only brief classical circulation compared with wetter years. Lagrangian particle tracking then resolved spatial and interannual variability in SDB residence times, which was compared with a decade of oyster recruitment observations and environmental records. Recruitment increased toward the estuary head, consistent with headward increases in temperature, salinity, and residence time. Residence times were longest near the head in 2018, approximately double those of 2017 and 2019. Recruitment was significantly related to median air temperature, wind speed, sea surface temperature, and coastal upwelling. This work advances understanding of biophysical interactions and hydrodynamic processes in LIEs, with relevance to estuary management in San Diego and to coastal communities generally.

Introduction

Estuaries are sites of indistinct boundaries. Land and water mix, blurring and warping the coastline. Freshwater and salt water layer and coalesce, obscuring where rivers end, and oceans begin. Where exactly the estuary is, is never completely clear, and instead they are defined by their dynamical transitions: shifting gradients of salt and life.

Low-inflow estuaries (LIEs) are systems at the edge of our understanding of estuaries. LIEs are a class of globally distributed and understudied estuaries where the effects of river input can be outweighed by the effects of heating, evaporation tidal mixing, wind, and wave forcing (Largier et al. 1997; Largier 2023). This can result in complex circulation structures and density gradients defined by both salinity and temperature that can vary on tidal, seasonal, and interannual timescales (Nidzieko and Monismith 2013). Because of this, LIE hydrodynamics are not well described by classical estuarine physical theories (Geyer and MacCready 2014).

LIEs exist worlwide in Mediterrenean climates (Largier 2023; McSweeney et al. 2017). Southern California contains numerous LIEs that are both physically dynamic and ecologically important (Southern California Wetlands Recovery Project 2018). Among these, Los Peñasquitos Lagoon (LPL) and San Diego Bay (SDB) are especially useful study systems at opposite ends of the range of characteristics displayed by Southern California LIEs. LPL is a small ($\sim 2\ km^2$) intermittently closed estuary (ICE) that has been designated as a California State Marsh Natural Preserve. Its hydrodynamics have been well described (e.g., Harvey et al. 2020, 2023a), and are strongly impacted by persistent year-long urban runoff, and sill accretion and occasional mouth closure due to weak stream flow and wave-driven sediment transport. While the urban discharge inputs are very small ($< 1 m^3 s^{-1}$), LPL's small size is such that this weak inflow is

enough to drive a classical estuarine circulation state with tidally varying stratification most of the year (Harvey et al. 2023a). SDB is a larger, hypersaline LIE ($\sim 50\ km^2$), with a heavily altered shoreline, and small pockets of marshes and mudflats. There has been significant research into its hydrodynamics (e.g., Largier 1995; Chadwick et al. 1996; Chadwick and Largier 1999a; Rodriguez 2019) which have shown it experiences complex longitudinal density structures including hypersalinity near the head and thermal dominance near the mouth (Largier 1995; Chadwick and Largier 1999a). It is strongly tidal and vertically well-mixed such that existing numerical models have been focused on 2D, depth-averaged circulation (e.g., Shrestha et al. 1997; Chu and Kyriakidis 2011). However, due to the extent of its historical and contemporary pollution, as well as its continually changing and expanding usage (managed by the Port of San Diego and the U.S. Navy), there exists demand to characterize its three-dimensional circulation in greater detail.

These hydrodynamic characteristics in turn shape LIE ecosystems. Oysters are foundational estuarine species that are sensitive to shifting environmental conditions. As sessile, reef-forming filter-feeding bivalves, oysters not only respond to their environment, but also construct it. They provide habitat for other organisms, limit shoreline erosion, and support fish and bird populations (Beck et al. 2011). As such, their population and behavioral dynamics are effective indicators of ecosystem health. Temperature, salinity, tidal elevation, residence time, and oxygen availability can all influence recruitment, growth, survival, and behavior. In LIEs, where these conditions may change rapidly over tidal and seasonal time scales, oysters must respond to dynamic conditions that can either promote community success, or result in mortality and population collapse.

The two oyster species in Southern California LIEs have demonstrated significant responses to changing conditions across the west coast of North America. The native *Ostrea lurida* has faced overharvesting and habitat loss in the past two centuries, while the invasive feral *Magallana gigas* which was initially introduced for aquaculture, has become well established in the region since the mid 20th century (Wolfe et al. 2024; Padilla 2010). Both species

exist together, although with different distributions and responses to environmental conditions. Understanding under which conditions these oyster populations succeed requires linking the behavioral responses and population dynamics to the broader circulation patterns and environmental variability that characterize LIEs.

This thesis aims to understand the hydrodynamics and ecological dynamics of oysters in LIEs, as well as how these two components interact. Chapter 1 relates oyster valve gape behavior (shell opening and closing measured at high frequency) to physical environmental conditions on tidal and subtidal time scales in LPL. This chapter and its associated peer-reviewed publication constitute the first published analysis of oyster valvometry in the context of a intermittently closed LIE. Chapter 2 focuses on the hydrodynamics of SDB alone, on subtidal and seasonal timescales, to characterize its temporally and spatially varying longitudinal circulation and ocean-estuary exchange. This chapter provides the first examination of the highly resolved time-varying circulation structure of SDB, and provides insight to other hypersaline LIEs that exist globally. Chapter 3 brings these two components back together, to examine the water residence times and other environmental conditions in SDB, and relate them to spatial and interannual variability in oyster recruitment (an integrated measure of larval settlement and survival) over the course of a decade. This chapter presents the first evidence of interannual variability in SDB residence times, and analysis of the longest existing time series of oyster recruitment in SDB. As a whole, this work advances understanding of hydrodynamics and biophysical interactions in low-inflow estuaries, with high relevance to estuary management issues such as pollution, eutrophication, water quality, ecosystem health, and restoration.

A Brief Reflection on Context

While researching and writing this thesis, I have also engaged in reflexive study of the context of my work (Nader 1972; Harding 1992). I have wondered, and sought to address specifically the question of where we draw the boundary of the dynamics that are included in

our analyses of estuarine systems, which dynamics are excluded from our analyses, and to what ends these boundaries serve. These questions follow from work in the discipline of science and technology studies, where the practice of drawing boundaries between society and nature is recognized as part of the scientific process (Jasanoff 2004; Felt et al. 2017). In pursuit of this, I have given particular attention to historical and contemporary management documents of SDB. Despite not doing a comprehensive review of all documents (I completely ignored the Spanish and Mexican periods), I did notice some patterns.

SDB has struck me as a place defined by destruction. It was the site of the first recorded European landing on the west coast of what became the United States (Wagner 1929). Over 70% of the salt marsh and over 80% of mudflats have been buried (Stein et al. 2014; Touchstone et al. 2021). There is more than a century of documented water pollution, including raw sewage, copper, mercury, DDT, tributyltin, PCBs and PAHs (Port of San Diego 1980; U.S. Department of the Navy, Naval Facilities Engineering Command Southwest and Port of San Diego 2013; Peeling 1975; Chadwick et al. 2004; Sarabia et al. 2024; Neira et al. 2018; Grovhoug et al. 1986; California Regional Water Control Board, San Diego Region 2012; National Research Council 1990). It is the current site of one of the largest Navy bases in the world, and it has been included on the EPA 303(d) list of impaired water bodies since at least 1990 (Water Resources Control Board State of California 1990; Torres 2024).

Over roughly the last 50 years, the management literature has largely shifted focus to environmental stewardship, preservation, conservation, and restoration. There is broad acknowledgement of ”legacy” pollution, habitat reduction, and the need to protect the environment. However, the extent of SDB restoration today is minimal in comparison to estimates of historical habitat size (Grossinger et al. 2011; U.S. Department of the Navy, Naval Facilities Engineering Command Southwest and Port of San Diego 2013; Stein et al. 2014; Touchstone et al. 2021; Planning and Environment Division 2024). It seems to me that instead of approaching some full restoration of the physical land and water which we call San Diego Bay, management bodies now work to maintain and stabilize SDB in its current form: post dredging, post infilling, post

river damming and diversion. A boundary was set in time that defines what SDB is and can be. What is maintained is not a purely physical structure spatially bounded by the waterline and bay mouth. Rather, as Mike Davis puts it in his book *Under the Perfect Sun: the San Diego Tourists Never See*, SDB is "a social artifact", co-constituted by the management structures and physical processes of the system.

The development and maintenance of this system have been accomplished in no small part with oceanographic work (although, not always by workers bearing the title "oceanographer"). In the late 19th century, for example, the construction of Zuniga Jetty followed observations that a jetty would increase tidal velocities, increasing scouring and deepening the channel, and blocking sediment transport from the south (U.S. Congress 1968; Martin 2017). The "improvement" of the bay through dredging was justified to the federal government with surveys of tides and bathymetry (see Letters from the Secretary of War Garrison (1916); Dern (1934); Stimson (1941) as well as U.S. Congress (1968)). In more recent years, oceanographic research has been a critical component of management planning documents, such as the San Diego Bay Integrated Natural Resources Management Plan, and the Strategy for a Healthy San Diego Bay, providing monitoring of physical, chemical, and biological changes to inform restoration strategies (U.S. Navy 2013b; Cheng and Nagoda 2015).

That monitoring is part of a restoration practice that rarely reproduces historical land and water configurations. "Success criteria" are typically functional, based on the "maximization" of properties such as pollutant removal, ecosystem productivity, potential carbon sequestration, or species richness and density (Williams and Zedler 1999; Zedler and Callaway 2000; San Diego Unified Port District and City of Chula Vista 2016; ESA Associates and Merkel & Associates 2022; U. S. Department of the Navy 2024), rather than on restoration to pre-colonial habitat (Zedler and Stevens 2018; Robinson et al. 2021). Restoration sites are often built to precise specifications, producing configurations that have never previously existed in SDB. In some cases, this is done in order to extract as much measurable benefit as possible from small areas, e.g., the site of the San Diego Bay Eelgrass Mitigation Bank was chosen in part based on maximizing

a ”credit yield” to quantitatively evaluate the potential ”functional lift” of restoring each site (Robertson 2000; Huff and Brock 2023; U. S. Department of the Navy 2024).

The same reasoning is used for restoration accounting. Restoration is increasingly done in the framework of mitigation banking, where a rule of ”no net loss” of habitat enables trading of restored land in one place for destruction elsewhere through fungible credits (e.g., Chula Vista Waterfront, and Pond 20 (Unified Port of San Diego 2010; Smith 2018)). Recent political ecology scholarship describes this as part of a broader pattern in which damaged nature becomes a new opportunity for profit rather than a limit on it, where biodiversity and carbon credit markets tend to reinforce the growth they are supposed to moderate (Huff and Brock 2023; Moranta et al. 2022). This accounting functions relative to a contemporary baseline, rather than to a pre-colonial social and environmental status, and some habitat losses in SDB are described as ”unavoidable” (Planning and Environment Division 2024). Because of this contemporary baseline, sites that have already sustained extensive damage sometimes face lower regulatory red tape for further destruction (e.g., new environmental analysis was avoided for unexploded ordnance-laden dredge spoils from SDB in 1998 by disposing of them at the pre-existing offshore dumping site LA-5) (Cotter and Cunniff 1987; EPA 1991; California Coastal Commission 1998; Pierce et al. 2001).

As I interpret it, components of the SDB system such as Naval Base San Diego and the Port of San Diego Shipyards are therefore naturalized and externalized from the environment. The base’s mission capabilities and land area are subject to the same ”no net loss” requirement as habitat (U.S. Navy 2013a; sik 1960), and while the Port makes some effort to ”minimize substantial adverse environmental impacts,” it ultimately assigns ”highest priority” land use to ”port purposes” (Planning and Environment Division 2024). The sites of the base and shipyards are therefore unlikely to be considered for restoration, and their persistence is never really discussed, just assumed. I read this as a significant part of what accounts for the disparity between restoration extent and historical habitat extent. The footprint of restoration in SDB is small at one level because of the cost and complexity of implementation, but at another, I

argue, because its function is to stabilize a capital and colonial centered structure. This view is in line with political ecology critiques of mitigation banking (Robertson 2000; Huff and Brock 2023). Restoration of this kind requires the measurements and analyses of oceanographers, which contribute to a precise accounting of an area's (exchangeable) ecosystem services.

The continuity of development and maintenance has been stated directly since early surveys. In his 1908 *History of San Diego*, William E. Smythe quotes the superintendent of The United States Coast Survey, Commodore C. P. Patterson on SDB.

> Ample accommodations can be had in this harbor for a very large commerce. There is no safer harbor on the Pacific Coast for entering or leaving, or for vessels lying off wharves. . . . from a national point of view, its importance is so great that its preservation demands national protection and justifies national expenditure. Fortunately, these expenditures need not be great, if the stable regimen of the harbor be preserved (Smythe 1908).

There is no clearer illustration of the unity of the development and maintenance phases of the SDB system. Patterson is describing preservation of a thing that does not yet exist: the optimal harbor for commercial and national interests. Patterson's "stable regimen" is therefore the entire process of optimizing SDB. Development and maintenance are one activity, differentiated only by how much work remains. Our discipline's role in the construction of SDB was to make the physical land and water coincide with that conception, which required the destabilization of the land and water as they once were under Indigenous Kumeyaay stewardship. Because of the co-constitution of the SDB system by management and physical structures, restoration appears to require altering the management structures as much as the physical ones.

These issues with contemporary restoration practice are not unique to SDB, and alternative approaches have been discussed, and in some cases implemented, elsewhere (Robinson et al. 2021). Some approaches focus on restoring a site's physical processes, removing or altering the infrastructure that blocks them, and allowing the site to develop into its own configuration over time rather than building to a fixed design (Williams et al. 2009; Griggs and Patsch 2019). Other approaches favor bringing affected communities into decisions through consultative forms of

co-production (Thornton and Scheer 2012; Mistry and Berardi 2016; Bremer and Meisch 2017). In each case, western science is used to figure out what the current conditions at a site are, and where they are headed. While those approaches involve maintaining contemporary management decision making structures, others specify that restoration also requires changing who holds authority over management decisions. In particular, they distinguish between including Indigenous knowledge in planning stages, and ceding decision making authority over the environment (Senos et al. 2006; Gomez 2024; Sylman et al. 2026).

In my investigation of this literature, it appears that the unceded land and water beneath the colonial wrapper of SDB cannot be restored without the return of the rights to that land and water to the Kumeyaay. This decolonization would require ”the repatriation of Indigenous land and life... all of the land, and not just symbolically” (Tuck and Yang 2012; O’Donnell 2023). Restoration of SDB without decolonization seems to me unable to revitalize the system into a state which is not dominated by the military and commercial usage, but instead reflects relations of kinship and reciprocity with the land and water (Senos et al. 2006).

The chapters that follow are themselves conventional oceanography, studying hydrodynamics and oysters in San Diego’s estuaries entirely within the methods of western physical and biological science. The above reflection is provided alongside the chapters so that the work in this thesis can be read in the context of its complex and intersecting scientific and social boundaries.

Chapter 1

Behavioral Response of Oyster Valve Gape to Ecological Conditions in an Intermittently Closed Estuary

Abstract: Low-inflow estuaries are highly variable and productive habitats. Organisms in these systems must cope with constantly changing conditions. This study investigates the continuous response of oysters to environmental stimuli in a small, low-inflow, estuary, Los Peñasquitos Lagoon (LPL), in San Diego, California, USA. The oysters were placed on a mooring at near-surface and near-bottom locations and instrumented with noninvasive sensors to measure their shell opening (oyster valve gape), concurrently with physical and chemical measurements (water depth, salinity, temperature, dissolved oxygen, pH, solar radiation, wind velocity, and wave radiation stresses) over 136 days. The time series of each oyster with each variable over tidally averaged and shorter time scales were analyzed using traditional statistical methods. The strongest gape relationships were with salinity and dissolved oxygen (Spearman correlation coefficient 0.6), among the oysters near the water surface. Diurnal phase averaging showed how the surface oysters open and close in phase with insolation, while the near-bottom oysters have a lagged response. Tidal phase averaging further illustrates the distinct gape behavior, with surface oysters closing consistently during low tides, and bottom oysters generally remaining open. A subset of variables that had high Spearman correlations (near surface oxygen and salinity, near-bottom pH, solar irradiance, and near-bottom turbidity) and their 18-hour time lags were used to test a set of multivariate models for predicting surface oyster valve gape. The best performing model ($r^2 = 0.75$) was consistent with the correlation analysis, showing salinity and dissolved oxygen to be the most important predictors. Key insights from this study are that oysters in LPL have predictable responses to environmental conditions (particularly salinity and dissolved oxygen) with differing responses to conditions near-surface and near-bottom on tidal and tidally-averaged, and faster

than tidal timescales.

1.1 Introduction

Estuaries have consistently been cited as one of the most economically valuable ecosystems (Costanza et al. 1997; de Groot et al. 2012; Costanza et al. 2014). In the United States, eight of the ten largest metropolitan areas are in regions bordering estuaries, comprising 40% of the nation's population (Rouleau et al. 2021). Estuaries are sensitive to changes in climate which alter forcing from the atmosphere, ocean and upstream end members, while at the same time are subjected to significant direct human modifications. In order to mitigate the negative effects of human modifications, significant management and restoration projects have been implemented in impacted estuaries (Kennish 2004; Fuentes et al. 2020; Walker et al. 2025). Monitoring estuarine conditions in a cost effective and accessible manner is necessary for making such management decisions and implementing successful restoration plans (Roegner et al. 2008).

Low-Inflow estuaries (LIEs) are estuaries with minimal or intermittent freshwater input that exist worldwide in Mediterranean climates (Largier 2023). Many of these LIEs experience a wide range in environmental and water quality conditions due to multiple compounding factors including the potential for hypersaline conditions and inverse or weak circulation (Largier 2023). Many also experience significant mouth morphological changes including intermittent inlet mouth closure (intermittently closed estuaries, ICEs) during times of high waves and low freshwater flow (Behrens et al. 2013; McSweeney et al. 2017; Orescanin and Scooler 2018). During times of weak or no circulation, poor water quality, including build up of pollution and development of hypoxia can occur (Harvey et al. 2023b; Gale et al. 2007; Cousins et al. 2010).

Southern California LIEs and ICEs face a multitude of stressors and are heavily managed to avoid negative human and ecosystem consequences (for example, hypoxia, flooding, and mosquito breeding during inlet closures) (e.g., Elwany 2011). The patchwork of entities operating at different scales (e.g., local, state, regional, and federal), combined with divergent management

objectives (e.g., ecological protection versus infrastructure maintenance), monitoring systems, and sensor networks, complicates the management landscape (Pratt 2014; SANDAG 2025). Regional environmental managers have expressed a need to better understand when water quality conditions pose direct risks to biotic communities. In this context, biosentinels offer the potential to augment existing monitoring data and strengthen estuary management decision-making across these systems. (Southern California Wetlands Recovery Project 2018; Walker et al. 2025).

Often, environmental management bodies deduce biological dynamics from physical measurements and sparse biochemical measurements that involve slow benchtop analyses or single-use tests. Chemical water quality analysis can be expensive. Bae and Park (2014) note that the average cost to analyze 126 US EPA pollutants is $1000 per sample, and monitoring ecosystems at population and community levels can be slow (e.g., counting individuals). Comprehensive chemical analysis of all potential environmental toxins is not always possible (Bub et al. 2025). However, living organisms respond to a range of chemical and physical stimuli, through changes in behavior and physiological processes to maintain homeostasis. By measuring and describing behavioral and physiological variability, we can diagnose unusual behavior indicative of a change in the environment, possibly undetected by conventional sensors, or indicative of multi-stressors. Oysters are one organism that can act as these 'biological early warning systems' (BEWS) where patterns in their behavior (e.g., valve gape) reflect their health, possible stress, and response to their environment. BEWS have been used around the world (e.g., France, Germany, USA, China, Japan, and Korea) to monitor water quality through the behavior of individual organisms. BEWS have involved observing bacterial growth, algal fluorescence, plankton movements (e.g., *Daphnia*), fish movements, and bivalve behavior (Bae and Park 2014). Sessile bivalves such as oysters are well suited as the basis for BEWS, due to their sensitivity to and bioaccumulation of contaminants, as well as their easy manageability in comparison with mobile organisms (Vereycken and Aldridge 2023). Bivalves have been used to monitor water quality at least since the early 20th century with the work of Marceau (1909), and have been used for monitoring drinking water supplies in some locations (de Zwart et al. 1995;

Borcherding 2006). Bivalves are known to respond with their valve gape behavior to a broad set of environmental chemical changes including salinity, dissolved oxygen (DO), pH, copper, uranium, and toxic algae (Fournier et al. 2004; Tran et al. 2004, 2007, 2010; Porter and Breitburg 2016).

The goal of this study is to investigate the continuous response of oyster valve gape to environmental stimuli in a small, low inflow, intermittently closed estuary subject to a wide range of conditions, providing baseline data for oyster valve response in an LIE and ICE. The study site is Los Peñasquitos Lagoon (LPL), a LIE and ICE located in San Diego, California, USA. Using an open source hardware and software system described in Miller (2022), *Crassostrea [Magallana] gigas* oysters in LPL were instrumented with noninvasive sensors to measure their shell opening (oyster valve gape) over time, concurrently with physical and biogeochemical measurements. The oyster monitors, as well as salinity, temperature, depth, and DO sensors were attached to a mooring in the LPL main channel, at two different depths (see Figure 1.1). This vertical resolution allows for a deeper level of analysis not just of the oysters, but of their responses to stratification, which is an essential and well-studied component of estuarine dynamics. The study examined conditional averaging of oyster valve gape over diurnal, tidal, and spring/neap cycles, correlation of the time series of each oyster with each variable at tidally averaged and shorter time scales, and variable joint distributions. Given the relationships found between different environmental variables and nonlinear dynamics observed, we show the potential use of a multivariate function of environmental variables to predict oyster activity.

Compared with previous research involving oyster valvometry in estuaries, this work is a specialized effort at unifying physical oceanographic methodologies with those of behavioral ecology. Examination of organismal response across a very wide range of parameters is made possible by virtue of the estuary type and by having sensors located near-surface and near-bottom across a strongly stratified water column. This work addresses key knowledge gaps by utilizing long, high temporal resolution data, and extensive in-situ co-located environmental and water quality variables. Specifically, we hypothesized and found that:

1. Oysters near the surface have distinct valve gape behavior from oysters near the bottom of the water column, related to water column stratification.

2. Oyster valve gape varies periodically on diurnal, tidal, and fortnightly time scales, and so will have relationships with variables that are also periodic on those timescales due to known physical processes.

3. These relationships may be nonlinear, and correlated with each other, so a qualitative analysis of their joint distributions is necessary to understand to which variables the oysters are directly responding.

4. The majority of oyster valve gape variance can be explained by some time-varying combination of the concurrently measured variables.

1.2 Methods

1.2.1 Field Site

Los Peñasquitos Lagoon (LPL) is a small LIE and ICE in northern San Diego, southern California, USA. The LIE nature and strongly stratified, tidal dynamics of LPL inherently provide a wide range of environmental conditions. The inlet closes at least once seasonally, during which time the conditions respond strongly, including extended periods of hypoxia and overall estuarine freshening (Harvey et al. 2023b). Precipitation, and resulting freshwater runoff, occurs mainly in late winter and early spring, during occasional storms. LPL is shallow, with a maximum depth of approximately 4 meters. The main channel is no wider than 70 meters, and the entire estuary covers about 2 km^2 (Figure 1.1c). The inlet crosses a beach consisting of sand and cobbles. Inlet closures occur mainly during late spring due to accretion caused by large waves coincident with minimal river flow (Harvey et al. 2023b; Elwany 2011). Since 1932, the inlet has been constricted under a bridge as part of the construction of Highway 101 / North Torrey Pines Road, which has led to more frequent closures. LPL is the outlet of a roughly 255 km^2 watershed which includes Carmel Creek, Carroll Creek, and Los Peñasquitos Creek (Figure 1.1b).

Prior to development by western settlers, LPL was a predominantly open estuary. As a result of increased closures caused by the highway berm (originally built in 1915 and modified in 1932) and increased year-round urban runoff, the salt marsh and salt flats of LPL have largely been replaced by brackish wetlands (Beller et al. 2014). These changes have led to increased occurrence and breeding of mosquitos which are vectors for viruses that cause human encephalitis, e.g., the West Nile Virus. Moreover, inlet closures result in rapid hypoxia at depth and upstream flooding risk. The 2015-2016 El Niño led to more frequent and severe mouth closures, indicating that the estuary state is sensitive to climate conditions (Harvey et al. 2020). To maintain ocean-estuary water exchange, and prevent ecological collapse, sediment dredging is performed when the inlet is closed or is near closing. Dredging is done at least once a year, but has been done up to 6 times in one year (2016). The cost of a single dredging is $115,000 to $130,000 (Harvey et al. 2023b; Mike Hastings, personal communication). Each dredging moves between 2,000 and 30,000 m^3 of sediment (Crooks et al. 2019). During the 2020 Southern California harmful algal bloom, following the conclusion of the sensor deployment investigated in this study, LPL suffered a mortality event of fishes and invertebrates, associated with intermittent hypoxia, and abnormally high pH followed by abnormally low pH (Skelton et al. 2024). Mouth management decisions are applied using real-time measurements of dissolved oxygen and water levels as well as other factors such as mosquito presence. Restoration projects in LPL focus on increasing tidal influence and salt marsh in the back of the lagoon (Los Peñasquitos Lagoon Foundation 2018).

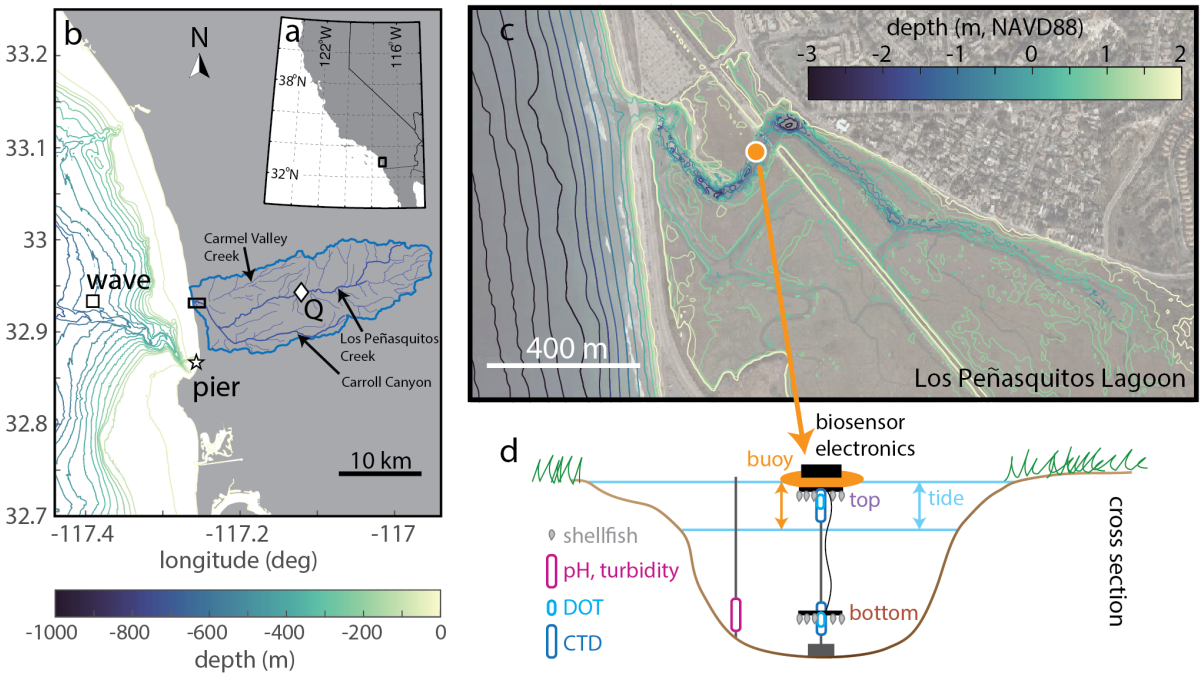


Figure 1.1. Maps and schematics of Los Peñasquitos Lagoon (LPL) study site. **a** Inset map of California, with the study location on panel **b** indicated with a rectangle. **b** Closer view showing the watershed, contours of offshore bathymetry, and locations of the CDIP wave buoy [square], the Ellen Browning Scripps Memorial Pier (NOAA tide gauge, irradiance data [star]), the upstream USGS flow gauge [diamond], and the study site shown in c indicated with a rectangle. **c** Contour map of the LPL topography and nearshore bathymetry overlain on a Google map satellite image. The mooring location is indicated with an orange disc, at approximately $32.93337°N$ and $-117.25716°E$. **d** A schematic of the LPL channel cross section and the mooring. Note that the view is facing upstream, and the pH and turbidity sensors (at the NERR LPL NW station) are by the northwest stream bank offset across the estuary by less than 10m.

1.2.2 Instrumentation

The oyster mooring was deployed in the main estuary channel upstream of the mouth and the first two bends (Figure 1.1c) on November 25, 2019 and recovered on April 9, 2020 (136 days). This deployment period was chosen to monitor the oysters through the winter time when freshwater input is present, and into the spring when there is potential for inlet closure due to sill build up following winter storm waves, all of which are conditions that were likely to cause changes in flow and water quality that might drive animal behavioral responses. Data collection stopped earlier than planned due to water intrusion in the data logger housing. The mooring was redeployed on May 18, 2020 during an inlet closure, however all instrumented oysters died

within 5 days. This second deployment is not included in the main analysis of this study, and is used qualitatively in the discussion section.

The mooring was anchored using lead weights, and the top of the mooring line was attached to a foam boogie board. The total mooring line length was about 5 meters to allow for tidally varying water levels and scope during strong currents. Sensors were attached to the mooring line using hose clamps and zipties. Near-bottom sensors were attached about 0.5 meters above the bottom, suspended by a subsurface float. Near-surface sensors were attached about 0.2 meters below the surface. The water column depth at the mooring varies from around 1 to 2.9 meters with the top/bottom sensors varying from 0.3m apart to 2.2m apart.

On the mooring, both near-surface and near-bottom, was a Seabird SBE 37 CTD to measure salinity, temperature, and depth, and a Precision Measurement Engineering Mini-DOT to measure DO concentration. The CTDs sampled every five minutes. The DO sensors sampled every minute. Sensors were affixed to *Crassostrea gigas* oysters originating from the shallow banks of LPL. This species is non-native, having been introduced sometime after 2005, and was chosen due to its prevalence in this system (Crooks et al. 2015). Ten oysters were deployed, five near the water surface (just beneath a floating platform), and five near the estuary bottom (Figure 1.1d). Two of the near-bottom oysters were not included in the analysis, because one oyster died soon after deployment, and the other oyster's sensor malfunctioned. Oyster shell valve opening and closing was monitored using a Hall effect sensor (A1395, Allegro Microsystems, Manchester NH) and neodymium magnet (6.35 mm diameter, 1.59 mm thick) glued to the opposing shell valves (Wilson et al. 2005; Miller 2022), such that changing distance between the Hall effect sensor and magnet as the shell opened and closed was registered as a changing voltage. Voltage values were recorded by a custom data logging device based on Arduino open-source hardware designs (https://github.com/millerlp/MusselGapeTracker). Raw voltage values were recorded at 5 s intervals, and were converted to estimates of opening distance (units of mm) and then to relative opening (gape fraction, 0 for completely closed to 1 for completely open for each individual oyster) using the methods described in Miller and Dowd (2017). The original 5 second

interval data were decimated to 1 minute intervals for subsequent analysis.

Just northwest of the mooring (less than 10 meters away) is a National Estuarine Research Reserve (NERR) monitoring station which includes pH and turbidity measurements, sampled every 15 minutes near the bed (Station LPL NW, data accessible at http://torreypines.trnerr.org/). Cross-shore and along-shore radiation stresses (S_{xx} and S_{xy} respectively) were sampled hourly from the Coastal Data Information Program (CDIP) monitoring and prediction point offshore of Torrey Pines Beach (site D0587). River flow, sampled every 15 minutes, was obtained from a USGS gauge upstream on Los Peñasquitos Creek (Figure 1.1b). Global horizontal irradiance was obtained from the National Solar Radiation Database's Physical Solar Model version 3, at the nearest spatial bin to the mooring. The model output has a 2 km spatial resolution and a 30 minute temporal resolution. Observed irradiance from the Ellen Browning Scripps Memorial Pier in La Jolla near the field site compared well to this model product, but was not available for the full time series, and so was not used as part of this study. Offshore water level (sampled hourly), wind direction and speed (sampled every 15 minutes), were obtained from the NOAA tide and meteorological station (station ID 9410230) located on the Ellen Browning Scripps Memorial Pier, about 7.5 kilometers south of the mooring (Figure 1.1b).

1.2.3 Data Analysis

Data Preparation

To enable ease of analysis, all time series were cleaned, filtered, and subsampled to 30 minute intervals. Gaps in the oyster valve gape fraction time series, no longer than two hours, were interpolated using an autocorrelation kriging method. Data were 60-minute low pass filtered with a first order Savitzky-Golay filter (to avoid phase shifting and ringing typical of convolution based filters) and then subsampled to 30 minute intervals so that all time series were aligned with uniform time stamps, resulting in 6543 subsamples in each time series. Sub-sampling following filtering produces values that represent 60 minute means of the 1-minute sampled oyster valve gape fraction. The 30-minute processed time series was tidally averaged (using a

low-pass Godin filter described in Godin et al. (1981)) and the higher frequency residual was calculated by subtracting the tidally averaged data from the 30 minute processed data.

Spearman Correlations

To determine which environmental variables may be significant drivers of oyster valve gape behavior, a cross-correlation analysis was performed. Spearman correlation was chosen rather than Pearson correlation because the oyster valve gape data is not normally distributed. Variables with which many of the oysters have similar values of both the lag time of the central peak correlation, as well as their central peak correlation values, are determined to be significant environmental drivers of oyster valve gape behavior. Pairwise Spearman cross correlations between the oyster valve gape fraction time series and environmental data (water depth, insolation, northerly and easterly wind velocity components, pH, turbidity, cross-shore and along-shore wave radiation stresses, river flow, salinity, temperature, and DO) were calculated. Although they may not directly influence one another due to stratification, near-surface oyster valve gape was compared with the near-bottom measurements of pH and turbidity because prior work in LPL, as well as data shown here, indicate that surface and bottom parameters still co-vary due to the strongly tidal nature of the estuary (Harvey et al. 2023b).

Different estuarine processes influence water properties on tidal and tidally averaged time scales, with the tidally averaged time scale relevant to the residence time of nutrients and pollutants (Geyer and MacCready 2014). For this reason, the cross-correlation analysis was performed for the tidally averaged and high-frequency residual (i.e., tidal and higher) separately, as well as for the full 30 minute processed data (to determine the overall most correlated variables). The most consequential peak in the cross-correlation, chosen between the two prominent peaks around a lag of zero, was chosen as the central peak correlation and lag time. Statistical significance of the central peak correlation is defined as the likelihood that this lag would still be the central peak given another random sampling of the data. This significance was calculated using a Monte Carlo surrogate method (N=200). Surrogate data were generated

using a random phase technique, to preserve the spectrum of the measured data.

Phase Distributions

In order to determine the relationships between tidal and diurnal solar cycles and oyster valve gape, and characterize the distinct behaviors of near-surface and near-bottom oysters over these cycles, tidal and diurnal phase distributions of oyster valve gape were calculated. Similarly to Harvey et al. (2023b), tidal phase was defined between two offshore higher-high water levels. Tidal cycles that were not clearly semidiurnal (where a higher high tide was not followed by a lower high tide) were not included (13 tidal cycles). Incomplete tidal cycles at the beginning and end of the oyster deployment were also not included.

Diurnal phase was found from solar irradiance by aligning solar noon and solar midnight from the clearsky GHI provided by the PSM. Distributions of oyster valve gape behavior were determined in 100 phase bins, with respect to these definitions of the tidal, and diurnal phases. All surface oysters and bottom oysters were included in these distributions. This resulted in 122 tidal cycles, and 133 diurnal cycles. The effect of the fortnightly spring neap cycle was examined by splitting the tidal cycles into two even groups (61 cycles each) by tidal range, where the spring and neap groups had mean tidal ranges of 2.11 meters and 1.32 meters, respectively before calculating the phase distribution. These phase distributions were analyzed in lieu of spectral analysis to observe nonlinear and harmonic effects, building on the linear analysis in Tran et al. (2011).

Joint Distributions

To examine the shared influence of two variables on oyster valve gape, three dimensional joint distributions were also generated for near surface and near bottom oysters. The median oyster valve gape in each 2-dimensional bin was calculated to show a typical value of oyster valve gape as a function of these variables. The joint distribution of oyster valve gape with DO and salinity was chosen due to their similar cross correlation coefficients and lag times, as

well as their similar tidal phasing (Harvey et al. 2023b), so the joint distribution can show their conditional relationships. The joint distribution of oyster valve gape with pH and turbidity was similarly chosen due to their similar cross correlation coefficients. In addition, both pH and turbidity were only measured near the bottom of the water column, so further examination of these joint distributions can clarify the significance of their relationships with near surface and near bottom oyster valve gape behavior.

Multivariate Models

In the absence of direct measurements, it would be useful to have a model to predict oyster valve gape as a function of more commonly monitored environmental conditions. Here we test a few nonlinear models and compare them to a linear model. We tested a set of models that most directly tests the hypothesis that oyster valve gape is dynamically dependent on the local state of the environment. Specifically we tested three variations of Empirical Dynamic Modeling (EDM), using k-nearest neighbor (knn) regressor from the scikit-learn Python library, and two models from the pyEDM Python library, namely Simplex and S-Maps (Sugihara and May 1990; Sugihara 1994). Note that all previously described analysis was done using MATLAB however this analysis was done using Python because there is no MATLAB equivalent to these EDM Python libraries. Six skill metrics are used to evaluate the linear and nonlinear models: the coefficient of determination (R^2), root mean square error (RMSE), Willmott skill (Willmott 1981), model bias, Pearson's correlation, and Spearman's correlation.

The theoretical basis for EDM is mechanistic, and only has predictive power when the variables chosen belong to the same dynamical system, and are dynamically causal (Deyle and Sugihara 2011; Sugihara et al. 2012). By choosing the right set of observable environmental variables and their time delays to define an embedding space, the attractor that corresponds to the full dynamics of the system will be reconstructed. This enables accurate prediction of future states by searching for nearest neighbors on this multidimensional attractor. Briefly, the Simplex model calculates the centroid of the nearest neighbors of the prediction point on the attractor as

an estimate of the target point, and the S-Map model calculates a linear regression of the nearest neighbors with the target variable, which provides a slightly different estimate than the Simplex model. We also tested the knn regressor, which uses a different distance weighting for the nearest neighbors (the knn regressor uses an inverse distance weighting, while Simplex and S-Maps use an exponential weighting). These three variations of EDM were chosen because, although oyster valve gape behavior is assumed to be similar when environmental conditions are similar, the type of locality in the state space (distance weighting, local functional relationship) is unknown. Comparison among these variations is necessary to determine the most appropriate EDM model for this dataset. Since S-Maps calculates local linear regressions in the state space of the chosen variables, it also provides predictions of the relative contribution of each variable to predictions of oyster valve gape fraction.

The same embedding was used for all of these models. Filtered valve gape fraction for the surface oysters was predicted as a function of filtered simultaneous measurements of near surface DO and salinity, near-bottom pH, solar irradiance, and near-bottom turbidity, as well as the values of these variables 18 hours previously. This set of variables was chosen based on an assessment of the values of the valve gape-variable cross correlations found previously, as well as the assumption that oyster valve behavior is dynamic, and is therefore a function of previous system states. The lag value was chosen based on the peak lag of the autocorrelation of the mean valve gape fraction of the surface oysters. The number of nearest neighbors used for each prediction was twenty percent of the number of points in the training set. This value was chosen based on a brute force search for the value that gave the best model skill. Valve gape fraction and the predictor variables were filtered using a 6-hour causal half-hamming filter. The data were then subsampled to a 1.5-hour interval. This filtering and subsampling reduced noise and model runtime, respectively, while preserving features on timescales in the data that are known to influence valve gape behavior, such as the diurnal and tidal timescales (Tran et al. 2011). Subsampling additionally ensures that data points are maximally independent, which is particularly important for such a short time series where a rigorous test of the model requires

evaluation of skill metrics on many randomized data shuffles.

If more data collection would lead to better nonlinear models, i.e. the state space is not yet optimally resolved, then we expect that with increasing training library size, nonlinear model skill metrics would continue to improve, while linear model skill would increase more slowly or level off. In order to evaluate the benefit of increased data collection on model skill, the models were evaluated by shuffling the data 100 times, and fitting the models on training libraries of various sizes, from 5 to 85% of the total length of the dataset. Each instance was tested on an out-of-sample set of shuffled data (15% of the total length of the dataset), as well as an in-sample set of data (30% of the training library used for that model instance). Data shuffling prevented biases caused by the uneven temporal distribution of states (e.g. some segments in the time series have more open oyster valve gape states than closed states). In-sample testing was used to evaluate model overfitting (skill metrics for in-sample testing should be comparable to the skill metrics for out-of-sample testing).

1.3 Results

1.3.1 Distributions of Oyster Valve Gape and Environmental Time Series

Figure 1.2 shows the time series and distributions of 30 minute processed (a-b) and tidally averaged (c-d) oyster valve gape, with the 30 minute processed time series showing a two day segment of the record to highlight its variability. On the shorter timescale (Figure 1.2a-b), variability between individual oysters is observed. However, within each set, oysters at the same depth in the water column behave similarly to one another and exhibit different patterns of opening and closing between the surface vs. the bottom group. The distributions show both depth groups experienced bimodal distributions with a peak at fully closed (0 gape fraction) and a broad peak centered around a gape fraction of 0.5 (Figure 1.2b). The distributions also show that the surface oysters were open less frequently than the bottom oysters. On the

tidally averaged timescale, each oyster behaved similarly to those within the same depth set (Figure 1.2c-d), and the surface vs. bottom oyster sets followed each other fairly closely until late February, when the two oyster sets began to show an inverse relationship in their gape behavior. When the tidally averaged time series shows a high gape fraction it reflects a time period when oyster closures only occur briefly each day/semi-diurnal period (see for example the shorter time series in panel a), however when the tidally averaged time series has a valve gape fraction near zero, that indicates that oysters were closed over the majority of the semi-diurnal period. All oysters were predominantly closed at the start and end of December 2019 and predominantly open through January and most of February 2020. The surface oysters were closed for most of the time in March and April (Figure 1.2c), which is reflected in the tidally averaged distributions (Figure 1.2d).

The full time series of oyster gape and all environmental variables are further examined by plotting their fields by time of day versus day (see Figure 1.3 and Figure 1.4). In this view, diurnal processes will show up as vertical stripes, tidal processes will show up as diagonal stripes, and event-scale variability will show up as horizontal stripes. This is most easily seen on the diurnally forced solar irradiance, which results in strong vertical stripes on Figure 1.3b. Wind forcing is strongly diurnal. These figures also highlight well known high vertical stratification (Figure 1.4 'Surface-Bottom Difference' in salinity) (Harvey et al. 2023b), and a diurnal phase shift in surface vs. bottom heating (Figure 1.4 'Surface-Bottom Difference' in temperature). Water level is tidally forced and thus shows diagonal stripes on Figure 1.3a. Waves and river discharge are dominated by event-scale variability. It is also clear that events influence other water quality parameters as expected such as salinity and DO, which clearly vary with river discharge events. The other variables show a mixture of diurnal, tidal and event variability (pH, turbidity, DO, salinity, temperature).

The time series in Figure 1.4 shows that oyster gape has diurnal, tidal, and event-scale variability. Overall, the bottom oysters are more open than the surface oysters (blue), particularly during these river discharge events (Figure 1.4). While a clear diurnal cycle is a bit hard to

discern from each oyster set given overlap of semi-diurnal and event variability, the difference in the top and bottom oyster gape shows a clear diurnal pattern (i.e. surface oyster gape fraction being higher than bottom oysters during daytime hours and lower at night) suggesting a diurnal phase shift between each set. The surface oysters close during events when salinity and DO are low (horizontal dark lines across gape, salinity, and DO panels), coinciding with transient events of high river flow, low pH and high turbidity seen in Figure 1.3 (horizontal lines at the same time periods).

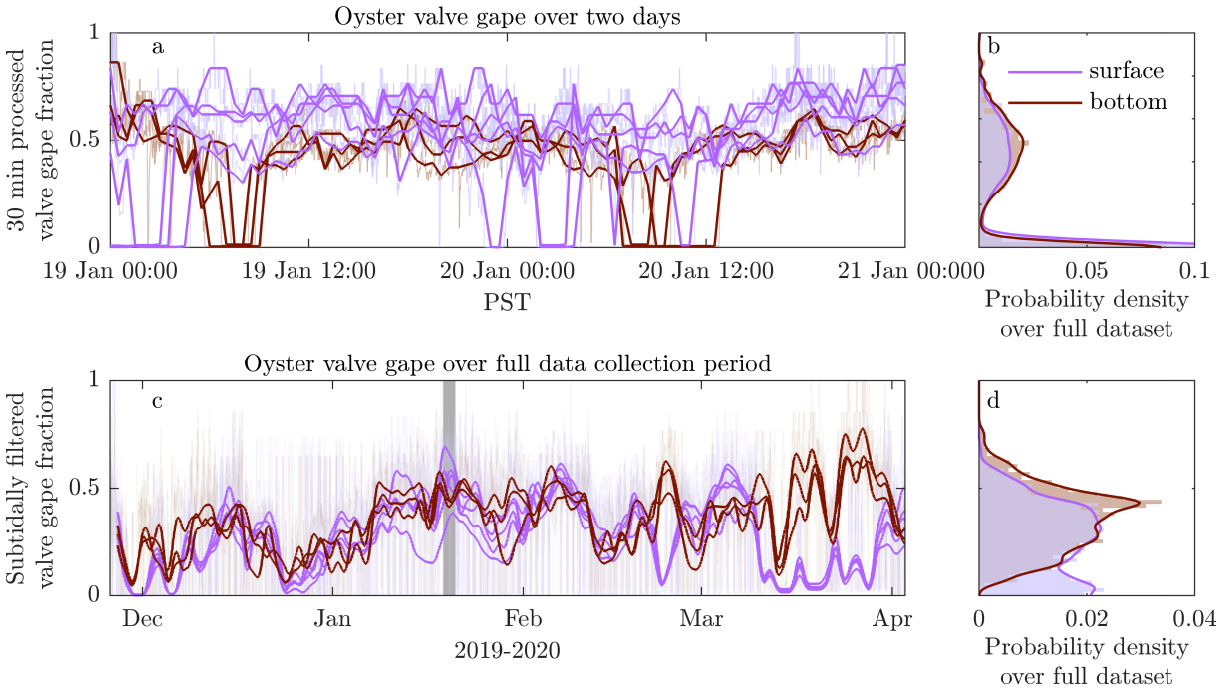


Figure 1.2. Time series and distributions of *Crassostrea gigas* valve gape. The vertical axes on all panels shows the fractional valve gape, where zero indicates that an oyster is fully closed, and one indicates that an individual oyster is at its maximum gape that was observed over the entire data collection period. **a** 2-day snippet of 30 minute processed valve gape. The raw time series is shown faintly in the background. **b** The distribution of the full 30 minute processed time series. **c** Tidally averaged valve gape over the full 4.5 month record, with its corresponding distribution at the right. The vertical gray bar highlights the time period shown in panel **a**. 30 minute processed time series are shown faintly in the background of **c**. **d** The distribution of the full tidally averaged time series.

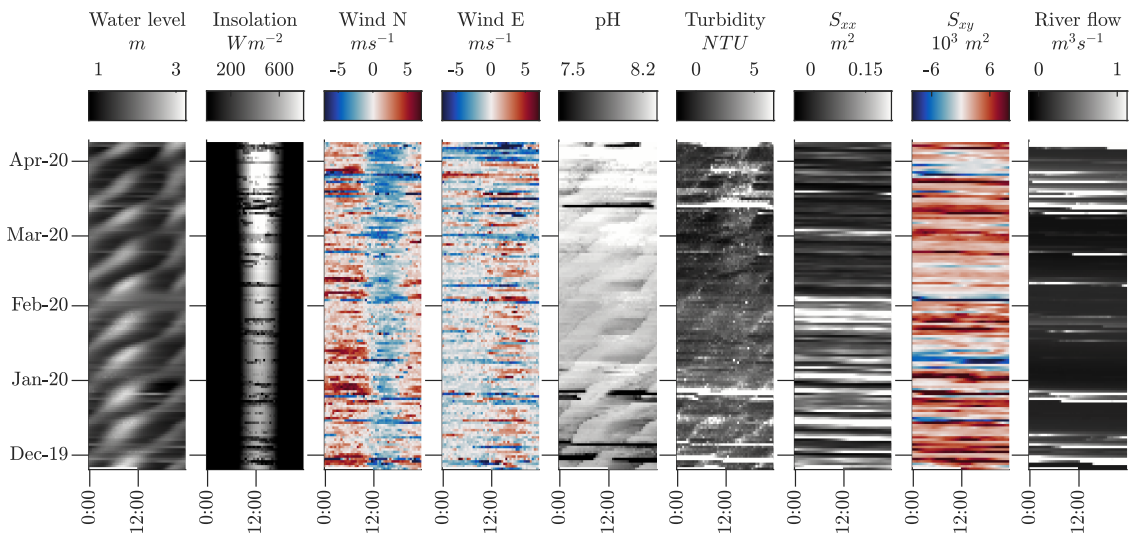


Figure 1.3. Time series of 30 minute processed environmental variables measured in or near to Los Peñasquitos Lagoon from late November 2019 through April 2020. The variables shown from left to right are water level (m), Solar irradiance (Wm^{-2}), northerly and easterly wind speeds (ms^{-1}), pH, turbidity (NTU), cross-shore and along-shore radiation stresses S_{xx} and S_{xy} (m^2), and river flow (m^3s^{-1}). Time of day is shown on the horizontal axes, and calendar day is shown on the vertical axis. Displaying the data by both time of day and time highlights diurnal features as vertical stripes across the figures and tidal (semi-diurnal) features as diagonal lines. Event-scale features appear as horizontal stripes. Note that the color bars for turbidity and river flow are capped below their maximum values to highlight their variability.

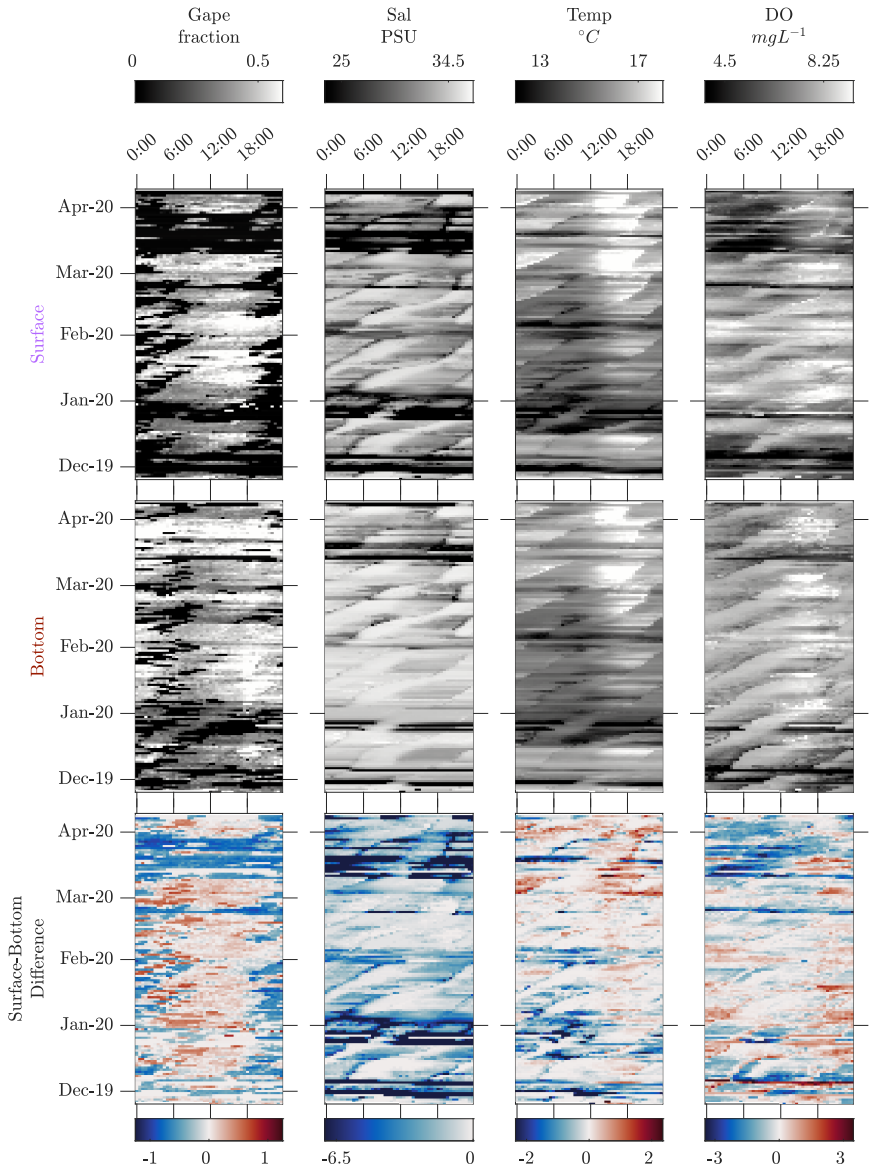


Figure 1.4. Time series of 30 minute processed data from the LPL mooring from late November 2019 through April 2020. The variables shown, each in its own column, are oyster valve gape fraction (labeled as Gape fraction), salinity (Sal, PSU), temperature (Temp, $^{\circ}C$), and dissolved oxygen (DO, mgL^{-1}). The top row labeled at the left in purple as 'Surface' shows the data from the surface sensors. The middle row, labeled at the left in brown as 'Bottom', shows the data from the bottom sensors. The bottom row, labeled at the left as 'Surface-Bottom Difference' shows the difference between the surface and the bottom sensors where positive (red) values indicate that the top sensors have higher values than the bottom and negative (blue) values indicate that the bottom sensors have higher values than the top. Time of day is shown on the horizontal axis, and day is shown on the vertical axis as done in Figure 1.3. Compare to Figure 1 in Tran et al. (2011)

1.3.2 Spearman Correlations

The strongest relationships of near-surface oyster valve gape are on the tidally averaged timescale, with salinity and dissolved oxygen at the surface (Figure 1.5). Salinity leads or lags behind surface oyster valve gape by no more than 2.5 hours. Dissolved oxygen leads surface oyster valve gape by no more than 14.5 hours. On the tidally averaged timescale, surface oyster valve gape is consistently positively correlated with insolation, pH, salinity, and dissolved oxygen, and is negatively correlated with water depth, turbidity, alongshore radiation stress S_{xy}, and river flow. On the tidally averaged timescale, near-bottom oyster valve gape has the clearest relationships with northerly wind speed (with lags ranging from 26.5 to 40.5 hours), positively correlated with easterly wind speed (with lags ranging from -2.5 to 13 hours), and negatively correlated with alongshore radiation stress (with lags ranging from -1.5 to 5 hours).

On the high-frequency (shorter than tidally averaged, and longer than 30 minute processed) timescale, the surface oysters have the strongest and most consistent relationships with insolation (positive), temperature (positive), water depth (negative), and northerly wind speed (negative). Near-bottom oyster valve gape has the clearest relationships with insolation and temperature on the high-frequency timescale. Surface oyster valve gape leads temperature by about 5 hours, while bottom oyster valve gape leads temperature by an hour or less. Surface oyster valve gape is approximately in phase with insolation (lagging behind by an hour or less), while near-bottom oyster valve gape is negatively correlated with insolation, leading it by six hours.

The cross correlations of the 30 minute processed data reveal a more complex picture, with all variables but northerly wind and crossshore radiation stress S_{xx} having some statistically significant correlations with surface oyster valve gape. Salinity, DO, river flow, pH, and turbidity have the overall strongest correlations with surface oyster valve gape. Bottom oysters overall have a weaker response to all variables, with some significant correlations with both wind components, alongshore radiation stress S_{xy}, and temperature.

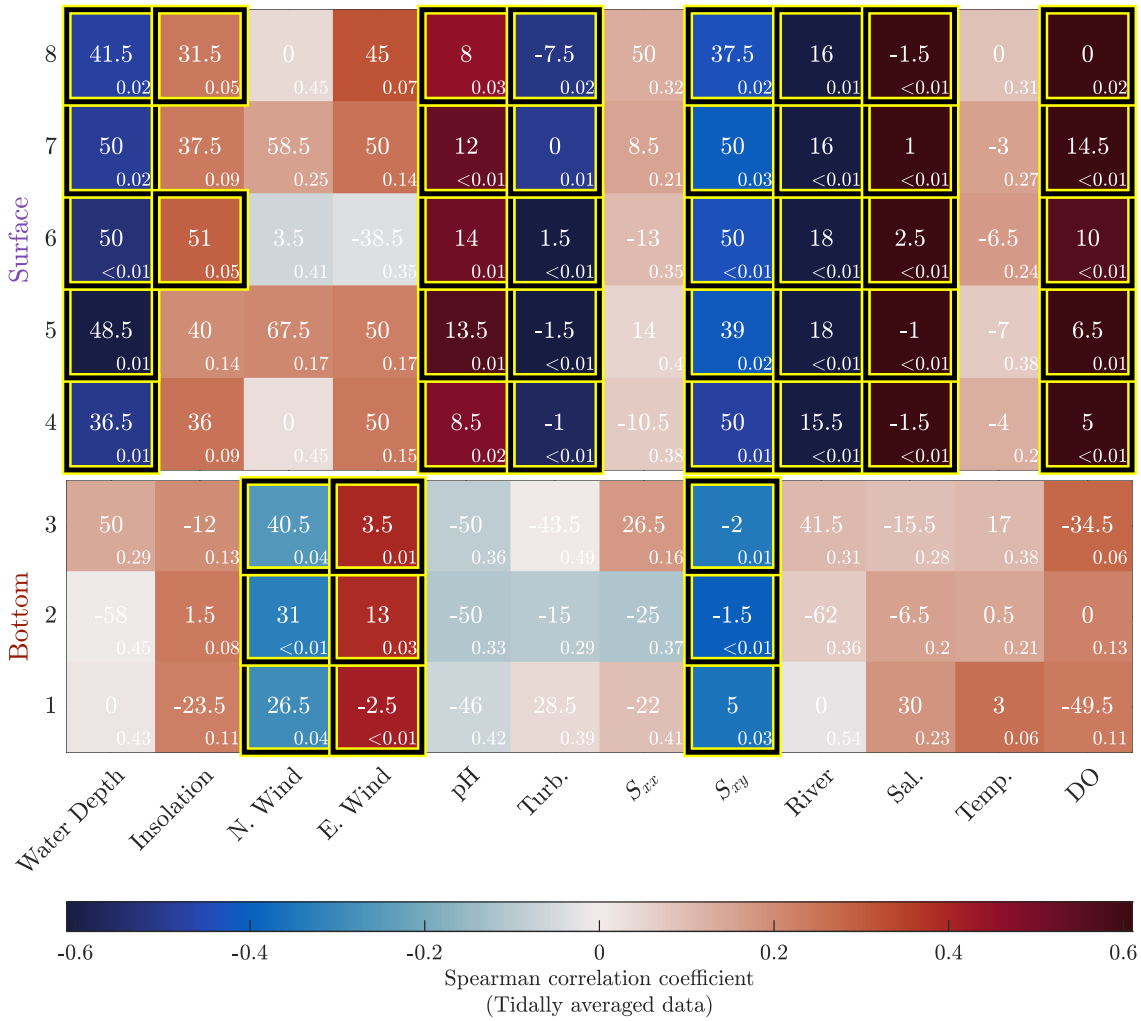


Figure 1.5. Cross correlations between each oyster valve gape time series and each environmental variable at the tidally averaged time scale in LPL. The vertical axis shows each oyster (indexed 1-3 on the bottom of the mooring, 4-8 near the surface). Blue indicates a negative correlation, and red indicates a positive correlation. The large numbers in each cell are the lag in hours of the central peak. Positive lag values indicate valve gape lagging behind the environmental variable. The small numbers in the bottom right corner of each cell are the bootstrapped p-values. Cross correlations with p-values less than or equal to 0.05 are identified with bold black and yellow borders.

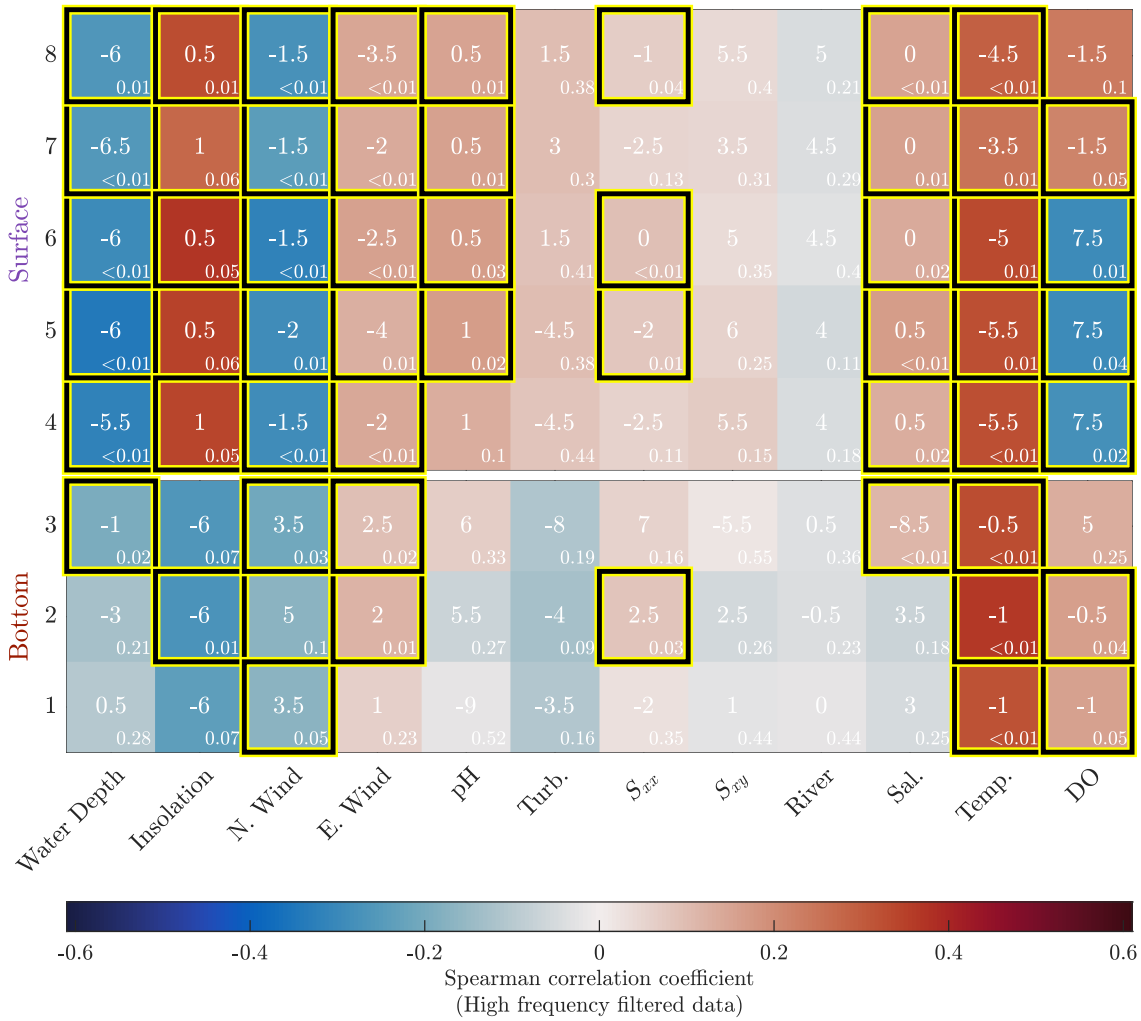


Figure 1.6. Cross correlations of the high-frequency (shorter than tidally averaged, longer than 30 minute processed) residuals of the tidally averaged time series of oyster valve gape and each environmental variable in LPL. The vertical axis shows each oyster (indexed 1-3 on the bottom of the mooring, 4-8 near the surface). Blue indicates a negative correlation, and red indicates a positive correlation. The large numbers in each cell are the lag in hours of the central peak. Positive lag values indicate valve gape lagging behind the environmental variable. The small numbers in the bottom right corner of each cell are the bootstrapped p-values. Cross correlations with p-values less than or equal to 0.05 are identified with bold black and yellow borders.

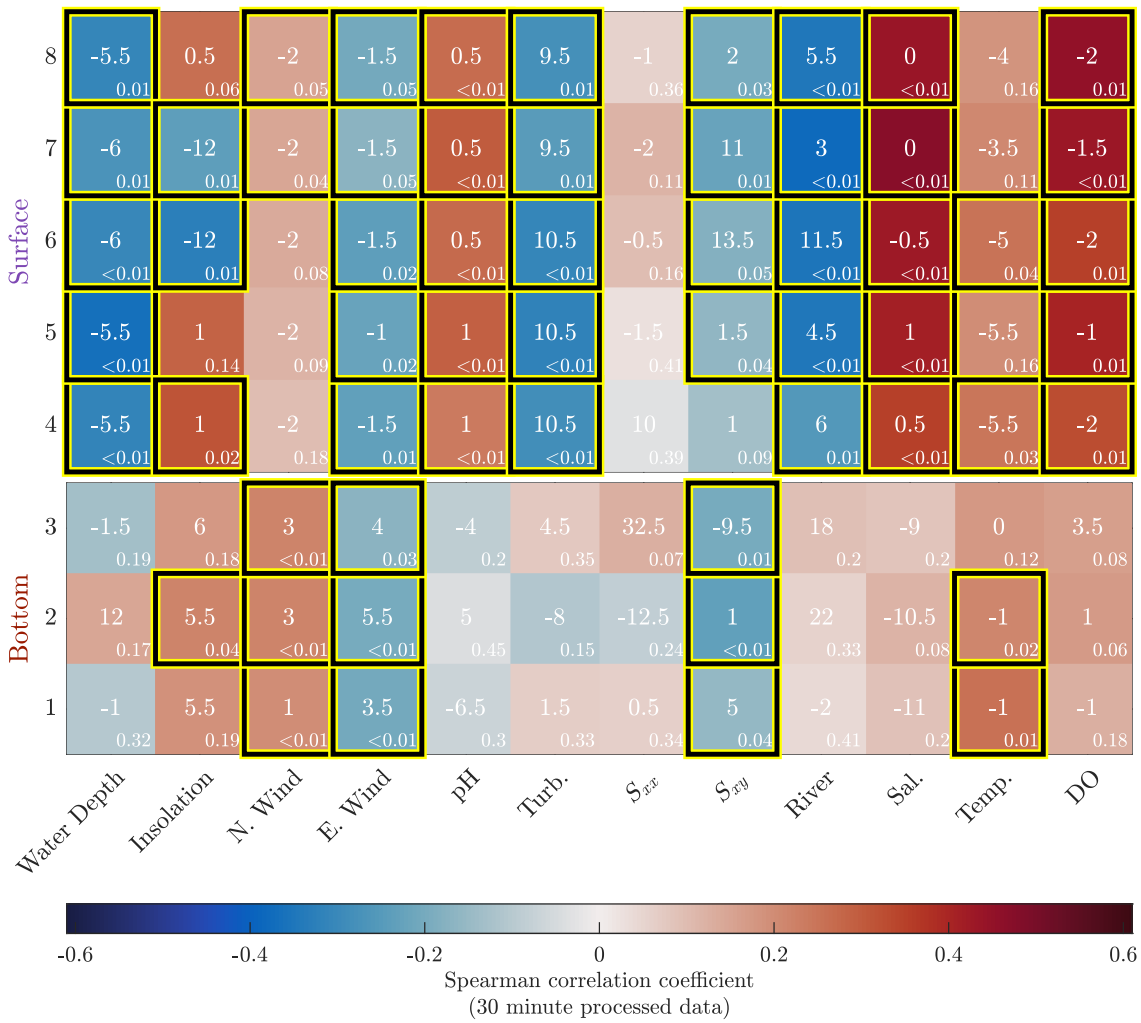


Figure 1.7. Cross correlations of the 30 minute processed time series of oyster valve gape and each environmental variable in LPL. The vertical axis shows each oyster (indexed 1-3 on the bottom of the mooring, 4-8 near the surface). Blue indicates a negative correlation, and red indicates a positive correlation. The large numbers in each cell are the lag in hours of the central peak. Positive lag values indicate valve gape lagging behind the environmental variable. The small numbers in the bottom right corner of each cell are the bootstrapped p-values. Cross correlations with p-values less than or equal to 0.05 are identified with bold black and yellow borders.

1.3.3 Solar Phase Distributions

The surface and bottom oysters have distinct diurnal behavior (Figure 1.8). While the surface oysters are most open around noon, the bottom oysters are most open later in the day,

near dusk. This is also seen on Figure 1.4 bottom left panel. This phase offset can also be seen in Figure 1.6 with the lagged correlations between each oyster and temperature. These correlations indicate that peaks in oyster valve gape preempt maximum temperature by about an hour for the bottom oysters and by about four hours for the top oysters. The peak daily temperature of coastal water occurs in the late afternoon/early evening, a few hours after the peak insolation at solar noon (Rasmussen et al. 2020), a time difference that mirrors the lags seen here. This distinct behavior between surface and bottom oysters is consistent at the quartiles of the distributions.

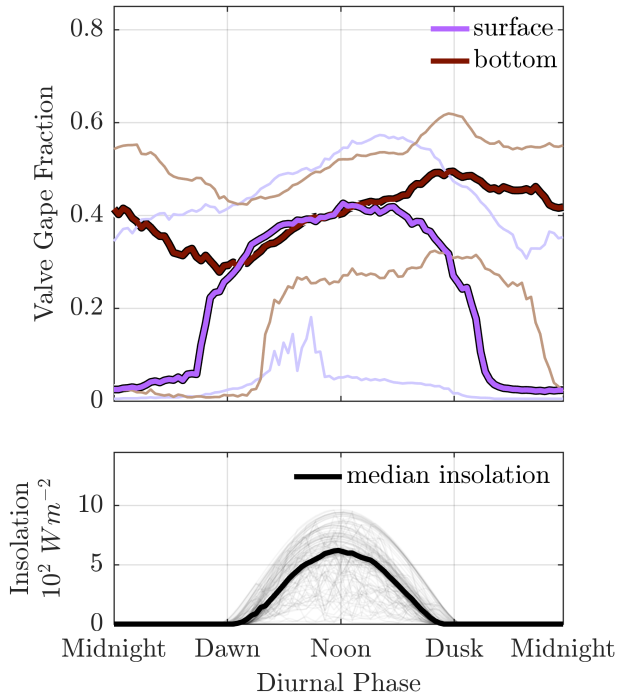


Figure 1.8. Top panel: solar phase distributions of oyster valve gape fraction in LPL. The median surface and bottom oyster data are shown in purple and brown, respectively. Quartiles are shown in thin lines in their corresponding colors. Bottom panel: median diurnal insolation cycle, with lighter gray lines showing each instance of this cycle (N=133), including cloud cover..

1.3.4 Tidal Phase Distributions

The tidal phase distributions of oyster valve gape also shows distinct behavior between the surface and bottom oysters. Both sets of oysters have a lower median valve gape around the higher-low tide ($\frac{3\pi}{2}$ in Figure 1.9), although the surface oysters' response is far more dramatic. Both sets of oysters have a predominantly diurnal tidal pattern. Harvey et al. (2023b) show the

highest stratification of the tidal cycle around this higher-low tide in LPL, which is likely due to tidal straining during the ebb tides, and is commonly observed in estuaries (Stacey et al. 2001; Geyer and MacCready 2014). Stratification results in less vertical mixing, possibly reducing food availability to oysters at both depths, through reduced mixing of phytoplankton to the lower water column and reduced mixing of nutrients into the upper water column. The surface oysters have a larger response to this since the stratification often leaves them in fresher water from upstream.

Median oyster valve gape fraction is greater during spring higher-high tides than during neap higher-high tides. Surface oysters close following spring lower-low tides and following neap lower-high tides (not shown). This may be a result of the estuary briefly losing high salinity inflow from the ocean due to a combination of the inlet sill and low water level at spring lower low tide, thus reducing the water and possibly nutrient flow around the oysters. Water level within LPL continues to ebb and freshen until around midway through the rising tide, indicating that the oysters are responding immediately to the changing tide (Harvey et al. 2023b).

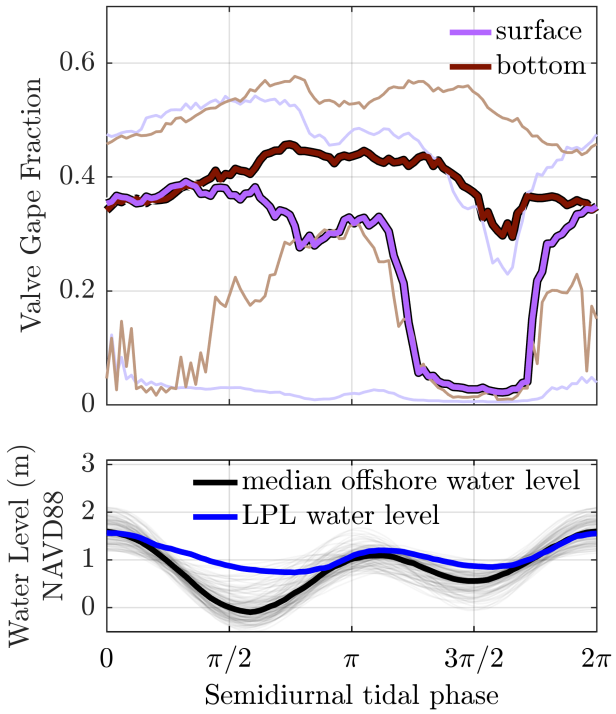


Figure 1.9. Top panel: tidal phase averaged oyster valve gape in LPL. The median surface and bottom oyster data are shown in purple and brown, respectively. Quartiles are shown in thin lines in their corresponding colors. Bottom panel: The black line shows the median tidal cycle of the offshore water level, with lighter gray lines showing each instance of this cycle (N=122). The blue line shows the median tidal cycle of the water level measured at the mooring within LPL.

1.3.5 Joint Distributions

While correlation coefficients show which variables have relationships, the complex nature of those relationships is not easily quantified. Salinity, dissolved oxygen, and pH are positively correlated with surface oyster valve gape, while turbidity is negatively correlated with surface oyster valve gape. These relationships are all consistent with the oysters responding to tidal and episodic forcing, as these variables are all correlated with the tidal cycle in LPL (Harvey et al. 2023b) and consistent with episodic storm forcing. To clarify the relative influence of these correlated variables on median valve gape fraction, we look at the joint distributions of median valve gape fraction with respect to dissolved oxygen and salinity, and pH and turbidity (Figure 1.10).

For oysters near the surface, when salinity is less than approximately 30 *PSU*, oyster

valve gape has a dissolved oxygen threshold around 7 $mg\ L^{-1}$, above which oysters are most open. When salinity is higher, the oxygen threshold is lower, around 4.5 $mg\ L^{-1}$. This suggests that oysters respond to both oxygen and salinity, and that high values of either one is associated with open valve gape, even if the other is lower.

Oysters near the bottom of the water column similarly are more open when there is high salinity and high dissolved oxygen. The bottom oysters are more open when dissolved oxygen is greater than approximately 5 $mg\ L^{-1}$, and do not have a clear salinity threshold value. Although the bottom oysters spend more time within a narrower range of salinity (higher values) and dissolved oxygen than the surface oysters, the bottom oysters appear to be more willing to remain open in a broader range of salinity and dissolved oxygen concentration.

Surface oysters are most open when turbidity is below approximately 8 NTU, as long as pH is above approximately 7.8. Bottom oysters are more tolerant of higher turbidity than are the surface oysters when pH is high, with a threshold that increases linearly. Bottom oysters have a threshold pH of approximately 7.6, below which they are closed at all values of turbidity. It is important to note that here pH and turbidity are both measured near the bottom of the water column, so some differences in the upper water column may not be captured by this analysis with the surface oysters.

A joint distribution of median valve gape fraction with respect to pH and salinity (not shown) reveals that surface oyster valve gape is more dependent on salinity, while bottom oyster valve gape is more dependent on pH. The salinity cutoff for median surface oyster valve gape is approximately 27 PSU when pH is 8.6, increasing to approximately 33 PSU when pH is lower, at 7.4. The pH cutoff for median bottom oyster valve gape is approximately 7.9 when salinity is 18 PSU, decreasing to a pH of around 7.5 when salinity is 34 PSU.

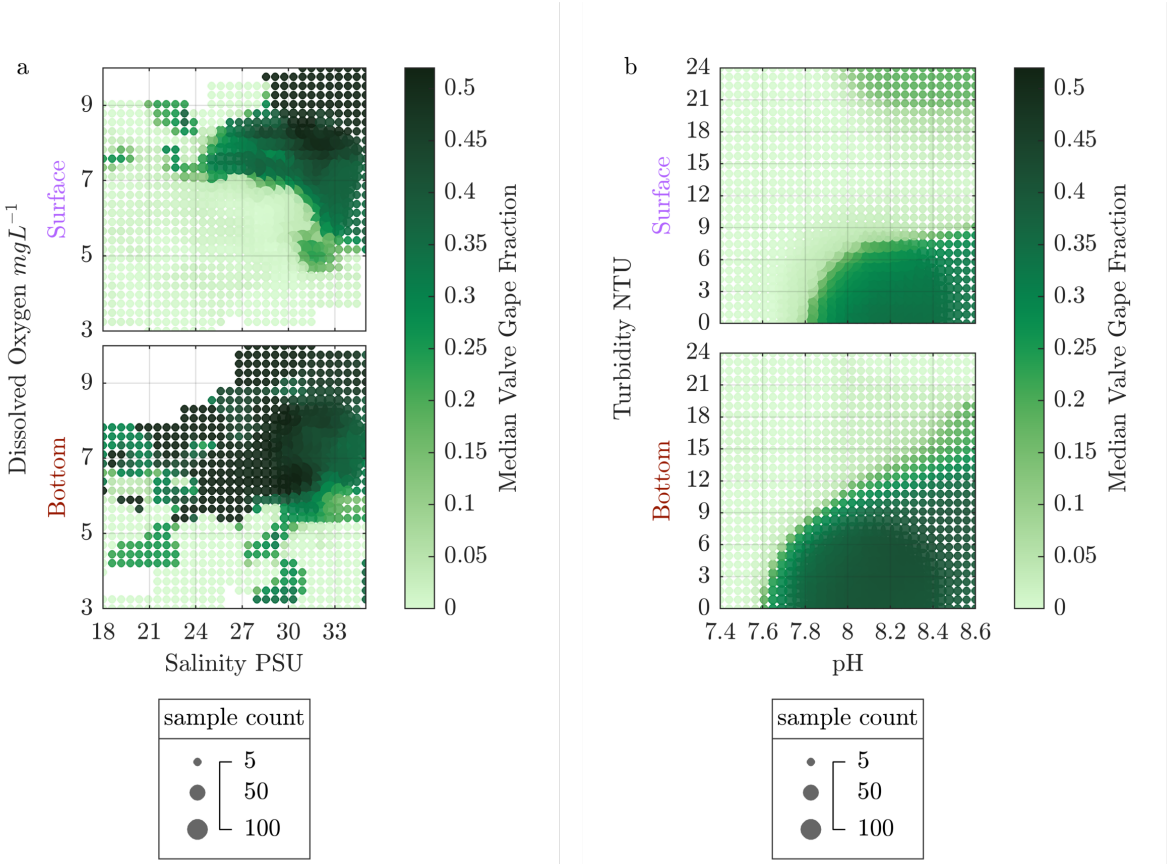


Figure 1.10. **a** Joint distributions of median oyster valve gape as a function of salinity and oxygen in LPL. The top plot shows values for the oysters near the surface with near-surface measurements of salinity and oxygen, and the bottom plot shows the corresponding bottom measurements. **b** Joint distributions of median oyster valve gape as a function of pH and turbidity. The top plot shows values for the oysters near the surface with near bottom measurements of pH and turbidity (as these variables were only measured near-bottom), and the bottom plot shows the corresponding bottom oyster measurements. Larger dots indicate more measurements in that bin, varying continuously in size. Darker dots indicate a greater median valve gape fraction (i.e., oysters are more open).

1.3.6 Multivariate Models

Given the stronger relationships of near-surface oyster valve gape compared to that of near-bottom oyster valve gape, the multivariate models were only tested using data from the near-surface oysters. All models tested explained a large fraction of the variance (R^2), indicating that the chosen variables together explain surface oyster valve gape behavior (although not necessarily causally) (Figure 1.11). Using 80% of the full time series, or 108 days of data for

the training library, the largest R^2 value across all models is 0.84, for S-Map. The smallest R^2 value is 0.41, for knn. Similar values for in and out of sample skill scores indicate that these models are not overfitting, and should generalize well to new data. S-Map provided the model with the highest skill, improving rapidly over the other models as the training set size increased, indicating the nonlinearity of the dataset, and that the state space is not yet fully resolved, and model performance will improve with new data in varying estuary conditions.

The time series of surface oyster valve gape fraction from March 1 to April 8 2020 is shown in Figure 1.12 along with the predictions of one instance of each model, trained on data from December 26 2019 to February 28 2020 (a 70% / 30% training / prediction split). In this model instance, S-Map has the best skill scores ($R^2 = 0.48$, $RMSE = 0.14$, Willmott Score $= 0.84$, Bias $= 0.04$, Pearson's $\rho = 0.73$, Spearman's $\rho = 0.74$), followed by Simplex ($R^2 = 0.27$, $RMSE = 0.88$, Willmott Score $= 0.71$, Bias $= -0.33$, Pearson's $\rho = 0.61$, Spearman's $\rho = 0.67$).

The local regression coefficients produced through this S-Map model instance (Figure 1.12) reveal that out of all the predictor variables, dissolved oxygen has the largest contribution when the mean surface oyster valve gape is in a closed state (i.e., March 13-17, 18-21, and April 7-9). Throughout most of the rest of the time series salinity dominates in importance. Overall, simultaneous variables had larger coefficients than the lagged variables, except for lagged pH which briefly has larger coefficients than all variables except for salinity before and after the oyster closures. It is valuable to note that this time period shown includes widely ranging conditions with frequent freshwater input due to storms (see Figure 1.3 and Figure 1.4).

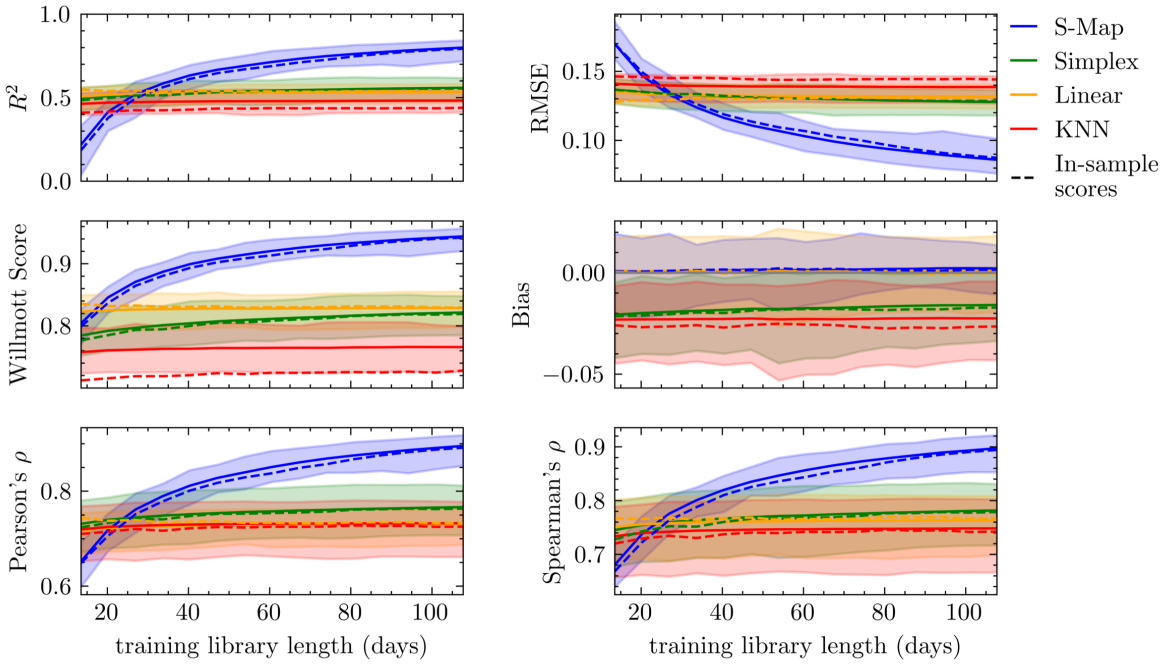


Figure 1.11. Model learning curves, showing six different skill metrics for each of the four models as a function of the training dataset length. The x axis covers 5-85% of the full data set. Solid lines are the skill values when the model is tested on an out-of-sample set of data, while dashed lines indicate skill values when the model is tested on an in-sample set of data.

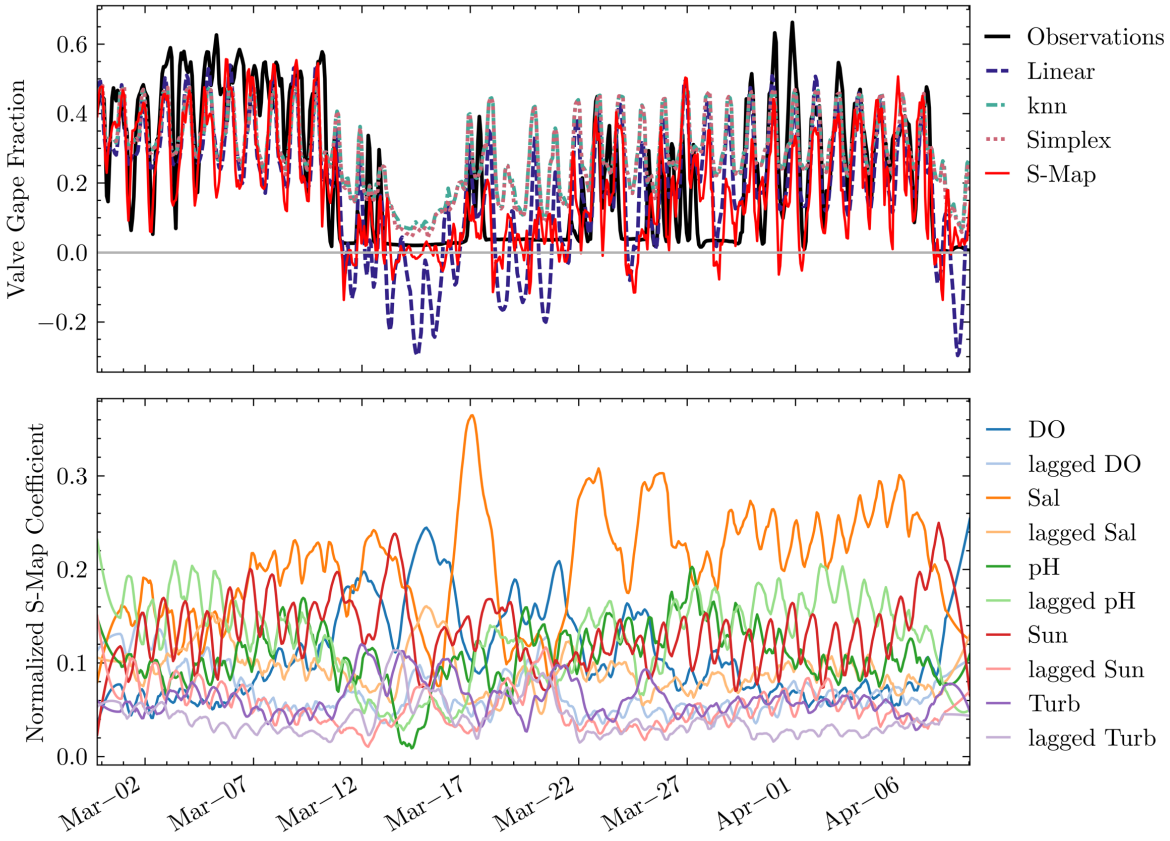


Figure 1.12. Top panel: model predictions for February 29 2020 through April 9 2020 of 6-hour half-Hamming filtered mean surface oyster valve gape fraction, trained on 70% of time series (December 26 2019 - February 28 2020). Bottom panel: Normalized S-Map time varying coefficients for each variable used as predictors in the model, showing the relative contribution of changes in each variable to a change in oyster valve gape. For ease of visual interpretation, coefficients have been smoothed with a 3-day Hamming filter.

1.4 Discussion

This study focused on determining the relationship on tidally averaged and high-frequency time scales of oyster valve gape behavior in LPL with salinity, temperature, depth, and dissolved oxygen, as well as with nearby water quality and environmental conditions such as estuary pH and turbidity, solar irradiance, coastal water level, upstream flow rate, offshore wave radiation stress, and wind speed. The strongest relationships found were with tidally averaged salinity and dissolved oxygen (positive Spearman's correlation coefficients of approximately 0.6), specifically

among the instrumented oysters near the surface of the water column. The oysters near the surface also responded to pH (positive correlation), turbidity (negative correlation), and upstream flow rate (negative correlation). These relationships are consistent with co-variance between the water quality variables expected during storms; freshwater input from storms (higher upstream flow rate) brings low salinity, lower pH, higher turbidity, and lower DO water into the estuary. Note that during these events is also when the water column is most stratified (see Figure 1.4 bottom panel).

Bottom oysters appear far less sensitive to the measured environmental variables on either the tidally averaged or higher frequency time scales. They do have statistically significant, although inconsistent, relationships with wind speeds and along shore radiation stress S_{xy}, particularly on the tidally averaged timescale, possibly due to the influence of these variables on bottom mixing and sediment transport and suspension. This is not reflected in the near-bottom oyster valve gape correlation with turbidity, which had no statistical significance. Despite this, near-surface oyster valve gape was found to have a significant correlation with turbidity. Estuaries tend to be more turbid at depth due to the effects of stratification and fluvial and tidal sediment transport (Uncles et al. 2002). The lack of a significant correlation between near-bottom oyster valve gape and turbidity can possibly be explained by acclimation of the near-bottom oysters to more turbid conditions, which has shown to be related to changes in the gills and pallial organs of *C. gigas* (Barillé et al. 2000; Dutertre et al. 2009). There also may be some relationships with other variables compounding this such as the fact that turbidity is highly correlated with river discharge which is shown to impact surface oysters more strongly than bottom oysters due to stratification. Correlations with wind speeds and alongshore radiation stress for both the near-surface and near-bottom oysters are more likely indirect, all being influenced by episodic storm conditions.

The relationships shown through cross-correlations of oyster valve gape with temperature and insolation may be due to surface oysters responding to light exposure and solar radiation, rather than changes in temperature in the surrounding water. A cross correlation between surface

and bottom temperature with insolation (not shown in this paper), gives a positive maximum correlation with solar irradiance at a lag of 4.5 hours. The surface oysters thus may be responding to light, or an associated variable such as phytoplankton abundance, while the bottom oysters are responding to temperature. However, solar irradiance was not measured at the bottom of the water column in this experiment, so directly determining the difference in light exposure between the surface and bottom oysters was not possible. These relationships are supported by the solar phase distribution, that show similar lags between the diurnal cycle of oyster valve gape and solar phase.

Phase distributions showed diurnal and tidal cycles in oyster valve gape behavior, consistent with research at other sites which have shown oyster valve gape to respond to both light and temperature (Tran et al. 2011; Casas et al. 2018). The diurnal cycle of near-surface and near-bottom oyster valve gapes are offset by approximately a quarter of a day, with surface oysters most open at midday, and bottom oysters most open in the evening. This may be attributed directly to temperature, or to other diel cycling of variables which were not measured during this field campaign, such as the vertical migration of plankton (on which oysters feed), which has been observed in other shallow estuaries, e.g. Hall et al. (2015). Valve gape behavior aligning with the tidal cycle appears consistent with oysters responding to tidal cycle variability in water quality parameters as observed in LPL, which is consistent with other tidally influenced, stratified estuaries (Harvey et al. 2023b). Similarly, the stronger response of near-surface oysters relative to near-bottom oysters to their environmental conditions is consistent with stratification leading to overall more variable water quality conditions near the surface. The phase relationship of oyster valve gape with the tidal cycle suggests that it is unlikely that oyster valve gape behavior has a direct dependence on water velocity. The observations in Harvey et al. (2023b) show that velocity in LPL acts like a standing wave, 90° out of phase with water level. This, together with the predominantly diurnal tidal pattern of valve gape, indicates that oysters are responding to varying water properties, rather than to velocity.

This investigation of these observations shows a strong and consistent near-surface oyster

response to multiple environmental parameters. The strongest response is with salinity and DO (with oysters preferring higher salinity and higher DO conditions with some thresholding effects). However, some of the conclusions drawn from this set of analyses are challenged by co-variance of the water quality parameters (for example, the lower salinity water has lower pH) and nonlinear relationships between oyster valve gape and the environmental variables.

The S-Map model was the strongest multivariate model tested, and should be explored further as a predictive monitoring tool. The local linear regression coefficients for each predictor variable provided through the S-Map model confirm the relative importance of simultaneous DO and salinity on oyster behavior. However, future models should take into account the non-negativity of oyster valve gape to produce more accurate predictions. It is worth noting that higher skill may be possible with an optimized lag for each variable, rather than a single lag applied to all variables. Including the lagged variables, compared with only including simultaneous variables), moderately improved skill scores for all models. The S-Map model improving the most, with an increase in the R^2 value by about 0.05. The overall greater performance of S-Map (and to a lesser extent Simplex) compared with the other models is a good indicator of the state dependence of system dynamics in LPL. Linear analyses assume separability of the effects of each variable, while models like S-Map and Simplex do not rely on this assumption. Accordingly, future analyses should explore a variety of nonlinear models.

Our study had some limitations that are important to consider when trying to contextualize this work for operational BEWS. To that end, we recommend the following improvements to our methodology. Given the significant inter-oyster variability in this study (including the death of one oyster at the beginning of the deployment), oyster sample size should be increased as much as possible. We also suggest co-location of chlorophyll sensors (to assess phytoplankton, i.e., food source, abundance), and pH and turbidity sensors (here we were limited to pH and turbidity only near the bed).

To observe the oyster sensitivity to cross-channel and along-channel location, moorings could be deployed at multiple sites within a single estuary. Comparisons could also be made to

native bivalve species to examine the extent to which their responses to environmental conditions differ in a changing estuary and climate (Skelton et al. 2024). Valve gape behavior of native species may also provide more effective indicators of pollution (Kelleghan et al. 2023). Finally, comparison across different sites would help elucidate if bivalve response varies by site or if there are some environmental cues that species respond to similarly across sites.

The deployment length should be increased as long as possible, or deployments should be overlapping, to observe and account for seasonal cycles in environmental parameters and oyster valve gape, such as that observed in Tran et al. (2011). Longer deployments will also allow observations before and during estuary inlet closures. Following the mooring deployment analyzed in this study, the mooring was redeployed with 8 new oysters during an inlet closure. The oyster mooring was not deployed while the inlet was closing. During the closure, compared to conditions when the inlet was open, near-surface and near-bottom salinity were low, near-surface and near-bottom temperature were high, and near-bottom dissolved oxygen and pH were low. All but two oysters (near-surface) on the mooring died within 5 days, before the inlet reopened. The redeployment occurred during a red tide (Skelton et al. 2024), creating particularly challenging conditions for the oysters. Continuous oyster valve gape observations spanning before, during, and after an inlet closure (or other high stress or mortality event) would be useful to determine oyster resilience to rapidly changing conditions, and provide timescales for biological response to inlet closures, stressors, and even for mortality. This information would be crucial to estuary management's decisions regarding response time to inlet closures before damage to the bivalve community.

All of these experimental modifications would help contextualize the usefulness of BEWS and the importance of local calibration of such systems. Beyond the use of BEWS to the environmental issue of inlet closures, there is the potential for their application in a variety of other management contexts (Andrewartha et al. 2015; Arroyo et al. 2022; Vereycken and Aldridge 2023; Meira et al. 2024). This includes exploring the use of biosentinels in issues of local management importance, such as aquaculture (Wallace 2023), invasive species assessment

(Crooks et al. 2015), pollution monitoring (Mladenov et al. 2024), living shoreline creation (Ridlon et al. 2021), and developing indicators for tracking restoration success (Walker et al. 2025).

1.5 Conclusions

This study adds to the existing body of literature on how bivalves and benthic organisms respond to environmental changes in Los Peñasquitos Lagoon (Novoa et al. 2016; Levin et al. 2023) as well as to the body of literature on BEWS (e.g., Bae and Park 2014). The temporal and spatial scales measured and analyzed here provides new insight into bivalve behavior in this estuary, as well as more broadly as they can be used in BEWS. Our results show oysters responding to both salinity and DO with a strong impact of vertical stratification leading to differing responses of near-surface and near-bottom oysters. There is also a response to pH, turbidity, and a clear influence of both diurnal and tidal cycles (which due to the estuarine dynamics drive tidal variability in all water quality parameters). However, due to nonlinear responses and co-variance of environmental parameters, we tested several multivariate models. Multivariate nonlinear models such as S-Map show some promise in predictability and even data attribution, thus additional data collection to further test these models would be valuable. Combining further studies of this type with multivariate nonlinear models could allow managers to optimize which parameters are most critical to observe for establishing useful BEWS and provide insight into the use of similar BEWS across different systems.

1.5.1 Funding

This work has been supported by the National Estuarine Research Reserve (NERR) System Science Collaborative, which supports collaborative research that addresses coastal management problems important to the reserves. The Science Collaborative is funded by the National Oceanic and Atmospheric Administration and managed by the University of Michigan Water Center (NA19NOS4190058, subaward SUBK00016699). Biosensor and hydrodynamic sensor

deployment was also supported in part by NOAA's National Centers for Coastal Ocean Science (NCCOS) Competitive Research Program under award NA18NOS4780172 to the Scripps Institution of Oceanography, University of California, San Diego, and by award NA16NOS4780205 to the CA Coastal Conservancy. NERR real-time data collection is supported by the NOAA Office for Coastal Management, award #NA24NOSX420C0043. This work is partially supported by grants from California (CA) Department of Parks and Recreation's Natural Resources Division and Division of Boating and Waterways, USC Sea Grant, CA Sea Grant, and NSF. This is CHRP contribution #270. This is contribution number XX of the Coastal and Marine Institute Laboratory, San Diego State University. The statements, findings, conclusions, and recommendations are those of the participants/authors and do not reflect the views of NSF, NOAA, the Department of Commerce, or the Department of the Interior.

1.6 Authors' Contributions

NA performed the analysis, and wrote the original manuscript. SNG led project administration and supervision. SNG, LPM, and GS developed and supervised methodologies and analysis approaches. SNG, LPM, LAL, KAG, and JC conceived of the idea and obtained funding for the project. SNG, LPM, CN, LRM, and DW participated in field work. All co-authors participated in reviewing and editing the manuscript.

1.7 Acknowledgements

This work would not be possible without support and supplemental data from the Los Peñasquitos Lagoon Foundation, CA State Parks, the Tijuana River NERR, CDIP, SCCOOS, USGS, NOAA, the NERR SWMP, and the SIO Coastal Processes Group. In particular, we thank G Kalbach, M Hastings, J McCullough, M Cordrey, C Stafford, L Rose, D Smith, B Collins, R Flick, B Woodward, S Finnerty, and C Black. Chapter 1, in full, is a reprint of the material as it appears in Estuaries and Coasts, 2026. Anidjar, Niv; Giddings, Sarah N.; Neira, Carlos; Sugihara,

George; Levin, Lisa A.; Goodrich, Kristen A.; Crooks, Jeff; Wheeler, Duncan; McCormick, Lillian R.; Miller, Luke P., https://doi.org/10.1007/s12237-026-01759-6. The dissertation author was the primary investigator and author of this paper.

Chapter 2

Seasonally Inverse Tidally-Averaged Circulation in a Low-Inflow Estuary

Abstract: Low-inflow estuaries (LIEs) have density gradients shaped by both temperature and salinity, producing distinct circulation patterns from classical estuaries. San Diego Bay (SDB), an urbanized, seasonally inverse LIE in Southern California, has well documented longitudinal gradients and tidal exchange processes, but its tidally averaged, longitudinal circulation has not yet been fully described. Here, three years (2017 through 2019) of output from a three dimensional high resolution numerical model of SDB are analyzed using the Total Exchange Flow (TEF) framework in salinity, temperature, and density coordinates. Results showed a seasonally shifting two cell circulation structure. During summer, there is a thermally driven classical cell near the mouth, and a salinity driven inverse cell near the head. Elevated salinity combined with fall and winter cooling drive inverse circulation throughout the estuary. Entire bay classical circulation occurs during winter precipitation events; stronger precipitation produced persistent classical conditions in 2017 and 2019, while weaker precipitation produced only transient conditions in 2018. Circulation strength appears independent of inverse/classical condition, and scales with tidal inflow rate (the upper limit on the exchange flow) consistent with tidal pumping as the dominant forcing mechanism. These results establish a seasonally varying description of SDB's tidally averaged circulation, with relevancy to residence times, water quality management, and potential responses to future changes to freshwater input.

2.1 Introduction

While the density gradients of classical estuaries are dominated by salinity gradients, the density gradients of estuaries with weak or inconsistent freshwater input, called low-inflow

estuaries (LIEs), have meaningful contributions from thermal gradients as well. This has motivated analysis of LIE exchange flow in both temperature and salinity coordinates (Lorenz et al. 2020). Given the seasonally and spatially shifting gradients observed in LIEs (e.g., Wolanski 1986; Nidzieko and Monismith 2013), examining the longitudinal circulation is a necessary component for understanding the ocean-estuary exchange of an LIE.

LIEs in urbanized environments are particularly susceptible to poor water quality. With minor and seasonal freshwater input, tidal processes and density-driven circulation are the main drivers of exchange with the ocean, leading to long residence times and hypersaline conditions near the estuary head. These conditions, combined with urban runoff and legacies of unregulated waste disposal, can impair water quality to the point of damaging sensitive estuarine ecosystems and creating unsafe conditions for recreational, commercial, and governmental use. LIEs are also sensitive to changes in the climate system: alterations to the freshwater budget due to precipitation, heating, and dam management, along with changes to sea level, temperature, and salinity, can shift estuary water properties, modifying import and export of water and nutrients and potentially impacting the estuary ecosystem (Scheffer et al. 2001; Andersen et al. 2009; Fong and Kennison 2010; Cloern and Jassby 2012; Schettini et al. 2017; Walter et al. 2018; Taherkhani et al. 2023). A thorough understanding of the physical processes that drive LIEs is therefore necessary for their stewardship as they face increasing pressure from changes at each of their boundaries (ocean, river, land, and atmosphere).

San Diego Bay (SDB) is an urbanized estuary in San Diego County, California, located a few kilometers north of the US/Mexico border. Freshwater input is intermittent and seasonal, with maximum tributary flow rates of $\approx 50\ m^3 s^{-1}$ in winter and early spring. This contributes to the bay's hypersalinity and long residence times. Long residence times are of particular concern due to the bay's pollution levels. There remains legacy pollution sorbed to the estuarine sediment including components from raw sewage (Delaney 1965), PAHs and PCBs (Neira et al. 2018), and metals (Komoroske et al. 2012), as a result of military and industrial discharge before state and federal environmental regulations in the second half of the twentieth century. SDB is jointly

managed by the San Diego Unified Port District and the United States Navy, which have used the estuarine regimes described by Largier et al. (1996) to define hydrographic regions for biological sampling (Largier et al. 1997; Sorensen et al. 2013; U.S. Department of the Navy, Naval Facilities Engineering Command Southwest and Port of San Diego 2013) and bay management. The seasonal diversity and distribution of biological communities has been shown to be related to temperature and salinity gradients in SDB (Harding et al. 2025), consistent with the influence of salinity on species composition found in hypersaline estuaries more broadly (Getz and Eckert 2023). Understanding the physical drivers of circulation in SDB is therefore directly relevant to ongoing water quality and ecological management efforts.

Exchange processes on tidal timescales have been well investigated in SDB, with tidal pumping identified as the dominant process (Chadwick and Largier 1999a; Chadwick et al. 1996). Inverse density and concentration gradients in the bay have been noted in observational studies (Chadwick et al. 1996; Deheyn and Latz 2006), and a two cell circulation structure has been identified in both drifter observations and modeling work (Hammond and Wallace 1982; Chu and Kyriakidis 2011), both common circulation structures seen in LIEs (Largier et al. 1997; Largier 2023). However, tidally averaged exchange and circulation are more difficult to quantify, requiring longer time series and finer spatial resolution (Lemagie et al. 2022). Observational studies in SDB are further limited by the duration of surveys and the constraints on mooring deployment in a busy trade port and military harbor (Wickliffe et al. 2024). Prior model studies simulated SDB using depth-averaged barotropic models over day to month long periods, precluding calculation of volume fluxes and seasonal exchange structure (Shrestha et al. 1997; Wang et al. 1998; Chu and Armstrong 2005; Chu et al. 2006; Wang et al. 2011; Chu and Kyriakidis 2011).

The present study addresses these limitations using three years of output from a three-dimensional baroclinic, realistic hydrodynamic model, enabling application of the Total Exchange Flow (TEF) framework (MacCready 2011) to quantify volume fluxes and locate the seasonally shifting boundary between circulation cells. This is the first model study, to our knowledge,

to use the joint T/S TEF framework (Lorenz et al. 2020) to examine the temporally-varying longitudinal circulation structure in a seasonally inverse LIE.

2.2 Methods

2.2.1 Study Site Description

San Diego Bay is an urbanized (≈25 km long, ≈3 km wide, <20 m maximum depth), microtidal (≈1.7 m tidal range), seasonally inverse LIE in a Mediterranean climate region. Thorough descriptions of the bay can be found in Browning et al. (1973) and Chadwick and Largier (1999a). The bay has a narrow mouth, bordered to the west by Point Loma, and to the east by Zuniga Jetty, an approximately 2300 meter rock jetty, with inflow directed northward. Moving into the bay, the channel completes a nearly 180 degree turn clockwise, bordered seaward by Coronado Island and Silver Strand Beach (Fig. 2.1). Three watersheds surround the bay: Pueblo San Diego, Sweetwater, and Otay. The Sweetwater River and the Otay River near the bay head are the main freshwater sources, although many smaller creeks such as Chollas Creek, Paleta Creek, and Switzer Creek also carry freshwater and are important stormwater drainage and pollutant loading sites (Schiff and Carter 2007).

2.2.2 San Diego Bight Model

Model Description

The San Diego Bight, including SDB, was simulated using the Coupled Ocean Atmosphere Wave Sediment Transport (COAWST) Modeling System (Warner et al. 2010; Kumar et al. 2012), which couples the 3D hydrodynamic Regional Ocean Modeling System (ROMS) (Shchepetkin and McWilliams 2005) with the Simulating WAves Nearshore (SWAN) wave averaged model (Booij et al. 1999). A full description of the model setup can be found in Wu et al. (2020). Analysis of tracer transport and surfzone/innershelf exchange using this model has been included in multiple studies (e.g., Wu et al. 2021b,a,c), and the December 12 2016 to

December 25 2019 hindcasts used here were also analyzed in Feddersen et al. (2021); Brasseale et al. (2023) to examine coastal water quality.

A series of four nested models were run, from coarse (Level 1) to fine (Level 4) resolution, with the highest resolution Level 4 model used in this study's analysis. For the hindcast simulations presented here, Level 1 receives boundary and initial conditions from the California State Estimate (CASE) solution (Zaba et al. 2018), while the subsequently smaller and finer models receive their boundary and initial conditions from the previous (Level 1 solutions are used for Level 2, Level 2 solutions are used for Level 3, and the Level 3 solutions are used for Level 4). The first 5-9 days of the Level 4 simulation are likely impacted by model spin-up.

The Level 4 grid is 15×36 km, extending from just north of Point Loma in San Diego, US to south of Punta Bandera in Tijuana, MX. The horizontal grid resolution stretches from 110 m at the offshore boundaries to 7.8 m at the finest resolution. The finest resolution is along the coastline (in the cross-grid direction) and at the Tijuana River Estuary (TJRE) mouth in the along-grid direction, resulting in 486×1142 grid cells in the horizontal. This stretched grid results in bay resolution varying from $\approx$7.8 to 50 m in the cross-grid direction, and $\approx$30 to 80 m in the along-grid direction. NOAA $\frac{1}{3}$-arc second coastal digital elevation model is used for the Level 4 model bathymetry.

North American Mesoscale (NAM) surface flux fields are used as atmospheric forcing for all model levels (surface wind, air temperature, relative humidity, air pressure, precipitation, shortwave and longwave radiation). Evaporation is calculated in ROMS using the COARE 3.0b algorithm (Fairall et al. 2003). Within SDB, the model receives freshwater input from the Otay and Sweetwater Rivers. The Otay and Sweetwater discharge is estimated by multiplying the observed flow rate of the San Diego River (USGS gauge) by the ratio of the drainage areas. The Level 4 model also receives freshwater input from Punta Bandera, and the Tijuana River Estuary (TJRE) as described in Feddersen et al. (2021). River input temperature is estimated with a 30-day lowpass of observed temperature in Oneonta Slough in the TJRE. Level 4 also includes realistic wave forcing with boundary conditions provided by the Coastal Data Information

Program. Modeled properties are saved at hourly snapshots.

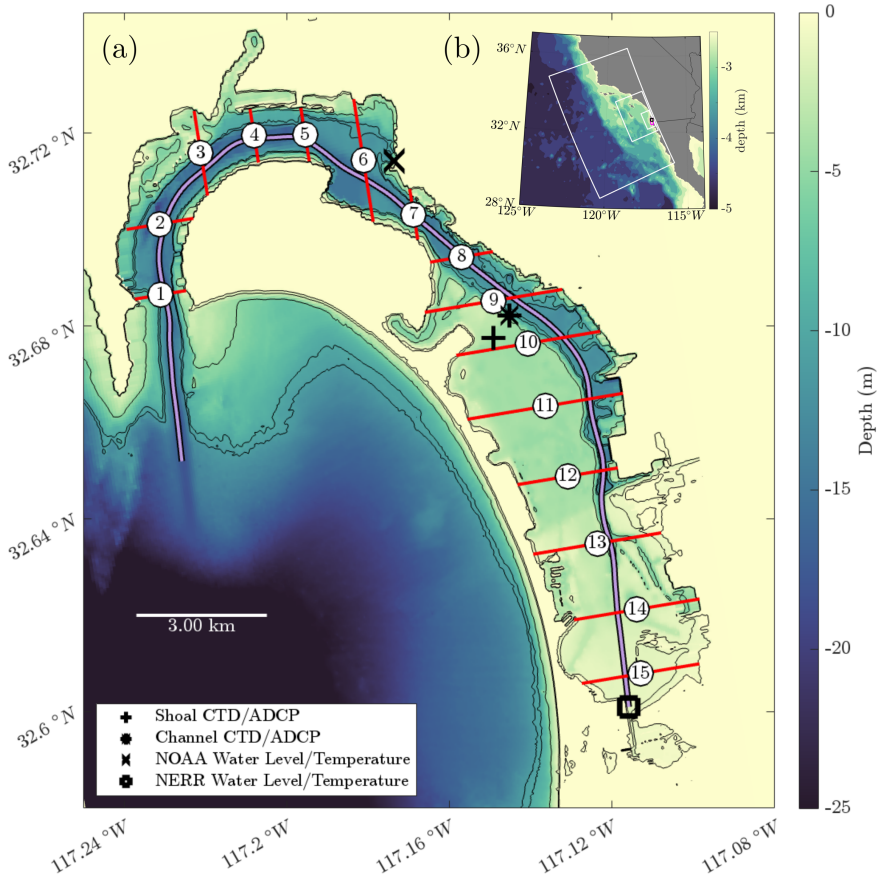


Figure 2.1. **(a)** A Map of the portion of the San Diego Bight model bathymetry around San Diego Bay. The color shows depth in meters, referenced to mean sea level. Depth contours are shown at 0, -1, -5, -10, and -11 meters. Locations where the model was validated are shown as markers. Numbered red lines show the locations of extracted bay cross-sections. The purple line shows the extracted thalweg section. **(b)** Map of nested model domains on the west coast of the United States and Mexico. Levels 1 through 3 are shown as white boxes (with Level 1 being the largest). Level 4 is shown as a small black square inside Level 3.

Model Validation

Moored CTDs and ADCPs were deployed between June and November 2017, midway through the bay in the shoals, and on the slope of the main channel (Figure 2.1, labeled as Shoal CTD/ADCP and Channel CTD/ADCP). CTD deployment began June 6 and ended November 21. ADCPs were deployed twice (Deployment 1: June 30 through August 7, Deployment 2: August 13 through November 17). Further technical detail on the CTD and ADCP deployments

can be found in Rodriguez (2019). Hourly and tidally-filtered water level, salinity, temperature, depth-averaged principal axis velocities (velocities, relative angles, major and minor axes), and the depth-varying velocities along the depth-averaged principal axis were compared.

Long term monitoring stations over all three model years were also available. The South Bay NERR monitoring station (Code TJRSBWQ, square on Fig. 2.1) measurements of water level, salinity, and temperature were used for validation for all three model years. NOAA monitoring station (ID: 9410170, X on Fig. 2.1) measurements of water level and temperature were used for validation for all three model years. Temperature data was not available from late summer 2018 through early spring 2019. Water level was adjusted to account for the inverse barometer effect using air pressure data from the same monitoring station. Modeled and observed tidal constituents were compared using the UTide MATLAB package (Codiga 2011). The amplitude and phase of the tidal constituents prescribed at the boundary of the Level 1 model (M_2, S_2, N_2, K_2, O_1, P_1, Q_1, K_1, M_4, and M_6) were compared. Confidence intervals for the constituent amplitudes and phases are calculated using the default settings of the UTide package.

All comparisons were assessed using a series of skill metrics including: mean absolute error, percent error, root mean square error, the coefficient of determination (r^2), and the Willmott skill score (Willmott 1981).

2.2.3 Analysis

Salinity, temperature, and velocities were extracted along 15 cross-sections on the model v-grid (see red lines in Fig. 2.1). u-grid and rho-grid variables were interpolated to the v-grid, following MacCready (2011) and MacCready et al. (2021). These quantities were also extracted at 200 vertical profiles, approximately equally spaced (0.13 km) along the thalweg, from the NERR monitoring station at the mouth of the Sweetwater River, to about 4 km past the bay mouth into the ocean (see purple line in Fig. 2.1).

The structure of cross-sectionally averaged properties in SDB was examined in relation to freshwater inputs and outputs (river flow, precipitation, evaporation), and the Coastal Upwelling

Transport Index (CUTI; Jacox et al. 2018) at the nearest latitude bin, $32°N$. River flow was extracted and summed from the model input for the two freshwater sources into the bay that were included in the model, the Otay and Sweetwater Rivers. Precipitation was extracted from the model input as well. Evaporative flux was calculated from model atmospheric inputs using the Coupled Ocean–Atmosphere Response Experiment (COARE) version 3.0b bulk algorithm used for surface fluxes by ROMS within COAWST (Fairall et al. 2003).

The TEF method (MacCready 2011) using both salinity (S) and temperature (T), as well as density (ρ) is applied to the cross sections similar to what is described in Lorenz et al. (2020) to examine net fluxes and to determine circulation cells and possible circulation cell boundaries. Tidally-averaged volume and mass transports through a cross-section, $Q_\rho(\rho)$ and $F_\rho(\rho)$ respectively, are given by equations 2.1 and 2.2. $A(\rho)$ is the area of a cross section with density greater than ρ. u is the velocity normal to the cross-section, oriented positive into the estuary towards the head. Angle brackets indicate tidal averaging, done numerically using a Godin filter (Godin et al. 1981).

$$Q_\rho(\rho) = \left\langle \int_{A(\rho)} u \, \mathrm{d}A \right\rangle \tag{2.1}$$

$$F_\rho(\rho) = \left\langle \int_{A(\rho)} \rho u \, \mathrm{d}A \right\rangle \tag{2.2}$$

The volume and mass exchange profiles per unit density, q_ρ and f_ρ respectively, are given by equations 2.3 and 2.4

$$q_\rho = \frac{-\partial Q_\rho}{\partial \rho} \tag{2.3}$$

$$f_\rho = \frac{-\partial F_\rho}{\partial \rho} \tag{2.4}$$

Dividing densities between layers are determined using the method described in Lorenz et al.

(2019). Integrating the exchange profiles over inflowing and outflowing layers gives bulk inflowing and outflowing volume and mass transports $Q_\rho^{in}, Q_\rho^{out}$, and $F_\rho^{in}, F_\rho^{out}$.

$$Q_\rho^{in} = \int q_\rho \Big|_{in} d\rho, \quad Q_\rho^{out} = \int q_\rho \Big|_{out} d\rho \tag{2.5}$$

$$F_\rho^{in} = \int f_\rho \Big|_{in} d\rho, \quad F_\rho^{out} = \int f_\rho \Big|_{out} d\rho \tag{2.6}$$

Transport-weighted densities are calculated as:

$$\rho_{in} = \frac{F_\rho^{in}}{Q_\rho^{in}}, \quad \rho_{out} = \frac{F_\rho^{out}}{Q_\rho^{out}} \tag{2.7}$$

The difference between inflowing and outflowing transport-weighted density $\Delta\rho = \rho_{in} - \rho_{out}$ defines the type of exchange through a cross-section. When $\Delta\rho > 0$, the exchange is classical, and when $\Delta\rho < 0$, the exchange is inverse. Equations 2.1 through 2.7 are similarly defined in salinity and temperature coordinates for salinity and temperature transports, and ΔS and ΔT respectively.

Note that in previous studies, the order of operations for time-integrated bulk transports is to integrate in time within each density (or salinity or temperature) bin before integrating the transport in each density layer. In this system, the range of S, T, ρ the system covers is very large and changes substantially throughout the year which can cause some issues with this averaging approach. Thus, here, the order of operations will be reversed for integration over nonconsecutive segments of circulation which are characterized as classical, inverse, classical at the head / inverse at the mouth, and classical at the mouth / inverse at the head. This decision and issues around it are explored in the discussion section.

Given the known difficulties in calculating fluxes, particularly from measurements (Lemagie et al. 2022), two additional metrics that are expected to represent circulation cells and circulation cell boundaries are investigated. The boundary between the thermal and hypersaline

regimes occurs where the longitudinal tidally averaged density is at a minimum and the density gradient $\partial_x \rho$ goes to zero (Largier et al. 1996). This boundary is calculated at each timestep of the model output. This boundary can also be estimated using a spatially varying compensation ratio c similar to the ratio used in Hearn (1998):

$$c = \frac{\alpha \mid \partial_x T \mid}{\beta \mid \partial_x S \mid} \tag{2.8}$$

where α is the thermal expansion coefficient, and β is the haline contraction coefficient. Longitudinal differences ∂_x are calculated between each adjacent cross-section. x increases toward the head, so positive $\partial_x S$ indicates an inverse salinity gradient, while positive $\partial_x T$ indicates a classical temperature gradient. Where $c > 1$, the dominant contribution to longitudinal differences in density is temperature. Where $c < 1$, the dominant contribution to longitudinal differences in density is salinity. Where $c = 1$, the contributions of temperature and salinity are balanced, and there is a transition between thermal and hypersaline regimes. Both $\partial_x \rho$ and c are calculated using cross-sectionally averaged quantities to assess where $\partial_x \rho = 0$ and where $c = 1$.

2.3 Results

2.3.1 Validation

Temperature, Salinity, and Water Level

Model skill was assessed at four sites (Table 2.1): the long-term NOAA and NERR monitoring stations (Fig. 2.1), and two shorter-duration ADCP moorings (Channel and Shoal), each deployed in two segments over 2017 (Channel: Jun 30-Aug 7 and Aug 13-Nov 17; Shoal: Jun 6-Aug 7 and Aug 13-Nov 17).

Hourly modeled temperatures compared well with observations, with r^2 values ranging from 0.31 to 0.96 across all four sites (Table 2.1). Skill was highest at the long-term NERR and NOAA stations ($r^2 = 0.96$ and 0.82, respectively) and lower at the Channel and Shoal CTD sites ($r^2 = 0.31$ and 0.79). Subtidal temperatures (Fig. 2.2**a**) showed a similar pattern, with r^2 ranging

from 0.26 to 0.97, and Willmott skill scores of at least 0.57 at every site. Percent errors were small throughout (0.15-5.89%), indicating that the model reproduces both the magnitude and the seasonal and subtidal evolution of temperature well, with reduced skill for the shorter CTD deployments.

Salinity skill was weaker than temperature skill. Hourly salinities compared with r^2 values ranging from 0.08 to 0.64, and tidally filtered salinities from 0.01 to 0.84 (Fig. 2.2**b**). The NERR station showed the strongest agreement ($r^2 = 0.64$ hourly, 0.84 tidally filtered), while the Shoal site showed the weakest ($r^2 = 0.08$ hourly, 0.01 tidally filtered), although percent error was comparable (1.8-4.4%) across sites. The model appears to capture the mean salinity reasonably well at all sites but doesn't do a good job reproducing the salinity variability at the Shoal site, which is in shallower water than the Channel site.

Hourly water levels compared with r^2 values ranging from 0.78 to 0.98, reflecting the dominance of tidal forcing and the model's strong representation of the dominant tidal constituents Fig. 2.4. Subtidal water levels showed considerably lower skill ($r^2 = 0.01$-0.44), reflecting the small residual signal that is harder to resolve. Subtidal water levels showed a consistent seasonal cycle at the NOAA and NERR stations in both model and observations, and RMSE remained small (0.04-0.25 m).

Across all three variables, the lowest skill scores consistently came from the CTD deployments rather than the long-term NOAA/NERR stations. This is at least in part due to their short deployments and fewer samples: each CTD deployment period ranged from five weeks to around three months (Channel/Shoal dep1: Jun-Aug; dep2: Aug-Nov), compared to the multi-year NOAA/NERR records. It may also reflect the CTD sites' location in the shoals and along the channel slope, where property gradients are stronger and sensitive to small errors in the model circulation.

Table 2.1. Skill scores for modeled temperature, salinity and water level, co-located with data sources. Skill scores for the hourly values are given along with scores for the tidally filtered values in parentheses.

Site	Variable	Unit	N	RMSE	% Error	r^2	Willmott skill
NOAA	Temperature	°C	20903 (20868)	1.12 (1.02)	0.15 (0.18)	0.82 (0.85)	0.95 (0.96)
NOAA	Water Level	m	26617 (24114)	0.09 (0.04)	0.00 (0.55)	0.97 (0.44)	0.99 (0.80)
NERR	Temperature	°C	25115 (25420)	1.20 (1.08)	3.99 (3.97)	0.96 (0.97)	0.98 (0.98)
NERR	Salinity	PSU	22720 (22450)	3.61 (2.73)	4.41 (4.41)	0.64 (0.84)	0.67 (0.76)
NERR	Water Level	m	25481 (25420)	0.10 (0.07)	0.59 (2.99)	0.97 (0.21)	0.99 (0.64)
Channel	Temperature	°C	6416 (6136)	1.69 (1.65)	5.89 (5.81)	0.31 (0.26)	0.60 (0.57)
Channel	Salinity	PSU	3260 (2980)	0.75 (0.75)	2.19 (2.20)	0.16 (0.39)	0.31 (0.31)
Channel	Water Level	m	6416 (6136)	0.07 (0.04)	2.83 (40.11)	0.98 (0.01)	1.00 (0.45)
Shoal	Temperature	°C	3739 (3599)	1.22 (1.16)	4.54 (4.44)	0.79 (0.81)	0.82 (0.82)
Shoal	Salinity	PSU	1966 (1686)	0.64 (0.63)	1.83 (1.85)	0.08 (0.01)	0.26 (0.22)
Shoal	Water Level	m	3739 (3599)	0.25 (0.04)	0.58 (0.82)	0.78 (0.07)	0.94 (0.51)

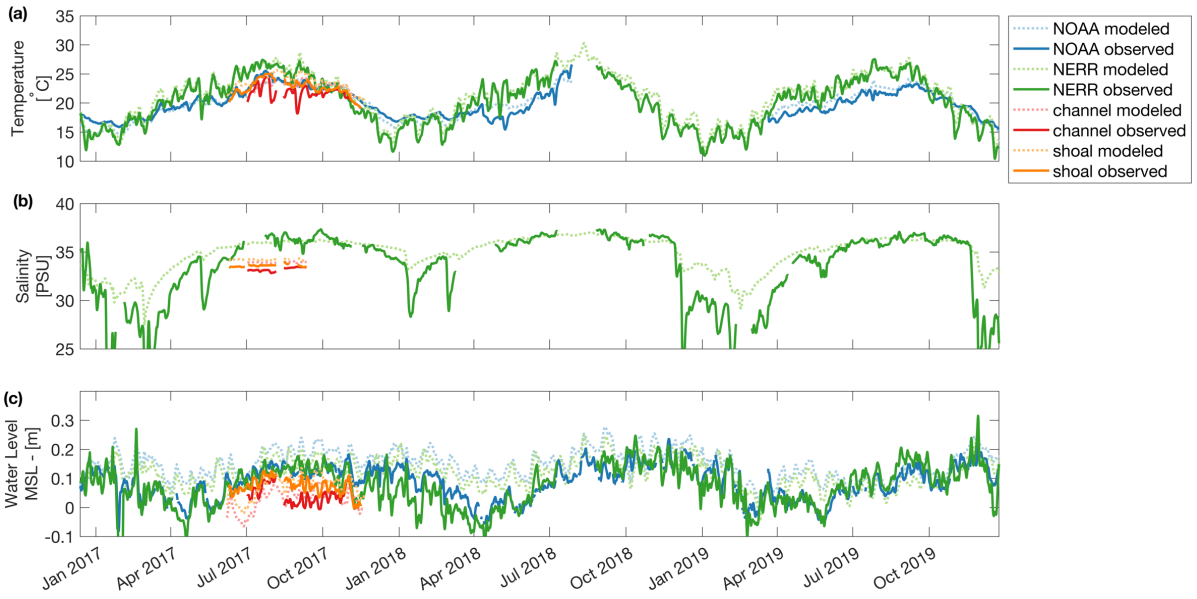


Figure 2.2. Tidally filtered observed and modeled **(a)** temperature , **(b)** salinity, and **(c)** water level. Observations are shown at the four locations labeled in Fig. 2.1, along with co-located model values.

Currents

Depth-averaged principal-axis velocities at the channel site agreed well with observations across both deployments (Table 2.2). Principal-axis orientations differed from observations by 13.4° and 23.2° for deployments 1 and 2, respectively, consistent with the along-channel

currents, and hourly r^2 values were 0.96 for both deployments, with Willmott skill of 0.99 at both; depth-varying skill (not shown) remained strong throughout the water column, indicating the model reproduces both the strength and the vertical structure of channel currents well. This agreement held after removing the tidal signal: the depth-averaged tidally averaged (Godin filtered) residual velocity also corresponded strongly between observations and model ($r^2 = 0.79$ and 0.60 for each deployment), with comparable mean magnitude and the same sign in both records (0.02 $\mathrm{m\,s^{-1}}$) Fig. 2.3**(a)** and **(b)**.

The shoal site showed weaker agreement than the channel site. Principal-axis angle differences were larger (29.1-35.4°) and percent errors much higher (48-259%), possibly reflecting the smaller mean velocity magnitudes at this site (Table 2.2). The mean flow along the principal axis was oriented opposite the observations in the model: the model captured the tidal-band variability with skill comparable to the raw comparison, but the subtidal residual circulation disagreed in sign from the observations, with the observed subtidal velocity persistently negative ($\approx -0.2\ m\ s^{-1}$) against a persistently positive modeled value ($\approx 0.3\ m\ s^{-1}$) with a weaker depth-averaged correspondence ($r^2 = 0.42$ and 0.55 for each deployment) Fig. 2.3**(c)** and **(d)**. Given the weak mean flow at this location, this sign disagreement may reflect local variations in the residual circulation not resolved by the model.

Table 2.2. Validation of the principal axis model velocities co-located with each ADCP deployment. Principal-axis angle difference (observation - model), observed and modeled (in parentheses) mean velocity along their principal axes, and depth-averaged skill metrics for the hourly values. Skill scores for the tidally averaged values are in parentheses.

Mooring / deployment	N	Angle diff. (°)	Mean vel. (ms^{-1})	RMSE	% Error	r^2	Willmott skill
Channel 1	1946 (1876)	13.4	0.025 (0.021)	0.032 (0.005)	3.00 (12.64)	0.96 (0.79)	0.99 (0.90)
Channel 2	551 (481)	23.2	0.022 (0.026)	0.032 (0.008)	3.27 (23.17)	0.96 (0.60)	0.99 (0.80)
Shoal 1	1479 (1409)	35.4	-0.019 (0.029)	0.071 (0.050)	48.20 (259.55)	0.79 (0.42)	0.90 (0.18)
Shoal 2	2345 (2275)	29.1	-0.014 (0.023)	0.056 (0.040)	37.23 (271.31)	0.86 (0.55)	0.94 (0.16)

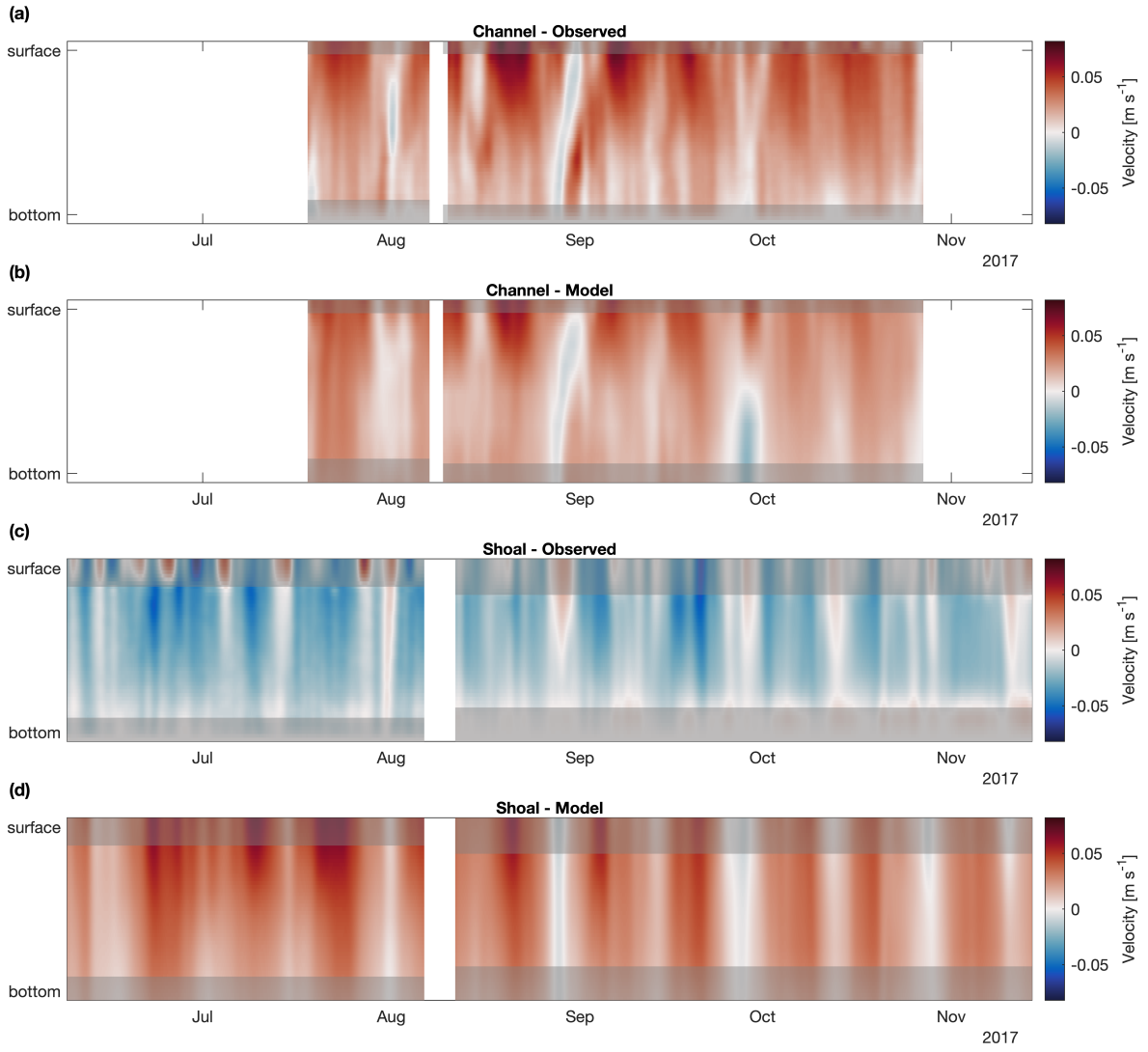


Figure 2.3. Tidally averaged observed and modeled velocities at the channel and shoal moorings shown in Fig. 2.1**(a)**. Panels **(a)** and **(b)** show both channel deployments, observed and modeled, respectively. Panels **(c)** and **(d)** show both shoal deployments, observed and modeled, respectively. Shaded regions at the surface and bottom of each axis indicate where velocities were extrapolated following Giddings et al. (2014).

Tidal Constituents

Comparison of the ten prescribed tidal constituents at the NOAA station shows that the model reproduces the tides in SDB well (Fig. 2.4). Amplitude percent errors were smallest for M_2, N_2, and K_1 (0.21%, 0.70%, and 0.89%, respectively), which are the three largest-amplitude constituents in the system. The largest amplitude error occurred in the M_4 constituent (20.55%).

Phases were best represented for M_2, S_2, and P_1 (0.05%, 0.60%, and 0.90% error, respectively), with the largest phase error in M_6 (125%). Confidence intervals on the observed and modeled amplitudes were small relative to the amplitudes themselves (not visible at the scale of Fig. 2.4).

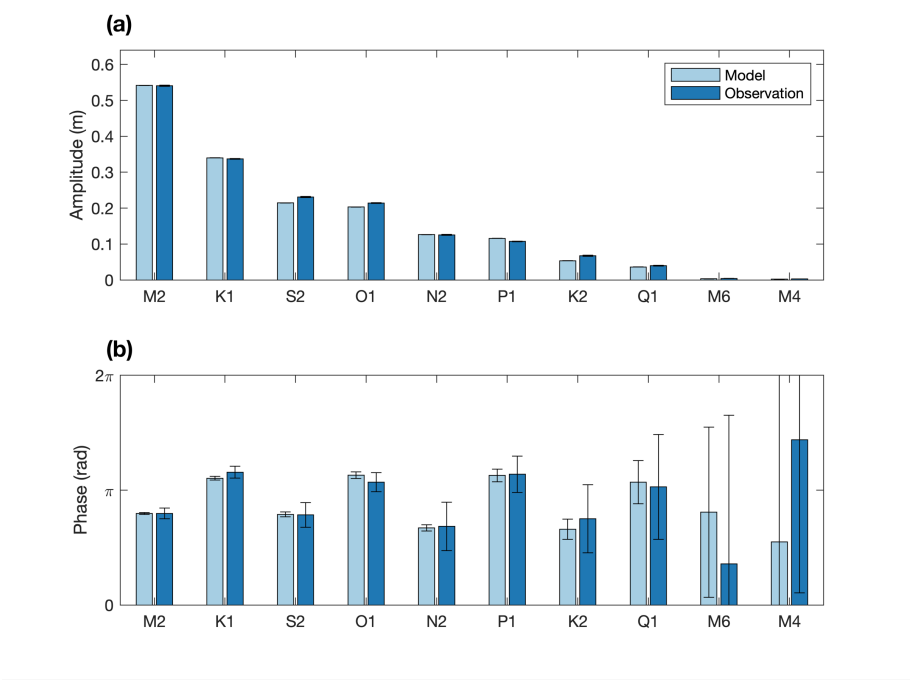


Figure 2.4. Comparison of modeled (in light blue) and observed (in dark blue) tidal constituents at the NOAA monitoring station on the northeast side of SDB. Panel **(a)** shows the tidal constituent amplitudes. Panel **(b)** shows their relative phases. Confidence intervals are shown at the top of each bar. Note that the confidence intervals in the constituent amplitudes are too small to see.

2.3.2 Environmental Conditions

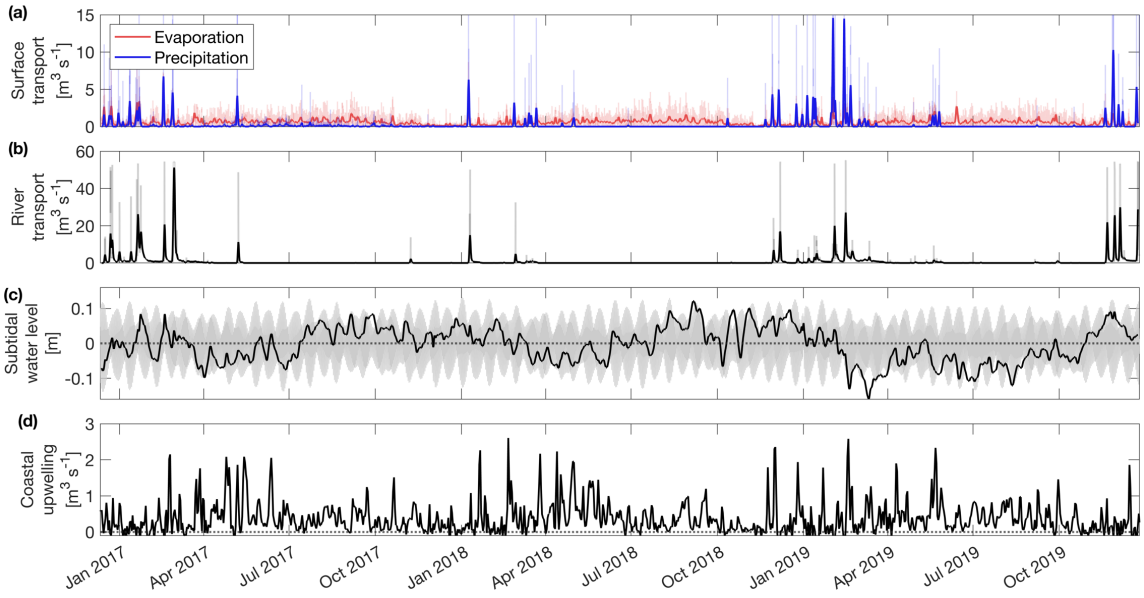


Figure 2.5. Relevant environmental variables over the three year model period. Thicker lines show tidally filtered values. Panel **(a)** shows the surface flux rate of evaporation (red) and precipitation (blue). Panel **(b)** shows the model input stream flux rate summed over the Otay and Sweetwater Rivers. Panel **(c)** shows modeled hourly and tidally filtered water level at the mouth. Hourly water level is scaled down by a factor of 10 to clearly show the spring-neap cycle. Panel **(d)** shows the daily CUTI index, representing coastal upwelling.

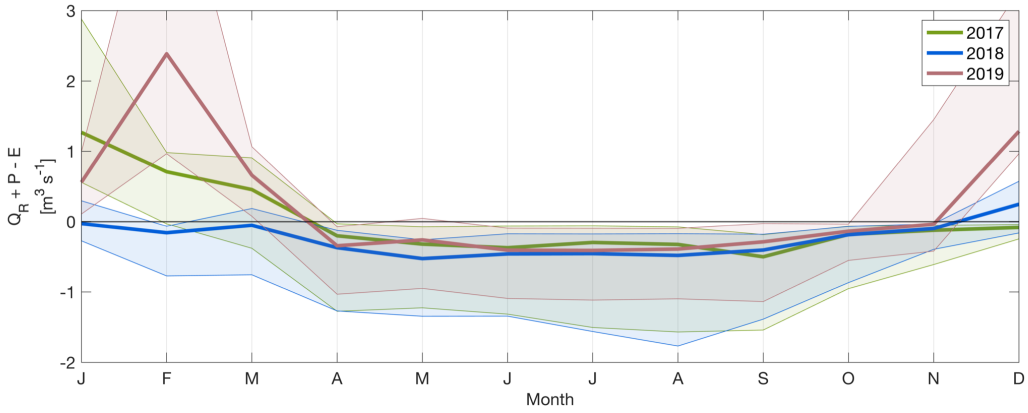


Figure 2.6. Monthly median freshwater transport $[m^3 s^{-1}]$ in model years 2017 through 2019. The shaded areas show the 75th and 25th percentile for each month.

Freshwater input through precipitation and river flow occur mostly in winter Fig. 2.5**(a)**. River flow is negligible except following precipitation events Fig. 2.5**(b)**. Tidally filtered water level shows a seasonal cycle, with lowest water levels in spring and early summer Fig. 2.5**(c)**, generally aligning with annual peaks in coastal upwelling Fig. 2.5**(d)**. Evaporation exceeds precipitation and river flow for the months of April through November for all three years Fig. 2.6. August had the greatest monthly mean evaporation of 0.78 $m^3 s^{-1}$, and December had the lowest monthly mean evaporation of 0.40 $m^3 s^{-1}$. The wettest year was 2019, while 2018 was the only year with net freshwater loss. Annual total freshwater inputs for 2017, 2018, and 2019 were approximately 16700×10^3 m^3, -5100×10^3 m^3, 31000×10^3 m^3, respectively.

2.3.3 Longitudinal Property Structure

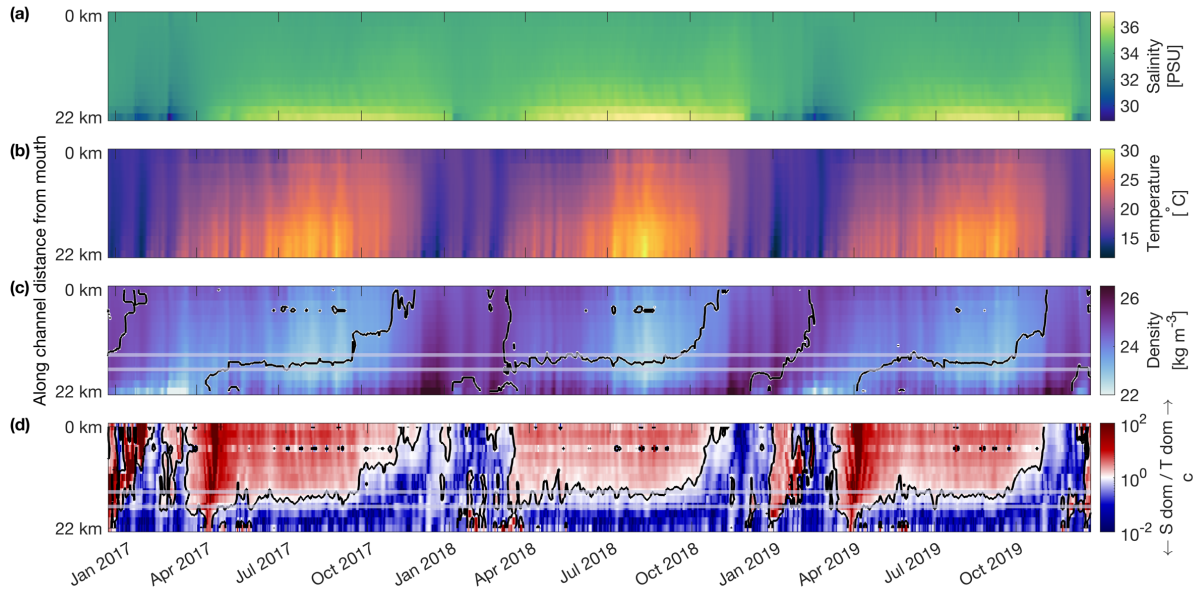


Figure 2.7. Cross-sectionally averaged modeled water properties (**(a)** salinity, **(b)** temperature, **(c)** density), and **(d)** compensation ratio c, over the three year model period. Each panel has longitudinal distance as the y-axis, with the estuary mouth at the top (at 0 km), and the head at the bottom (at 22 km). Cross-sectionally averaged density **(c)**, includes a black contour marking density extrema at each time step (generally the density minimum). The compensation ratio c **(d)**, includes a black contour where $c = 1$, marking longitudinal transitions between salinity and temperature dominated density difference. The gray lines on panels **(c)** and **(d)** indicate the along-channel locations of sections 10 and 12, as labeled in Fig. 2.1.

The cross-sectionally averaged modeled water properties show a combination of seasonal cycles and transient events (Fig. 2.7). SDB is hypersaline (increasing salinity monotonically toward the head) for most of the model period, with peak salinities and salinity gradients mid to late summer (Fig. 2.7**(a)**). The peak salinity during the model period is around 37.8 PSU near the head on August 12, 2018, with a maximum subtidally averaged salinity gradient of 0.12 PSU/km on August 8, 2018. The positive sign of this salinity gradient indicates an inverse salinity gradient. Minimum salinity gradients occur during early winter and spring. Briefly during midwinter, SDB becomes hyposaline throughout the bay, corresponding with precipitation events. The strongest hyposaline gradients occur on March 2, 2017, and February 16, 2019, with gradients of -0.13 PSU/km and -0.12 PSU/km. The average salinity gradient over the model period is 0.06 PSU/km.

SDB is hyperthermal (temperature increasing monotonically toward the head) throughout the bay during the summer, with a peak temperature around $31.5°C$ near the head on August 10, 2018 (Fig. 2.7**(b)**). The maximum temperature gradient is $0.43°C/km$ on July 8, 2017, with the positive sign indicating this is in the classical sense (increasing temperature moving into the bay). Minimum temperature gradients occur in late November, early December, as well as February and early March. SDB is hypothermal during winter, with a peak hypothermal gradient of $-0.19°C/km$ on January 3, 2019. The average temperature gradient over the model period is $0.15°C/km$.

Density varies seasonally, with the lowest full bay average density anomalies of around 22 $kg\ m^{-3}$ midsummer through fall, and the highest in winter of around 26 $kg\ m^{-3}$ before precipitation events occur (Fig. 2.7**(c)**). Due to the combined effects of temperature and salinity (as seen by c near 1, Fig. 2.7**(d)**), there is a persistent mid-estuary density minimum during summer. During the drier year of 2018, the density minimum starts mid-estuary, while in the two wetter years (2017 and 2019), the density minimum moves from the head in the winter and spring to mid estuary during the summer and fall. While the cross-sectionally averaged view captures the bay-wide seasonal cycle, examining the depth varying properties along the thalweg

provides insight into the along-channel structure.

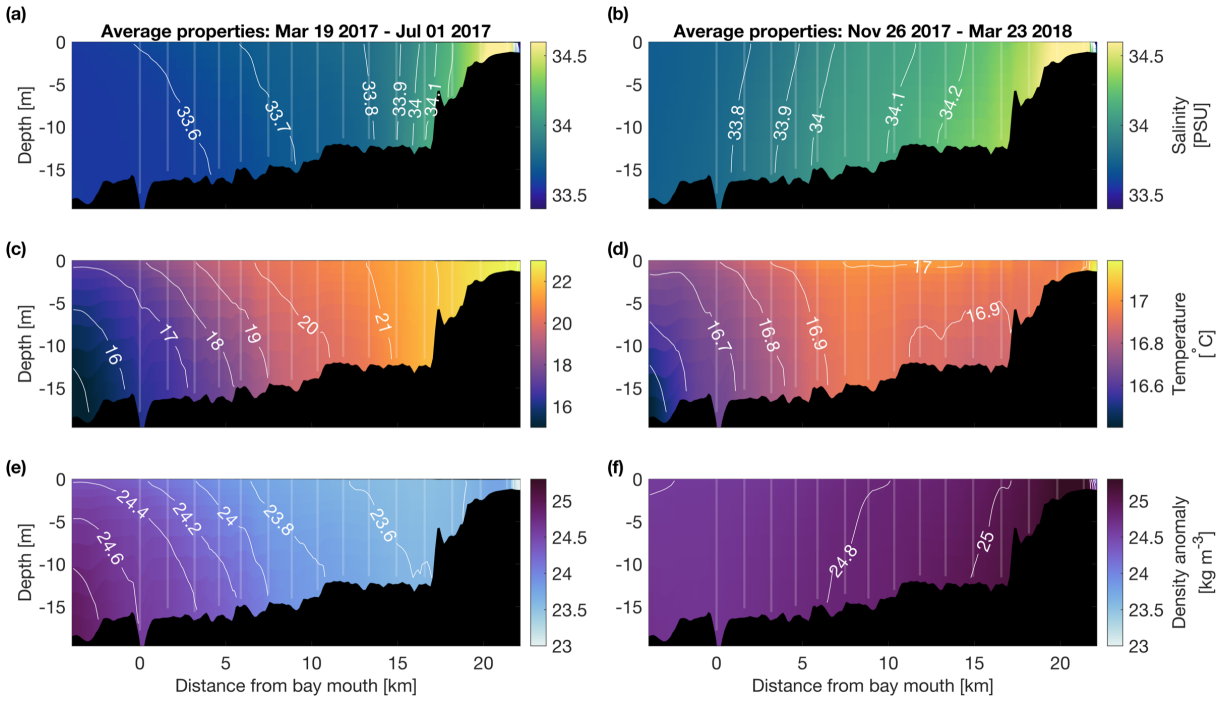


Figure 2.8. Average modeled water properties (**(a)** and **(b)** salinity, **(c)** and **(d)** temperature, **(e)** and **(f)** density) along the thalweg over two time periods. Property contours are shown in white with labeled values. Faint vertical lines indicate intersections with the cross-sections used for the TEF analysis. Note the difference between the color limits of the temperature panels.

Time-averaged modeled water properties along the thalweg show temporally and longitudinally varying vertical structure that indicates seasonally shifting estuarine exchange regimes. For instance, there are clear differences between the spring/early summer period of March 19, 2017 through July 01, 2017, and the fall/winter period of November 26, 2017 through March 23, 2018 (Fig. 2.8).

In the spring/early summer period, isohaline, isothermal, and isopycnal lines are tilted toward the ocean, particularly closer to the bay mouth. Headward of the 33.8 isohaline, approximately 7 km from the head, the isohaline and isopycnal lines become tilted slightly toward the head, suggesting a potential change in the direction of the gravitational circulation. Closer to the head, at the mouth of the Sweetwater River, there is a slight freshening, but the bay is overall hypersaline. The salinity maximum may act as a salt plug, although it is worth noting that the

location of the change in the tilt direction of the isohalines is seaward of the location of the salinity maximum, suggesting that the ”density plug” is due to the combined effects of salinity and temperature. Despite the hypersalinity, the warm and light estuarine water overlays the ocean water out past the mouth as is seen in positive estuaries, suggesting a classical circulation. Stratification is largest in the ocean-ward half of the estuary becoming fairly well mixed in the landward half.

In the fall/winter period, the bay is colder and saltier. The isohalines and isopycnals are tilted toward the head while the isotherms tilt towards the mouth, and there is a temperature maximum between 16.9 and 17$^{\circ}C$, about 13 km from the head. The estuarine water now behaves as expected for a negative estuary, underlaying the ocean water out past the mouth. Overall the vertical stratification and longitudinal density gradients are weak throughout the bay and significantly weaker than during the spring/early summer period.

2.3.4 Estuarine Total Exchange Flow and Transport-weighted Properties

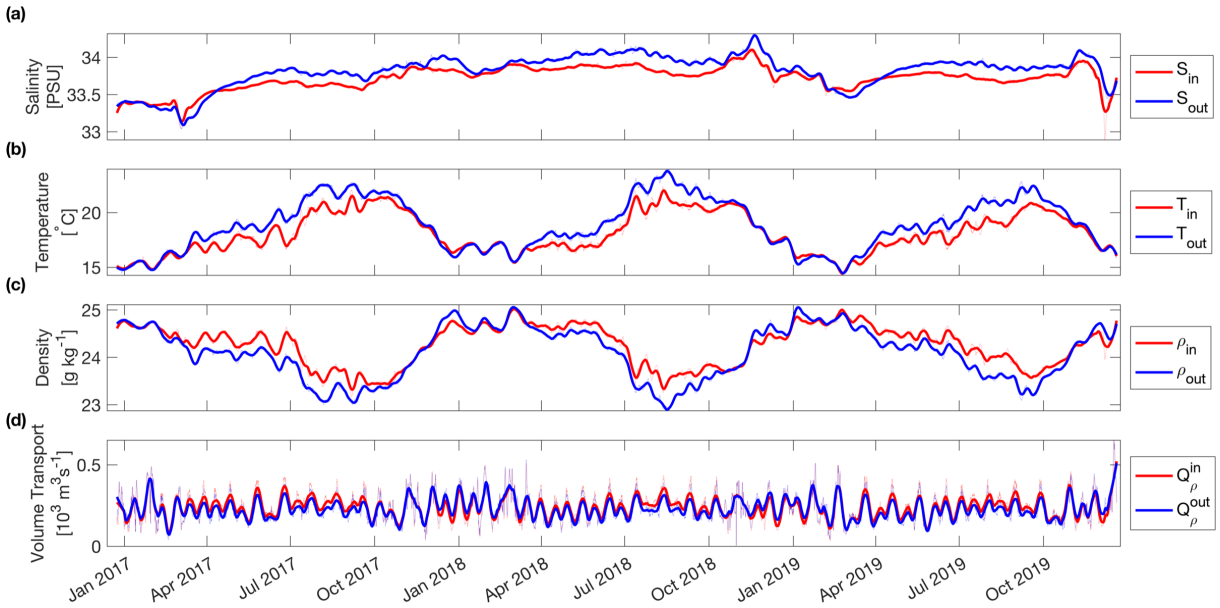


Figure 2.9. Time series of quantities at the mouth (section 1) of SDB. Panel **(a)** shows the spring/neap tidal envelope. Panel **(b)** shows the Brunt–Väisälä frequency N^2, representing stratification. Panel **(c)** shows the inward and outward volume transport through the cross section, where the sign of Q_ρ^{out} is flipped for visual comparison. Panels **(d)** - **(f)** show the inward and outward transport weighted salinities, temperatures, and densities, respectively. In panels **(c)** - **(f)**, red indicates the inward flowing values, and blue indicates the outward flowing values. All values have additional arbitrary smoothing (15 days) for readability, with the unsmoothed TEF time series shown faintly in the background.

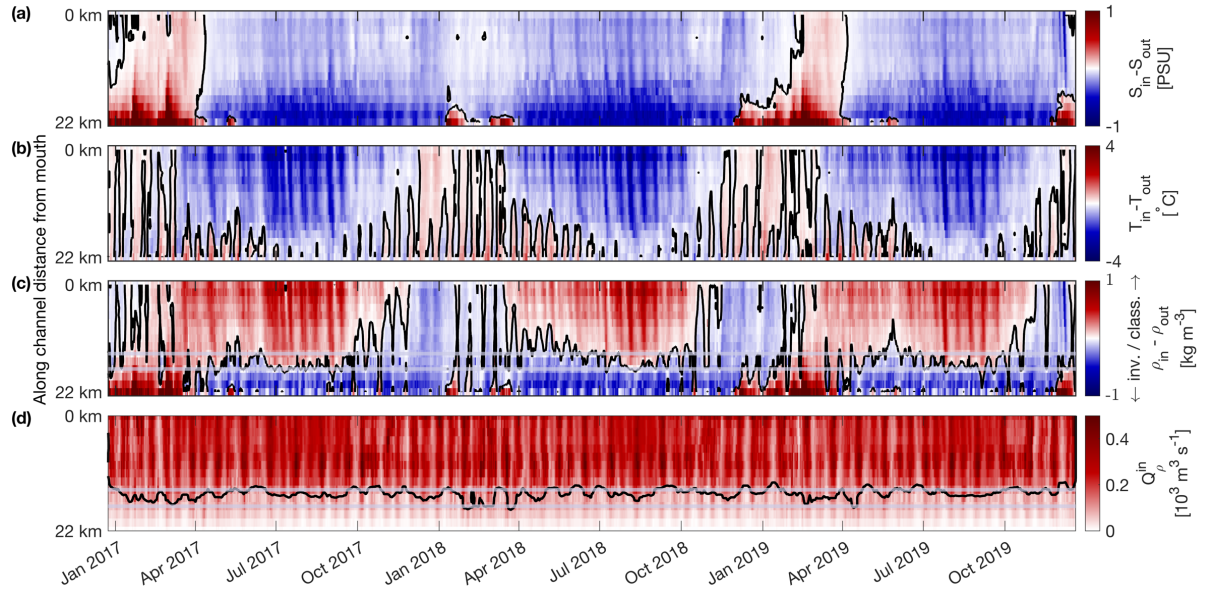


Figure 2.10. Differences between inflowing and outflowing transport-weighted mean properties (**(a)** salinity, **(b)** temperature, **(c)** density), and **(d)** inward volume transport for model years 2017-2019. Each panel has longitudinal distance as the y-axis, with the estuary mouth at the top (at 0 km), and the head at the bottom (at 22 km). The inflowing - outflowing differences on panels **(a)**-**(c)** are such that negative values indicate exchange in a sense consistent with hypersaline **(a)**, hyperthermal **(b)** and inverse **(c)** circulation. Contours on panels **(a)**-**(c)** mark where there is no difference between inflowing and outflowing values. The contour on panel **(d)** is at $0.1 \times 10^3\ m^3\ s^{-1}$. The two gray lines on panels **(c)** and **(d)** indicate the along-channel locations of sections 10 and 12, as labeled in Fig. 2.1.

SDB's longitudinal gradients are in part set by ocean-estuary exchange at the mouth. Seasonal salinity variability in the exchange at the mouth was minimal Fig. 2.9**(d)**. The salinity difference of the exchange is mostly inverse, with outflowing salinity generally greater than inflowing salinity. Mean ΔS at the mouth was -0.08 PSU. Outflowing salinity briefly fell below inflowing salinity during precipitation and stronger river flow in early 2017 and 2019 (Fig. 2.5**(a)**,**(b)**). Peak ΔS at the mouth during these reversals was 0.19 PSU on March 19, 2017, and 0.13 PSU on March 14, 2019.

S_{out} is greatest when stratification is highest, following both spring and neap tides, particularly summer through early fall (S_{out} ranges from 33.56 to 34.00 PSU, mean 33.76 PSU, over June–October pooled across 2017–2019; it peaks at 34.00 PSU on 21 July 2018, when

$N^2 \approx 6.2 \times 10^{-4}\,\mathrm{s}^{-2}$ roughly 3 to 4 times the typical spring/neap mean), while Q_{in} and Q_{out} are greatest during spring tide, when stratification is lowest (mean $Q_{in} \approx 0.4 \times 10^3\,\mathrm{m}^3\,\mathrm{s}^{-1}$ and $Q_{out} \approx -0.4 \times 10^3\,\mathrm{m}^3\,\mathrm{s}^{-1}$ at spring tide vs. $Q_{in} \approx 0.3 \times 10^3\,\mathrm{m}^3\,\mathrm{s}^{-1}$ and $Q_{out} \approx -0.2 \times 10^3\,\mathrm{m}^3\,\mathrm{s}^{-1}$ at neap tide, coinciding with $N^2 \approx 1.6 \times 10^{-4}\,\mathrm{s}^{-2}$ at spring vs. $2.2 \times 10^{-4}\,\mathrm{s}^{-2}$ at neap).

The time-varying transport-weighted mean properties calculated using TEF through the 15 cross-sections (Fig. 2.10) show the seasonal cycle of circulation patterns suggested by the along-thalweg vertical structure (Fig. 2.8). The circulation is hypersaline (saltier outflow, Fig. 2.10(a)) through every cross-section for most of the model period, becoming fully hyposaline in early 2017, late 2018 through early 2019, and briefly near the head in early 2018 and late 2019. The strongest hypersaline flows appear near the head in late summer and early fall, with peak ΔS values ranging from -0.8 to -0.9 PSU. Hyposaline flows appear during precipitation events with peak ΔS values ranging from 2.1 to 6.7 PSU.

The circulation is hyperthermal (warmer outflow) for most of the model period near the mouth, except late fall through early winter, when it becomes hypothermal Fig. 2.9**(e)** and Fig. 2.10**(b)**. Mean ΔT at the mouth was $-0.89°C$. The circulation swings between hyperthermal and hypothermal near the head aligned with the spring/neap cycle, with hypothermal flows during neap. The circulation is most hypothermal during spring (March and April) near the head with ΔT peaks ranging from 1.7 to 2.2 $°C$. The circulation is most hyperthermal during late summer (end of July / early August) near the head, with peak ΔT values ranging from -3.3 to -3.8 $°C$. During late fall / early winter when most of SDB is hypothermal, ΔT values are smaller, with peak ΔT values around $0.91°C$.

This temperature and salinity variability produces classical circulation (positive $\Delta\rho$) near the mouth and inverse circulation (negative $\Delta\rho$) near the head during most of the year (Fig. 2.9**(f)** and Fig. 2.10**(c)**), consistent with the salinity inverse, temperature dominated exchange at the mouth noted above. Inverse density differences extend throughout the estuary during late fall / early winter, while brief classical periods appear near the head during winter freshwater events, with a much smaller extent during dry 2018 than in wetter 2017 and 2019. Peak classical

conditions near the mouth in late July / early August exhibit $\Delta\rho$ values around 0.72 to 0.82 $kg\ m^{-3}$, while inverse conditions near the head at that time giving $\Delta\rho$ values around -0.45 to -0.60 $kg\ m^{-3}$. Late fall / early winter inverse conditions across the entire bay are weaker, with typical $\Delta\rho$ values ranging from -0.2 to -0.5 $kg\ m^{-3}$. Transient classical circulation in winter and spring can give peak $\Delta\rho$ values ranging from 2.2 to 5.3 $kg\ m^{-3}$. The $\Delta\rho = 0$ contour marking the cell boundary sits mid-estuary, closer to the head (between sections 10 and 12 marked with gray lines in Fig. 2.10**(c)** and **(d)**, $\approx$ 16 km from the mouth) through late spring, summer, and early fall, then shifts to the mouth and disappears during late fall/early winter. This boundary moves approximately with the spring-neap cycle, though the phase is inconsistent.

2.3.5 Circulation Strength

The overall circulation strength (Fig. 2.10**(d)**) is relatively consistent over time. There is a small seasonal weakening in late summer and early fall, consistent with the reduced density gradients during that period. However, the dominant temporal variability in circulation strength follows the spring-neap cycle, visible across all cross sections, with strongest exchange during spring tide (Fig. 2.10**(d)**). If the exchange flow strength is examined during different exchange conditions (e.g., classical vs inverse conditions vs bimodal), across all conditions, volume transports weaken from the mouth toward the head, reflecting the geometry of the bay (Fig. 2.11). Near the mouth, transports in all circulation states are approximately $0.3 \times 10^3\ m^3\ s^{-1}$ with Q^{ρ}_{out} during inverse conditions exceeding that during classical conditions by approximately $0.02 \times 10^3\ m^3\ s^{-1}$ suggesting that circulation strength is not strongly sensitive to the sign of the density gradient. The similarity in transport magnitude across all four states is consistent with tidal forcing playing a dominant role, rather than the baroclinic pressure gradient, as the primary control on exchange strength in SDB.

Examining the inward transport with respect to the tidal inflow rate (the upper limit of the exchange flow) provides insight into the forcing mechanism of the exchange flow (Chen et al. 2012; MacCready and Geyer 2024). If Q^{in}_{ρ} scales like Q_{prism}, then the exchange flow behaves

consistently with tidal pumping. If Q_ρ^{in} scales more like Q_{prism}^{-1}, the exchange flow behavior is more consistent with the gravitational circulation. For all exchange states observed in the model at the mouth and near the head, Q_ρ^{in} does scale like Q_{prism}, with values ranging from 0.06 (when inverse near the head) to 0.18 (when classical near the head) Fig. 2.12. This is lower than ratios of approximately 0.3 reported for the Salish Sea (MacCready and Geyer 2024), and the 0.2 to 0.65 range reported for the Hudson River and Merrimack River estuaries (Chen et al. 2012). This indicates an overall less efficient exchange flow than these other estuaries.

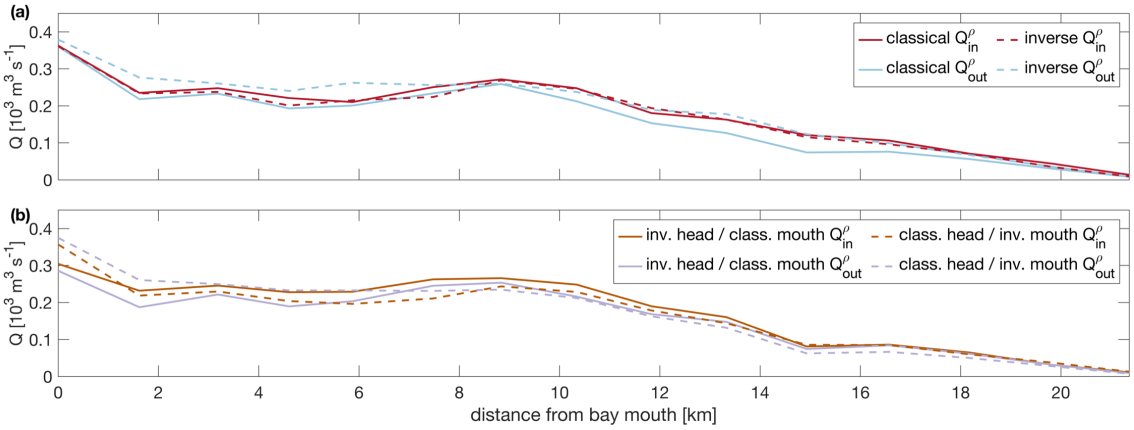


Figure 2.11. Time mean inward and outward volume transport through each SDB cross section for four exchange conditions. Panel **(a)** shows the transport for classical (solid lines), and inverse conditions (dashed lines). Red lines are inward transport, and light blue lines are outward transport. Panel **(b)** shows the transport when the exchange is inverse at the head / classical at the mouth (solid lines), and classical at the head / inverse at the mouth (dashed lines). Brown lines are inward transport, light purple lines are outward transport.

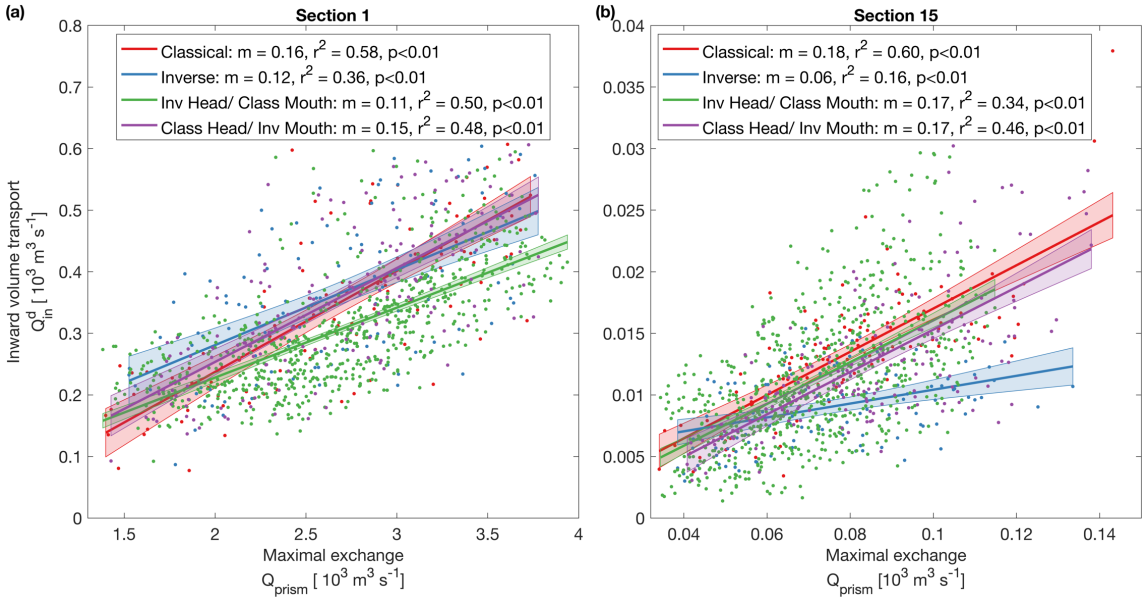


Figure 2.12. Maximal exchange (tidal inflow rate) against inward volume transport for SDB model cross sections 1 (panel **(a)**) and 15 (panel **(b)**). Data is colored and regressed according to the SDB exchange condition: classical, inverse, inverse near the head / classical at the mouth, and classical near the head / inverse at the mouth. r^2 and p-values for the regressions are displayed in each panel legend.

2.4 Discussion

2.4.1 Physical Interpretation

The seasonal cycle of circulation states in SDB reflects the competing and spatially varying contributions of temperature and salinity to the longitudinal density gradient. As spring progresses into summer, warming of the shallow inner bay drives a thermally dominated classical circulation cell near the mouth (Fig. 2.10**(c)**), where the compensation ratio c exceeds unity, indicating that temperature gradients dominate the density gradient in that region (Fig. 2.7**(d)**). Near the head, however, salinity accumulated through evaporation during the preceding summer remains elevated (Fig. 2.7**(a)**), maintaining an inverse salinity gradient that suppresses classical circulation (Fig. 2.10**(c)**). This spatial asymmetry produces the two cell structure, with classical exchange near the mouth and inverse exchange near the head.

Through summer, continued evaporation builds salinity throughout the bay. When the

water cools in fall, the elevated salinity is sufficient to produce a density gradient that drives inverse circulation across the entire bay (Fig. 2.10(**c**)), with $c < 1$ throughout, indicating salinity-dominated inverse density differences (Fig. 2.7(**d**)). This agrees with the observations of Chadwick et al. (1996). These transitions occur over the course of one to two spring-neap cycles.

Brief reversals to classical circulation occur in late winter and early spring, driven by precipitation events sufficiently strong to overcome the hypersaline winter conditions. The duration and spatial extent of these classical episodes correspond to the magnitude of freshwater input, with the wetter years (2017 and 2019) producing the most persistent classical conditions and the driest year (2018) producing only transient classical circulation. The sensitivity of the circulation state to interannual differences in precipitation may have implications for long term changes in bay residence time under the effects of the climate crisis.

The tidally averaged exchange flow estimated in this study is broadly consistent with previous observational estimates in SDB. Chadwick et al. (1996) estimated the tidally averaged bottom inflow on the order of 0.1 $m\ s^{-1}$ and tidally averaged surface outflow on the order of 0.05 $m\ s^{-1}$ at the mouth over a tidal cycle in May 1994. Multiplying these values by half of the mean cross-sectional area of the mouth from the San Diego Bight model ($\approx 4800\ m^2$), we can approximate the tidally averaged inflow and outflow as 480 $m^3 s^{-1}$ and 240 $m^3 s^{-1}$, respectively. The TEF derived volume transports are of the same order of magnitude. Differences between observational and model derived exchange estimates are expected given the known sensitivity of flux calculations to the number and placement of moorings across a cross-section (Lemagie et al. 2022). Eulerian estimates of volume transports are expected to be somewhat smaller than TEF transports due to cancellations at vertical levels as water level varies (MacCready 2011).

2.4.2 Implications for Climate Variability

The sensitivity of the circulation to interannual variability in precipitation demonstrated here has implications for the long-term trajectory of SDB under the effects of the climate crisis. The contrast between 2018, the driest model year, in which only transient classical circulation

occurred, and 2019, the wettest, in which persistent classical conditions developed in late winter and early spring, suggests that projected changes in the regional precipitation regime could substantially alter the seasonal circulation cycle. Precipitation over California is projected to decrease in frequency but increase in intensity, with more severe droughts interspersed with episodic extreme events (Norris et al. 2021; Kalansky et al. 2018). This could reduce the duration and frequency of classical circulation events in SDB, potentially increasing residence times and exacerbating hypersaline conditions. Warmer ocean temperatures along the Southern California coast (Siedlecki et al. 2021) and reduced alongshore winds favoring downwelling (Xiu et al. 2018) could further modify the offshore oceanic conditions driving exchange at the bay mouth. Sea level rise of a meter or more projected by the end of the 21st century (Kalansky et al. 2018) may additionally alter tidal mixing and stratification in ways that are difficult to predict, as the outcome depends on the interplay between changed tidal prism geometry, salinity gradients, and strain-induced periodic stratification. These compounding pressures underscore the importance of understanding the baseline circulation dynamics described in this study as a reference point for future monitoring and management of SDB.

2.4.3 Future Work

Several directions for future work follow naturally from this study. Most immediately, the model should be run in diagnostic mode, outputting hourly-averaged rather than hourly snapshot properties, to enable rigorous salt and volume budget analysis. Additional observational campaigns with long term mooring deployments at multiple along-channel locations would provide the validation data necessary to more thoroughly evaluate the modeled tidally averaged longitudinal density gradients. A simulation with a more complete validation would provide a stronger foundation for the future analyses described below.

The physical processes driving the seasonal circulation transitions identified here warrant further investigation. In particular, the relative contributions of tidal pumping and gravitational circulation to the exchange flow should be quantified following the decomposition approach of

MacCready and Geyer (2024), building on the analysis presented here of Q_ρ^{in} and Q_{prism}. The role of strain-induced periodic stratification in modulating the spring-neap variability of the circulation boundary, and the lateral circulation described by Rodriguez (2019), should also be examined to build a more complete picture of the three-dimensional exchange structure in SDB.

2.4.4 Applications for SDB Management

The circulation patterns described here have direct relevance to ecological and management applications. Residence and flushing times, which previous estimates place in a wide range of 2 to 100 days without capturing seasonal variability (Largier et al. 1997; Chadwick and Largier 1999a; Delgadillo-Hinojosa et al. 2008), should be calculated using TEF quantities (Lemagie and Lerczak 2015) to characterize their spatiotemporal variability. Efflux-reflux fractions should be estimated to determine what proportion of water is exchanged horizontally rather than recycled vertically within each circulation cell (MacCready et al. 2021). Finally, the seasonal circulation patterns identified here should be compared with datasets on the spatial and temporal distribution of estuarine biota in SDB (Harding et al. 2025), to evaluate the ecological relevance of the circulation boundaries identified in this study.

2.4.5 TEF Numerical Issues in LIEs

In previous applications of the TEF framework, bulk transport quantities are computed by first integrating fluxes over time within each density bin, then integrating across inflowing and outflowing density layers (MacCready et al. 2021). In this study, the order of operations was reversed: transports were integrated over inflowing and outflowing layers at each time step, and then the transport was integrated over time. This reversal was necessary to avoid cancellations between inflowing and outflowing density bins, due to varying transport weighted mean densities in disconnected time periods in each circulation state presented in Fig. 2.11. More broadly, we note that the conventional order of operations may introduce cancellation errors in systems where transport-weighted mean densities (or S, T) vary rapidly in time. In a classical estuary

where salinity dominates density and transport-weighted mean salinities are relatively stable, time-integration within density bins is unlikely to produce significant cancellation. However, in LIEs where both temperature and salinity contribute to density and their relative contributions shift seasonally, inflowing and outflowing components at a given density may alternate in sign over time, leading to underestimation of exchange when time-integrated within bins. To our knowledge this issue has not been formally investigated, and further analysis is warranted, particularly for LIE applications of the TEF framework.

2.5 Conclusion

Three years of model output of SDB was analyzed using the TEF framework to examine SDB's longitudinal circulation structure. A seasonally varying pattern was found, with a two cell structure during summer (with classical circulation near the mouth and inverse circulation near the head), and full-bay inverse circulation during winter. This seasonal cycle reflects the shifting balance between thermally- and salinity-dominated density gradients along the estuary, with the boundary between circulation cells shifting accordingly. Interannual variability in this pattern was tied to variability in precipitation, with the driest year (2018) producing only transient reversals to classical circulation and the wettest year (2019) sustaining classical conditions for extended periods, suggesting that projected shifts in regional precipitation could substantially alter the seasonal circulation cycle in the future. In applying the TEF framework to this seasonally inverse LIE, it was identified that the conventional order of operations for time-integrating bulk transports can introduce cancellation errors where transport-weighted properties vary rapidly in time, motivating a revised approach that may be relevant to TEF applications in other LIEs. Together, these results provide a baseline description of SDB's circulation dynamics that can inform future observational campaigns, refine estimates of residence and flushing times, and serve as a reference point for water quality and ecological management efforts in the bay.

2.6 Acknowledgements

Chapter 2, in full, is currently being prepared for submission for publication of the material. Anidjar, Niv; Giddings, Sarah N.; Rodriguez, Angelica. The dissertation author was the primary investigator and author of this material.

Chapter 3

Recruitment and Residence in San Diego Bay

Abstract: Oyster recruitment integrates larval supply, settlement, and survival, and is therefore a widely used indicator of habitat suitability in estuaries. In San Diego Bay (SDB), a heavily urbanized, seasonally inverse, low-inflow estuary, the native *Ostrea lurida* co-occurs with the invasive *Magallana gigas*, but the impacts of environmental conditions on recruitment of the two species have not been compared. This study combines a decade (2016-2025) of settlement tile deployments at five sites and multiple tidal elevations with local environmental time series (air temperature, wind speed, precipitation, water temperature, salinity, water level, satellite sea surface temperature, and coastal upwelling), and with three summers (2017-2019) of realistic hydrodynamic model output used to simulate offline Lagrangian particle tracking and estimate along-bay residence time. Recruitment density of both species generally increased from the mouth toward the head, coincident with bay-exit residence times that increased from less than 10 days near the mouth to 60-180 days near the head. Interannual variability was large, and most univariate regressions against seasonal medians and interquartile ranges were not significant. *M. gigas* recruitment increased with the previous winter's median daily minimum air temperature ($R^2 = 0.66$, $p = 0.004$) and decreased with winter median wind speed ($R^2 = 0.48$, $p = 0.026$), whereas *O. lurida* recruitment increased with winter median offshore sea surface temperature ($R^2 = 0.48$, $p = 0.025$) and decreased with water-year median upwelling ($R^2 = 0.49$, $p = 0.025$), consistent with the higher tidal elevation and greater aerial exposure of *M. gigas*. Residence time was longest in 2018, the driest year on record here, but interannual recruitment did not track interannual residence time.

3.1 Introduction

Oysters are an essential component of estuary ecosystems. Oyster beds provide habitat for other organisms (Farmer et al. 2023; Dame and Olenin 2005; Dutertre et al. 2010), remove contaminants by filtering the water (Sanjeeva Raj 2008), protect the shoreline from erosion by dispersing wave energy (Piazza et al. 2005; Meyer et al. 1997; Grabowski et al. 2012), and provide nutrients for organisms that consume them such as fish, and migratory birds (Beck et al. 2011; Grabowski et al. 2012). Certain oyster species, such as *Magallana gigas* (previously *Crassostrea gigas*), are economically and aquaculturally important (Shatkin et al. 1997; Ruesink et al. 2005).

In response to shifting spatial distributions of oysters, and population declines of native species, there have been significant efforts to track changes in oyster populations, and identify mechanisms and thresholds in environmental conditions for population stability (Pritchard et al. 2015; Wasson et al. 2015). A common method for determining population health is to measure oyster recruitment (Kennedy et al. 2011; Schulte and Burke 2014; Zacherl et al. 2015). Oyster recruitment measures a combination of oyster settlement over a deployment period, as well as the survival of settled oysters during a deployment period. Rather than measuring oyster larval production, recruitment represents an integrated measure of environmental conditions for developing oysters (Carson 2010; Gosling 2015). Oyster recruitment has been studied with respect to location, tidal elevation, water temperature, and substrate (both natural and constructed), predation pressure, and other environmental filters and settlement triggers (O'Beirn et al. 1995; Lagarde et al. 2017; Tedford-Callahan et al. 2025). Temperature in particular has been shown to be of relevance to both *Ostrea lurida* and *M. gigas* recruitment, with increased recruitment and recruitment success associated with higher water temperatures (Dutertre et al. 2010; Wasson et al. 2016; Valdez and Ruesink 2017; Wolfe et al. 2024). Larval retention and oyster recruitment in estuaries have been shown to relate to residence time and ocean-estuary exchange processes (Gaines and Bertness 1992; Roegner 2000; Sponaugle et al. 2002; Deck

2010).

Wasson et al. (2016) examined the coefficient of variation (the variance normalized by the mean) of winter salinity to test the relationship between environmental heterogeneity and recruitment success, finding that greater variation is associated with less recruitment failure. Comparing recruitment directly with winter salinity, they found increased recruitment failure at sites with higher winter salinity, indicating that strong marine influence may reduce recruitment success, although the researchers note that the exact mechanism is unclear, and it may be due to colder water temperatures, or decreased larval retention in regions with lower residence times.

San Diego Bay (SDB) is a heavily urbanized, low inflow estuarine system in San Diego, California, United States. The hydrographic structure of the bay has been well described (Largier 1995; Largier et al. 1996, 1997; Chadwick and Largier 1999a,b; Rodriguez 2019). The longitudinal density structure shows hypersalinity with increasing salinity toward the head in the back bay, a thermal regime with increasing temperature toward the head, and a marine regime near the mouth with similar properties to ambient ocean conditions. These density regimes contribute to a tidally averaged circulation structure with seasonally varying inverse and classical flows (see Chapter 2).

Previous studies on residence time in SDB include (Largier et al. 1996; Chadwick et al. 2004; Chu et al. 2006; Chu and Kyriakidis 2011). Largier et al. (1996) estimated residence time from salinity observations in August 1993, with values ranging from tidal near the mouth (≈ 1 day), to around 50 days near the head. Chadwick et al. (2004) found similar values, up to about 40 days near the head, calculated using salinity from surveys throughout 2000 and 2001. Chu et al. (2006) estimated residence times ranging from 15 days in the north bay and 29 days in the south bay for methanol released in a chemical spill model in June 1993.

O. lurida is a native oyster species that has been historically harvested in San Diego. *M. gigas* is a feral species introduced to the Pacific coast of the United States for aquaculture, but has since become widespread (Wolfe et al. 2024; Padilla 2010). It was first broadly observed in San Diego in the early 2000s (Crooks et al. 2015). There have been some oyster recruitment

studies in SDB, focusing on densities across various natural and artificial substrates and tidal elevations (Tronske et al. 2018; Perog et al. 2022) and intra-decadal population proliferation linked to warming waters (Wolfe et al. 2024). However, there remain knowledge gaps related to the differences in recruitment patterns between *O. lurida*, and *M. gigas*. This study aims to compare recruitment responses of the native *O. lurida* and invasive *M. gigas* using a combination of environmental data and realistic hydrodynamic model output and a decade of *O. lurida*, and *M. gigas* oyster recruitment observations at five sites in SDB to examine the spatial and temporal recruitment patterns in the context of hydrodynamic conditions. This study seeks to address the following knowledge gaps. How does interannual variability in oyster recruitment in San Diego Bay relate to the median and interquartile range of environmental conditions (air temperature , wind velocity (Jacobsen et al. 1990), water temperature [expected positive relationship (Valdez and Ruesink 2017; Cheng et al. 2015; Wasson et al. 2016)], salinity [expected positive relationship (Ortega and Sutherland 1992; Lagarde et al. 2017)], water level [*O. lurida* recruitment greater at lower tidal elevations, *M. gigas* recruitment greater at higher tidal elevations (Fuentes et al. 2020)], upwelling [expected positive relationship (Wasson et al. 2016)], residence time) that have shown relevancy to recruitment in other studies? Are conditions during deployment, or the previous winter more strongly related to recruitment? Are there meaningful differences in these relationships for these oyster species?

3.2 Methods

3.2.1 Study Sites

San Diego Bay (SDB) is an urbanized ($\approx$25 km long, $\approx$3 km wide, $<$20 m maximum depth), microtidal ($\approx$1.7 m tidal range), seasonally inverse, low-inflow estuary (LIE), in a Mediterranean climate region. Additional description of SDB is found in Chapter 2, and in Browning et al. (1973) and Chadwick and Largier (1999a). Five sites in particular within SDB are examined, each labeled and marked with an ‘x’ in Fig. 3.1. From nearest to SDB’s mouth to

its head, the sites are as follows. The La Playa site is near the mouth of a small cove, and has soft sandy substrate along with riprap backed by a seawall. The Glorietta Bay site is in a small cove with soft sandy substrate. The E Street site is on open shore in SDB, and has soft, muddy substrate. The Grand Caribe site is on a small island and has soft muddy substrate, backed by riprap. The Chula Vista Wildlife Reserve site is on a small tied island with cobble shoreline.

3.2.2 Data Collection

Environmental Variables

Water temperature, salinity, and water level for 2016-2025 were accessed from the south bay monitoring station (ID: TJRSBWQ) through the NERR Centralized Data Management Office data portal (https://cdmo.baruch.sc.edu/dges/). The sensor is located at approximately -0.809 meters below mean lower low water level (Fig. 3.1, black square).

Daily maximum and minimum air temperature (average was not available), daily precipitation, average wind speed, and direction of 2 minute fastest winds, were accessed from the Global Historical Climatology Network's Daily (GHCND) station (ID: USW00023188) through NOAA's National Centers for Environmental Information (NCEI) (https://www.ncei.noaa.gov/cdo-web/datasets/GHCND/stations/GHCND:USW00023188/detail). The station is located at the San Diego International Airport (Fig. 3.1, black triangle). The principal axis of the wind was calculated to be oriented with a 329° bearing with respect to north (approximately north northwest, approximately oriented alongshore), and wind speed along this axis was used in this study's analysis.

Sea surface temperature (SST) was accessed from NOAA 0.25-degree Daily Optimum Interpolation Sea Surface Temperature (OISST), Version 2.1 through the NOAA NCEI data portal (https://doi.org/10.25921/RE9P-PT57). This gridded product is a synthesis of satellite data and *in situ* observations. The nearest grid cell to the bay at $32.625°N, -117.125°E$ was used. As this is an integrated satellite product, its values are more reflective offshore open ocean temperatures, rather than temperatures within SDB.

Biologically Effective Upwelling Index (BEUTI) at the 33°N bin was also accessed (Jacox et al. 2018). BEUTI represents vertical nitrate flux in 1° latitude bins, in units of $mmol\ m^{-1}\ s^{-1}$.

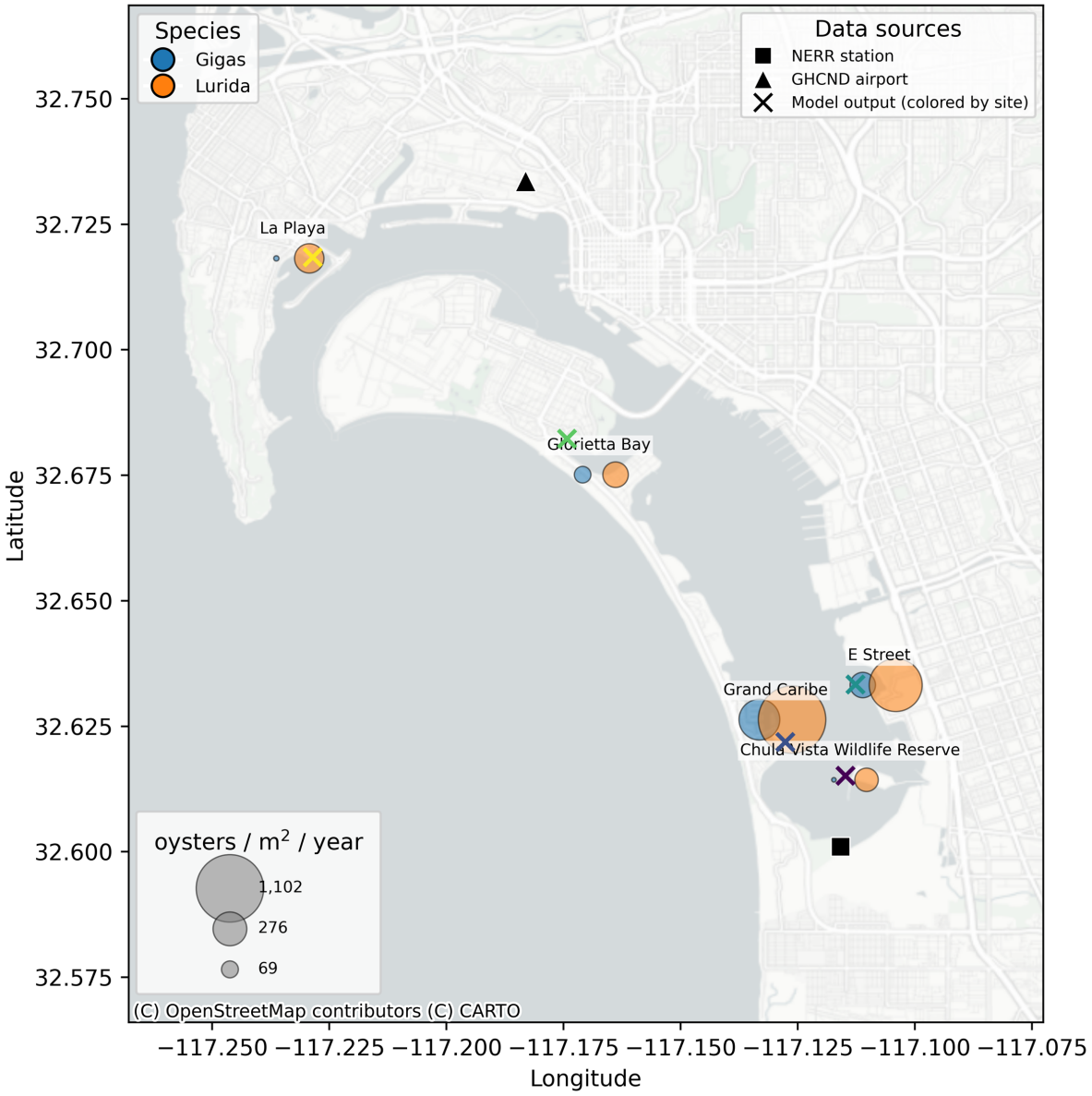


Figure 3.1. Yearly average recruitment density at each deployment site for *M. gigas* (blue) and *O. lurida* (orange), shown on a map of SDB, alongside environmental data sources. Model extraction points are colored by along-bay distance as used in subsequent figures.

Oyster Recruitment

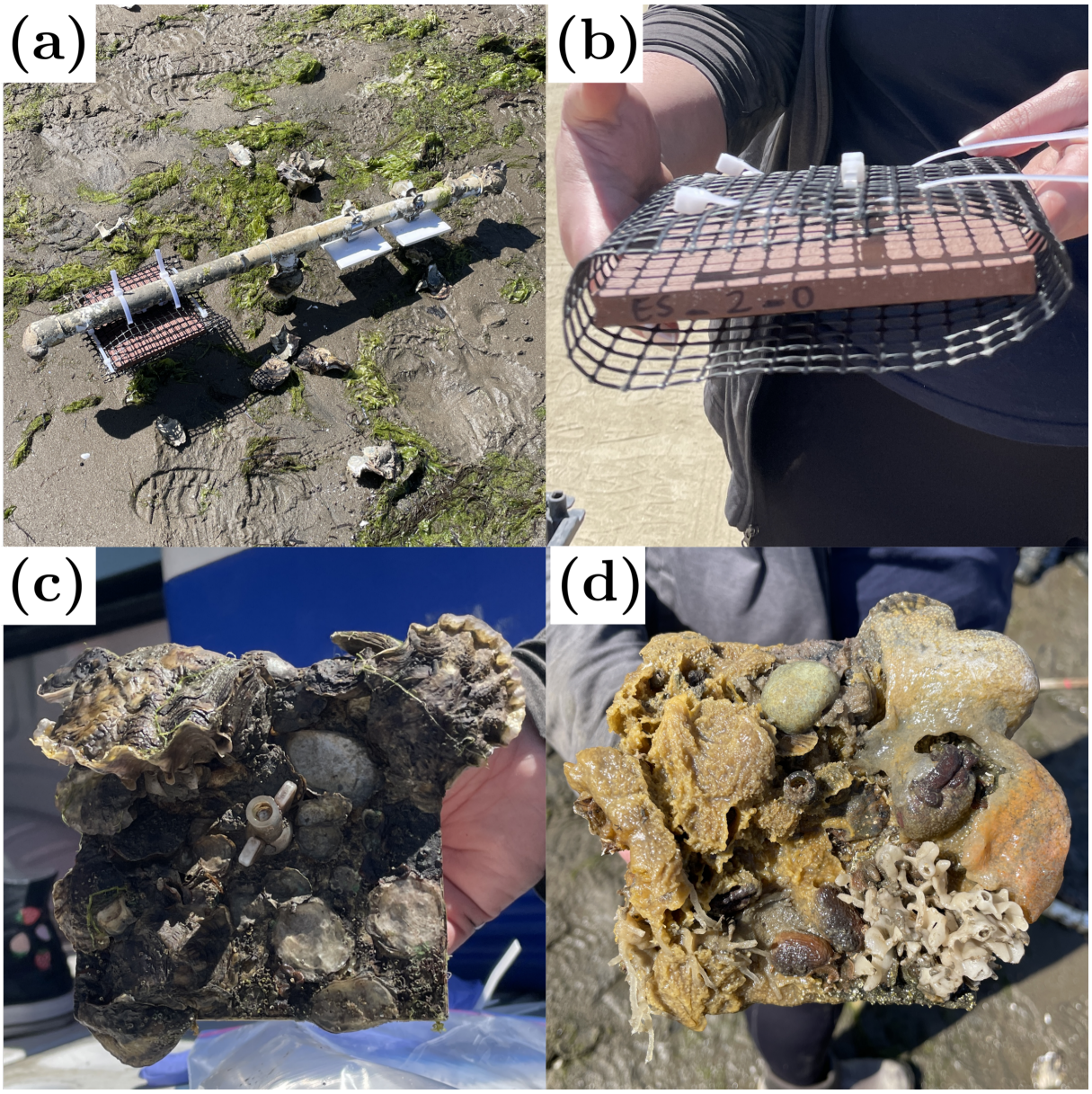


Figure 3.2. Images of oyster recruitment field setup. **(a)** PVC pipe apparatus on which a terracotta tile is suspended (left side), and two white ceramic tiles are attached (right side). **(b)** A closeup of a soon-to-be-deployed terracotta tile inside its mesh cage with zip ties in place to suspend it on the PVC pipe apparatus. **(c)** and **(d)** Two examples of post-deployment tiles, showing a variety of organisms, including oysters. **(c)** shows the fastener at the center of the tile used to attach it to the PVC pipe.

Table 3.1. Recruitment tiles by year and site. Each cell lists the tile count at each tidal elevation deployed at that site that year.

Year	Dates	La Playa	Glorietta	E Street	Grand Caribe	Chula Vista Wildlife Reserve
2016	Apr 05 Sep 16	–	3 (-0.3), 5 (+0.0), 5 (+0.3), 5 (+0.6), 6 (+0.9)	5 (-0.3), 5 (+0.0), 5 (+0.3), 5 (+0.6), 5 (+0.9)	–	–
2017	Mar 27 Sep 17	–	3 (-0.3), 5 (+0.0), 5 (+0.3), 5 (+0.6), 5 (+0.9)	5 (-0.3), 5 (+0.0), 5 (+0.3), 5 (+0.6), 5 (+0.9)	5 (+0.0), 5 (+0.6)	–
2018	Mar 28 Sep 10	–	5 (+0.0), 5 (+0.6)	5 (+0.0), 5 (+0.6)	5 (+0.0), 5 (+0.6)	–
2019	Mar 21 Sep 25	–	5 (+0.0), 5 (+0.6)	5 (+0.0), 5 (+0.6)	5 (+0.0), 5 (+0.6)	–
2020	Mar 22 Oct 18	5 (+0.0), 5 (+0.6)	–	11 (+0.0), 11 (+0.6)	–	5 (+0.0), 5 (+0.6)
2021	Mar 28 Oct 08	5 (+0.0), 5 (+0.6)	–	5 (+0.0), 5 (+0.6)	5 (+0.0), 5 (+0.6)	5 (+0.0), 5 (+0.6)
2022	Mar 27 Sep 08	–	–	5 (+0.0), 5 (+0.6)	5 (+0.0), 5 (+0.6)	5 (+0.0), 5 (+0.6)
2023	Mar 31 Sep 02	5 (+0.0), 5 (+0.6)	–	5 (+0.0), 5 (+0.6)	5 (+0.0), 5 (+0.6)	5 (+0.0), 5 (+0.6)
2024	Apr 05 Sep 20	5 (+0.0), 5 (+0.6)	–	5 (+0.0), 5 (+0.6)	5 (+0.0), 5 (+0.6)	5 (+0.0), 5 (+0.6)
2025	Mar 09 Oct 08	5 (+0.0), 5 (+0.6)	–	5 (+0.0), 5 (+0.6)	5 (+0.0), 5 (+0.6)	5 (+0.0), 5 (+0.6)

Oyster recruitment counts were determined by the number of live oysters of each species on the underside of tiles at a site. Tiles were deployed at multiple tidal elevations ranging from -0.3m to 0.9m MLLW (Mean Lower Low Water). Tiles were placed inside plastic mesh cages which were suspended from PVC pipe apparatuses using zip ties (Fig. 3.2**(a)** and **(b)**). Terracotta tiles ($0.15 \times 0.15\ m^2$) were primarily used, although concrete tiles (also $0.15 \times 0.15\ m^2$) were used from 2020 through 2022 at all sites (see Perog et al. (2023)). Smaller tiles ($0.075 \times 0.075\ m^2$) were used at the Glorietta Bay site, and were also affixed to a chain link fence rather than a PVC pipe apparatus due to space constraints. Oyster recruitment counts were area normalized to account for this difference, producing an estimate of per-species density [count$/m^2$] at each site and tidal elevation for each deployment. This study does not factor in potential differences in recruitment due to substrate type, which has been observed to influence settlement and recruitment (Tronske et al. 2018; Farmer et al. 2023). Tile deployment and retrieval times are shown in Table 3.1.

3.2.3 Recruitment Data Analysis

Medians and IQRs of environmental variables during the winter before, and during the oyster recruitment tile deployments were calculated. Winter values were calculated for December through February, and the recruitment period was standardized as April through September. To account for tidal aliasing, the start and end of these periods were shifted to the nearest neap tide for the water variables (salinity, temperature, water level). Each variable was used as a predictor in univariate linear regressions with recruitment density. The significance of regressions with p-values less than 0.05 was tested with a leave-one-out cross validation method.

Only values at the E Street site were used, as this was the only site with data every year from 2016 to 2025. Only *M. gigas* recruitment densities at tidal elevation +0.6m, and *O. lurida* recruitment densities at tidal elevation 0.0m were used, as these elevations had the most successful recruitment, and had no years with zero recruitment. Following Wolfe et al. (2024), recruitment densities were log transformed $(\log(x+1))$ to improve the normality of the

distributions for the regressions. Regressions were performed for the raw recruitment densities, and the log transformed recruitment densities, and the residuals were evaluated for normality by examining the quantiles of the residuals against theoretical normal distributions (Thode 2002). These showed significantly better agreement for the log transformed recruitment densities compared to the raw values, so those regressions were used for this study.

3.2.4 San Diego Bight Model Setup and Validation

Refer to Chapter 2.

3.2.5 Lagrangian Particle Tracking

3D offline Lagrangian passive particle simulations were ran using the San Diego Bight model output during the available simulation summers (2017, 2018, 2019). Particle advection was performed using OpenDrift (version 1.11.3) in Python, using a fourth order Runge-Kutta advection scheme with a timestep of 90 seconds (Dagestad et al. 2018). Horizontal diffusivity was set to $5.0 m^2\ s^{-1}$, to match that of the San Diego Bight model. Vertical mixing is determined by the simulation output salinity vertical diffusion coefficient, which is spatially and temporally varying. 6000 particles were randomly seeded throughout the bay at the start of each simulation Fig. 3.3. Simulations were initialized on the days when oyster recruitment tiles were deployed: March 27 2017, March 27 2018, and March 21 2019 at approximately neap tide. These initialization dates were chosen to have similar tidal range and spring/neap timing. Additional simulations were ran staggered from the neap tide by 3 hours (3 additional simulations per year, +3 hours, +6 hours, +9 hours) to test residence time sensitivity to initial tidal phase (Fig. 3.4). The four simulations for each year were then pooled, for a total of 24,000 particles per year (Lemagie and Lerczak 2015). Each particle simulation was run for 180 days. Particles were seeded randomly according to a uniform distribution with respect to water volume, resulting in a horizontal particle density of roughly 137 km^{-2} per simulation. All simulations were seeded with identical initial particle positions. Particles are deactivated when they reach the edge of the

model domain to prevent the return of particles into SDB that would realistically be advected away.

3.2.6 Residence Time

Residence times were calculated separately for particles in 15, $\approx$ 1.5 km long estuary bins from the mouth to the head Fig. 3.3. Two residence times were calculated for each bin: the residence time with respect to the bay mouth (i.e., from the bin to the mouth, bay-exit residence time, τ_{full}), and the residence time with respect to the bin boundaries (bin residence time, τ_{bin}). The fraction of particles inside (the bay to the bin and within each bin) at each time step was smoothed using a 50 hour filter to remove tidal oscillations. The residence time was then defined by when the smoothed curve reached its e-folding time ($\approx$ 36.8% of the initial count).

The sensitivity of the residence time with respect to the number of particles was tested through 500 permutation tests with random samples of the full 6000 particles per simulation, ranging from 100 particles, to the full 6000 used. The interquartile range of the residence times showed that as the particle count increased, the range of calculated residence times converged. 50% of residence times calculated from simulations that used 1000 particles have an error of 10% or less compared with the residence time calculated with all 6000 particles. This methodology was used rather than that used in Simons et al. (2013) since this study focuses on residence time, rather than the full spatial distribution of particles.

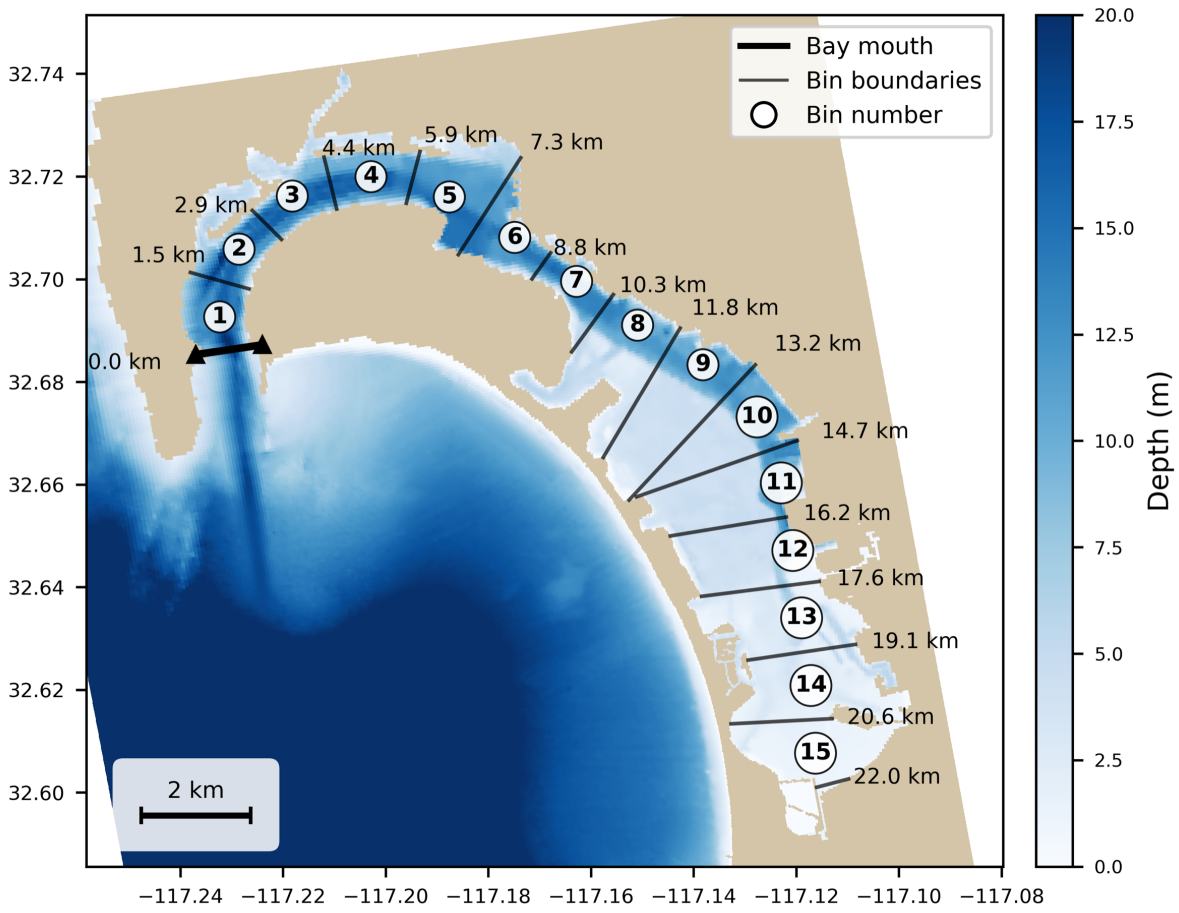


Figure 3.3. Map of a subset of the model domain showing SDB. The bay mouth is marked with a thick black line. Bin boundaries used for the residence time calculations are shown with thin black lines and bins are labeled 1 to 15 with 1 closest to the mouth.

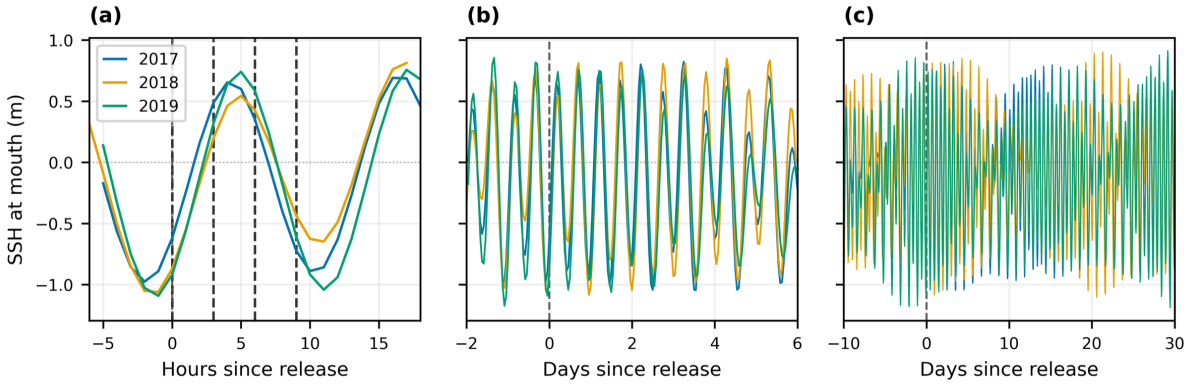


Figure 3.4. Particle release time for all three years (2017, blue; 2018, yellow; 2019, green) with respect to the tide. Panel **(a)** shows the four 3-hour staggered releases (dashed vertical lines) over a single tidal cycle, aligned for all three years. Panel **(b)** shows the first release time (dashed vertical line), aligned for all three years, over an 8 day period, highlighting the diurnal/semidiurnal tidal variability. Panel **(c)** shows the first release time, aligned for all three years, over multiple spring neap cycles (40 days).

3.2.7 Recruitment and Residence Time

With only three years of residence time available, there is not enough data to be used as a regression predictor for recruitment. However, qualitative comparisons of their spatial distributions are done here, along with a discussion of these results with reference to previous studies that examined both variables.

3.3 Results

3.3.1 Oyster Recruitment

Site comparison

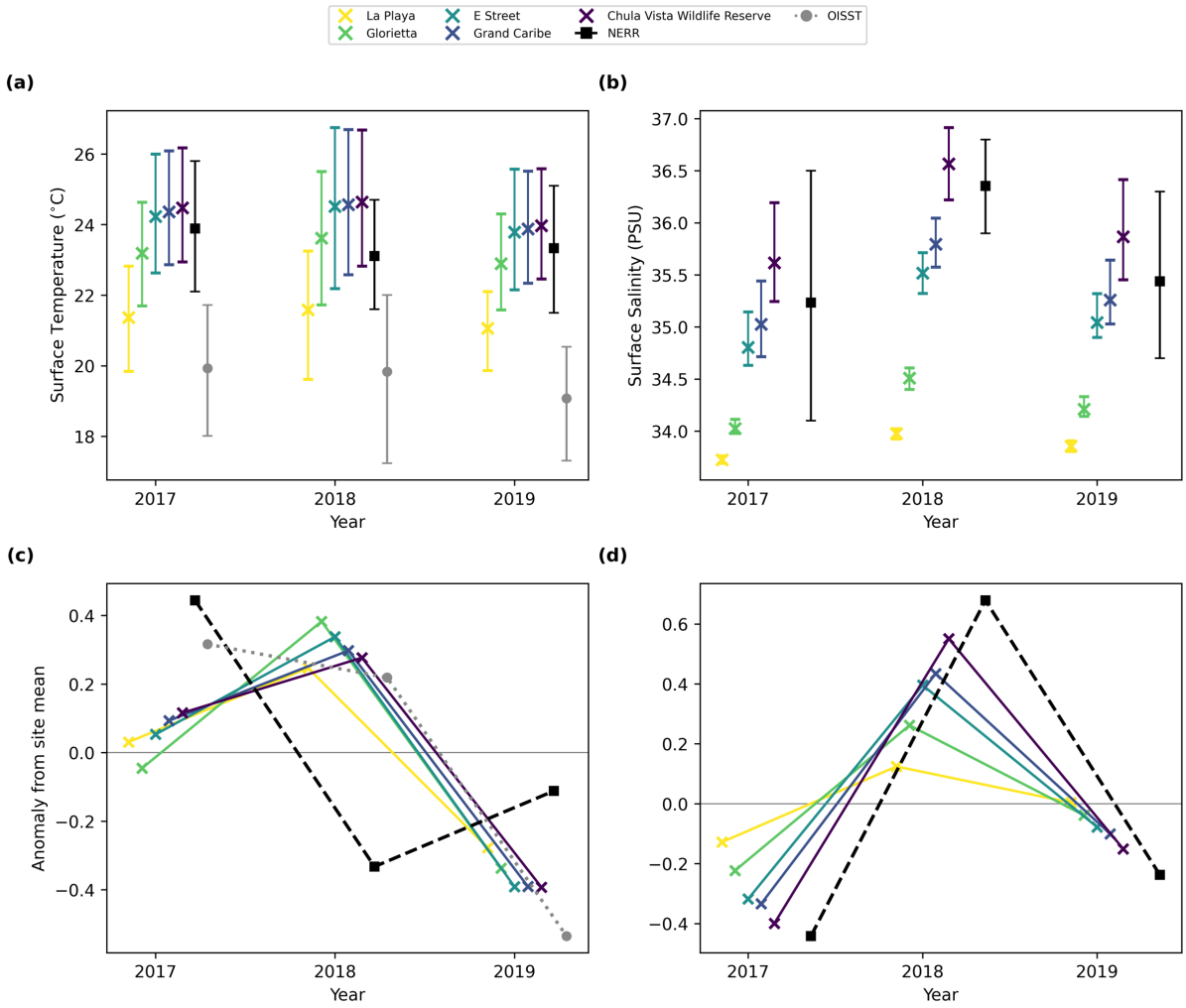


Figure 3.5. Comparison of summer (April-September) modeled surface temperature (left) and salinity (right) for years 2017 through 2019 at the five recruitment sites (La Playa, green; Glorietta, yellow; E Street, cyan; Grand Caribe, blue; Chula Vista Wildlife Reserve, pink). Panels **(a)** and **(b)** show medians and interquartile ranges for each site, alongside values from the OISST daily SST (temperature, gray triangle and dotted lines) and the south bay NERR station (temperature and salinity, black square and dashed lines). Panels **(c)** and **(d)** show the anomaly from the mean of each site. Site location is colored by distance upstream (as shown in Fig. 3.1) with yellow near the mouth and the darkest blues upstream near the head. OISST is indicated with gray as it effectively represents an offshore open ocean SST.

Inter-site variability in April-September averaged modeled surface temperature and salinity is greater than interannual variability at any of the sites (Fig. 3.5). La Playa, near SDB's mouth, is the coolest and freshest site. Salinity and temperature increase monotonically toward the head, with Chula Vista Wildlife Reserve as the warmest and saltiest site. Note that the NERR sensor shows lower temperature values as it is not a surface temperature measurement. Similarly, OISST is lower than all others as it represents values averaged over a 0.25° coastal bin that includes offshore sea surface temperatures, thus it effectively represents an offshore ocean SST. This is consistent with the overall longitudinal Bay dynamics during this time of year (Largier et al. 1996), and Chapter 2.

All model-extracted sites show the same interannual anomaly pattern (Fig. 3.5**(c)** and **(d)**). The warmest and saltiest year was 2018 (due to very minimal precipitation that year, see Chapter 2), 2017 was the coolest, and 2019 was the freshest. The NERR station salinity observations follow this same pattern, although the temperature observations do not, and show 2018 as the coolest year. OISST also does not follow this same pattern, showing 2017 slightly warmer than 2018. Despite these discrepancies of the modeled and observed temperatures, the synchrony of the modeled values provides sufficient motivation for comparing the recruitment data to the OISST and NERR time series.

Recruitment Trends

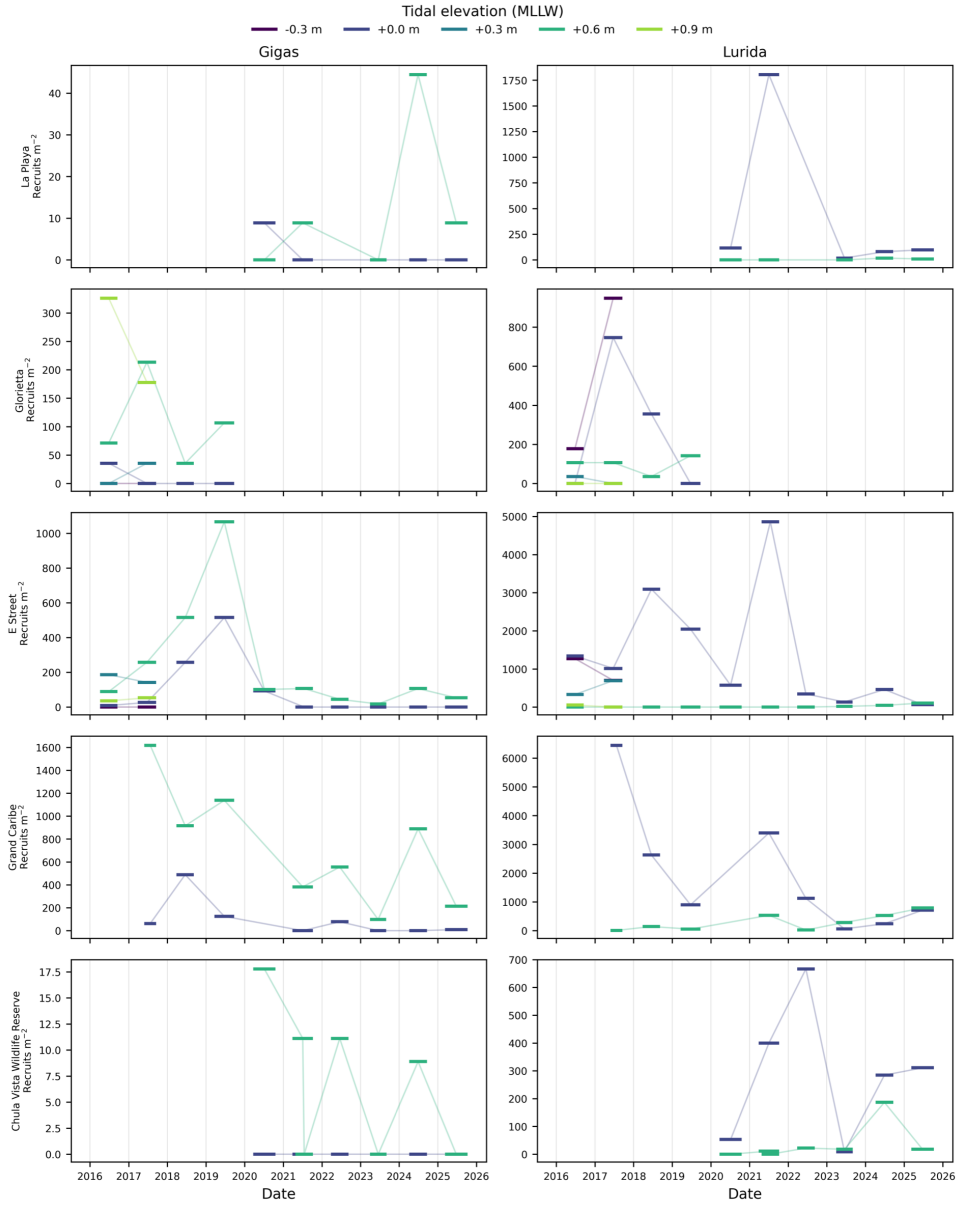


Figure 3.6. Recruitment density by site over time. Each row corresponds to a site (labeled on Fig. 3.1), ordered top to bottom from closest to SDB's mouth to furthest. The left column shows *M. gigas* recruitment, and the right column shows *O. lurida* recruitment. Data in each panel is colored by tidal elevation, with the color key at the top of the figure where deeper elevations are in darker colors. The duration of each deployment is indicated by the length of the bar at each data point, aligning with the dates on the horizontal axis of the panel. Note the independent vertical axes for each panel.

Fig. 3.1 shows the mean of all existing recruitment data for each site regardless of elevation and temporal coverage, while Fig. 3.6, shows recruitment as a function of time separated by site and deployment elevation. There is an uneven temporal coverage of measurements among sites and tidal elevations. E Street has the greatest coverage, with measurements every year 2016-2025 for tidal elevations 0.6 meters and 0.0 meters MLLW (Fig. 3.6, third row from the top). Grand Caribe is missing measurements for 2016 and 2020, but otherwise has coverage for tidal elevations 0.6 meters and -0.3 meters MLLW (Fig. 3.6, fourth row from the top). Glorietta Bay measurements ended in 2019, while La Playa and Chula Vista Wildlife Reserve measurements began in 2020.

Over all tidal elevations and time, E Street and Grand Caribe sites had much higher recruitment density than the other sites (Fig. 3.1). There are no consistent shared temporal patterns between these sites and there are significant differences in normalized recruitment values with some sites ranging from 0 to less than 100 recruits m^{-2} and some showing values well above 1000 with the maximum in the record > 6000. Within sites there is also significant variability between species and elevations. There does appear to be some longer term decline at E Street and Grand Caribe. However this is a qualitative observation.

Comparison with Environmental Conditions

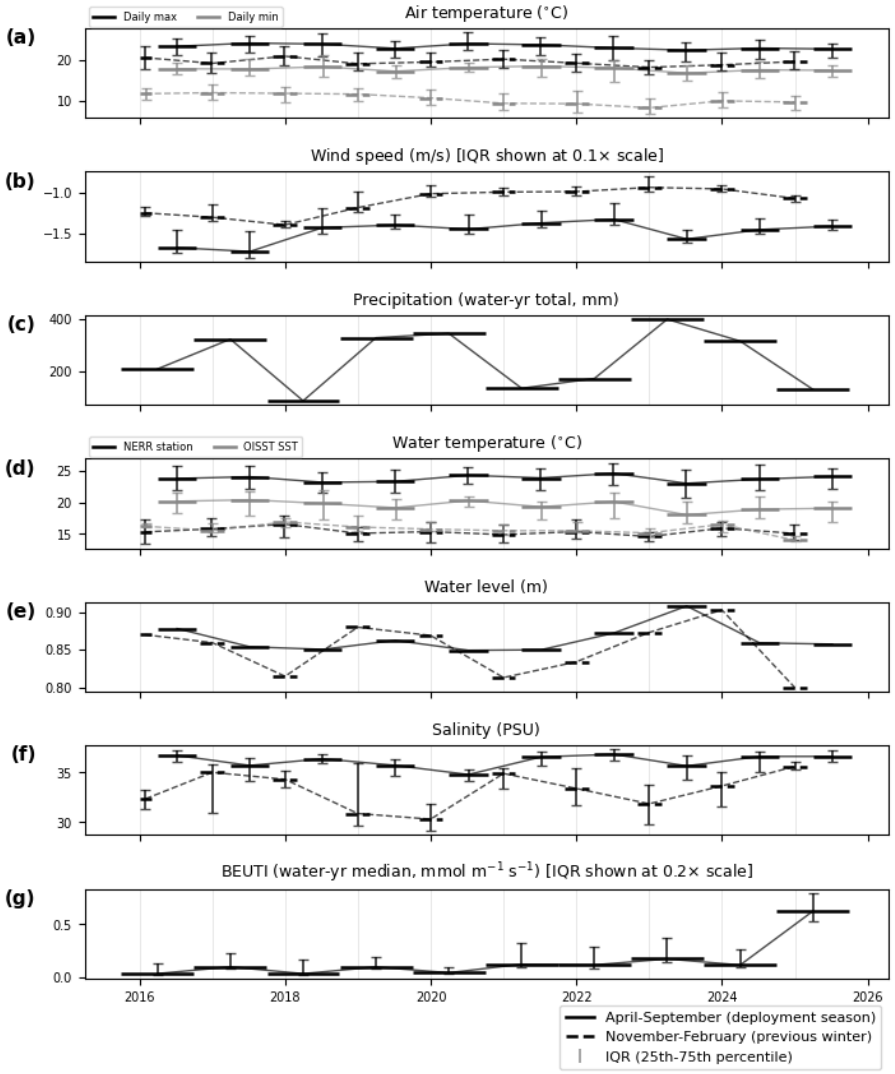


Figure 3.7. Environmental variables in and near SDB, showing seasonal median values (April - September, recruitment tile deployment season, solid black lines; November - February, previous winter season, dashed black lines) and interquartile ranges (IQRs, vertical bars). Water year total is shown for precipitation (panel **(c)**) and water year median is shown for BEUTI (panel **(g)**). IQRs are not shown for precipitation or water level.

Significant relationships were found for *M. gigas* recruitment with winter median minimum air temperature (positive) and winter median wind speed (negative). Significant relationships were found for *O. lurida* recruitment with winter median SST (positive), and water year median upwelling (negative). No significant relationships were found for either species with any

Table 3.2. Linear regressions of each median predictor against log transformed *M. gigas* and *O. lurida* recruitment densities. Values for *O. lurida* are shown in parentheses in each cell. Relationship column shows the sign of the fit. Asterisk and bold denote $p < 0.05$.

Variable	Season	Relationship with Recruitment	R^2	p
Maximum air temperature	Deployment	+ (+)	0.19 (0.40)	0.210 (0.052)
Maximum air temperature	Winter	+ (+)	0.13 (0.34)	0.312 (0.079)
Minimum air temperature	Deployment	+ (+)	0.06 (0.36)	0.499 (0.065)
Minimum air temperature	Winter	**+*** (+)	**0.66*** (0.32)	**0.004*** (0.091)
Wind Speed	Deployment	+ (+)	0.00 (0.00)	0.894 (0.979)
Wind Speed	Winter	**-*** (-)	**0.48*** (0.24)	**0.026*** (0.147)
NERR Water Level	Deployment	- (-)	0.35 (0.20)	0.071 (0.190)
NERR Water Level	Winter	+ (-)	0.00 (0.00)	0.859 (0.964)
NERR station salinity	Deployment	- (+)	0.02 (0.00)	0.664 (0.952)
NERR station salinity	Winter	- (-)	0.00 (0.00)	0.866 (0.925)
NERR station temperature	Deployment	- (-)	0.07 (0.04)	0.467 (0.575)
NERR station temperature	Winter	+ (+)	0.27 (0.12)	0.122 (0.324)
OISST SST	Deployment	+ (+)	0.10 (0.14)	0.365 (0.282)
OISST SST	Winter	+ (**+***)	0.31 (**0.48***)	0.092 (**0.025***)
Precipitation	Water-yr	- (-)	0.01 (0.06)	0.787 (0.497)
BEUTI upwelling	Water-yr	- (**-***)	0.12 (**0.49***)	0.319 (**0.025***)

Table 3.3. Linear regressions of each IQR predictor against log transformed *M. gigas* and *O. lurida* recruitment densities. Values for *O. lurida* are shown in parentheses in each cell. Relationship column shows the sign of the fit. Asterisk and bold denote $p < 0.05$.

Variable	Season	Relationship with Recruitment	R^2	p
Maximum air temperature	Deployment	- (+)	0.01 (0.04)	0.778 (0.599)
Maximum air temperature	Winter	+ (+)	0.18 (0.23)	0.216 (0.159)
Minimum air temperature	Deployment	+ (+)	0.01 (0.06)	0.811 (0.483)
Minimum air temperature	Winter	- (-)	0.07 (0.00)	0.464 (0.936)
Wind Speed	Deployment	+ (+)	0.13 (0.30)	0.308 (0.104)
Wind Speed	Winter	+ (+)	0.12 (0.01)	0.320 (0.819)
NERR Water Level	Deployment	+ (+)	0.18 (0.06)	0.229 (0.512)
NERR Water Level	Winter	+ (+)	0.12 (0.33)	0.329 (0.083)
NERR station salinity	Deployment	- (-)	0.02 (0.03)	0.719 (0.647)
NERR station salinity	Winter	+ (+)	0.13 (0.02)	0.307 (0.710)
NERR station temperature	Deployment	- (-)	0.08 (0.02)	0.430 (0.697)
NERR station temperature	Winter	+ (+)	0.06 (0.20)	0.506 (0.191)
OISST SST	Deployment	+ (+)	0.05 (0.01)	0.525 (0.785)
OISST SST	Winter	+ (+)	0.32 (0.09)	0.089 (0.395)
Precipitation	Water-yr	- (-)	0.26 (0.17)	0.128 (0.237)
BEUTI upwelling	Water-yr	- (-)	0.28 (0.21)	0.113 (0.186)

IQR predictors.

3.3.2 Residence Times

Residence curves for bins near the mouth drop off steeply, while curves for bins near the head drop off slowly (Fig. 3.8). Residence times τ_{full} increase monotonically toward the head for all three years with a steeper slope and thus longer residence times beyond $\approx$ 10 km from the mouth (Fig. 3.9**(a)**). Residence times in 2018 are consistently longer, significantly diverging from the other two years upstream of $\approx$ 10 km from the mouth. τ_{full} at the mouth is no more than 10 days, while it ranges from $\approx$ 60 to $\approx$ 180 days near the head. The tidal phase of particle release (shading on Fig. 3.9) had minimal impact on residence times near the mouth. However the range of both τ_{full} and τ_{bin} increase toward head. The 180 day particle tracking simulation was not long enough to reach the τ_{full} time for some tidal phases in bins 11-15.

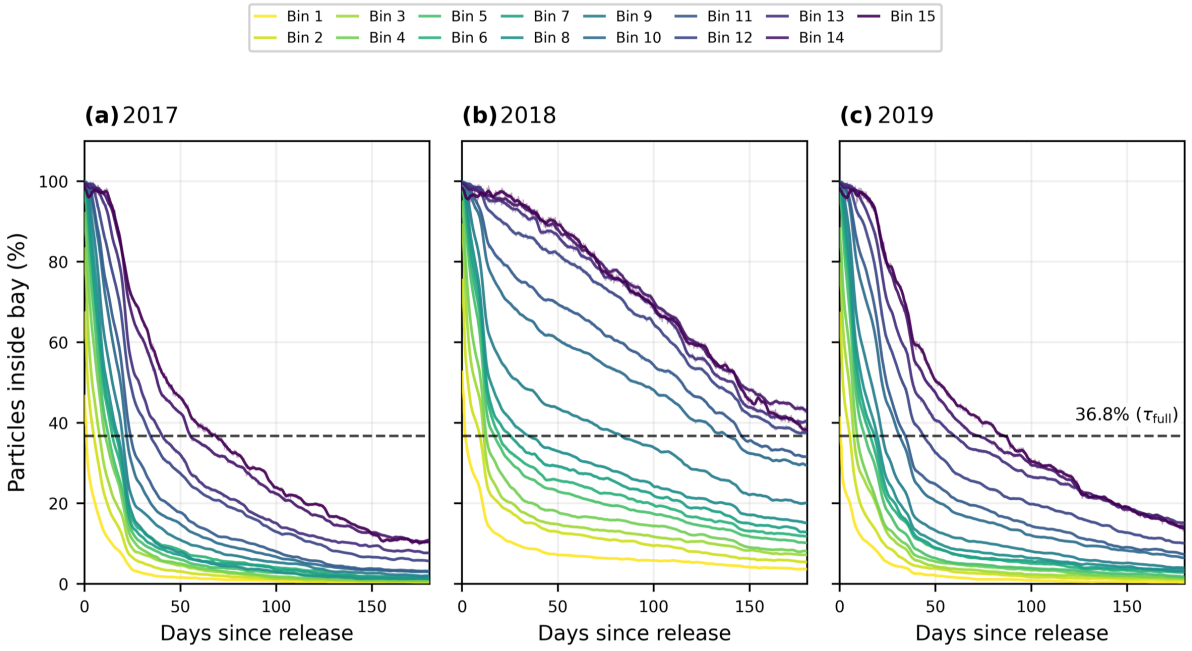


Figure 3.8. Residence curves showing the percent of particles from each bin (as labeled in Fig. 3.3, with bin 1 closest to the mouth, and bin 15 at the head) still remaining inside the bay, for simulation years **(a)** 2017, **(b)** 2018, and **(c)** 2019. The dashed horizontal line indicated τ_{full}, when the percent of particles still in the bay reaches 36.8% of its original value.

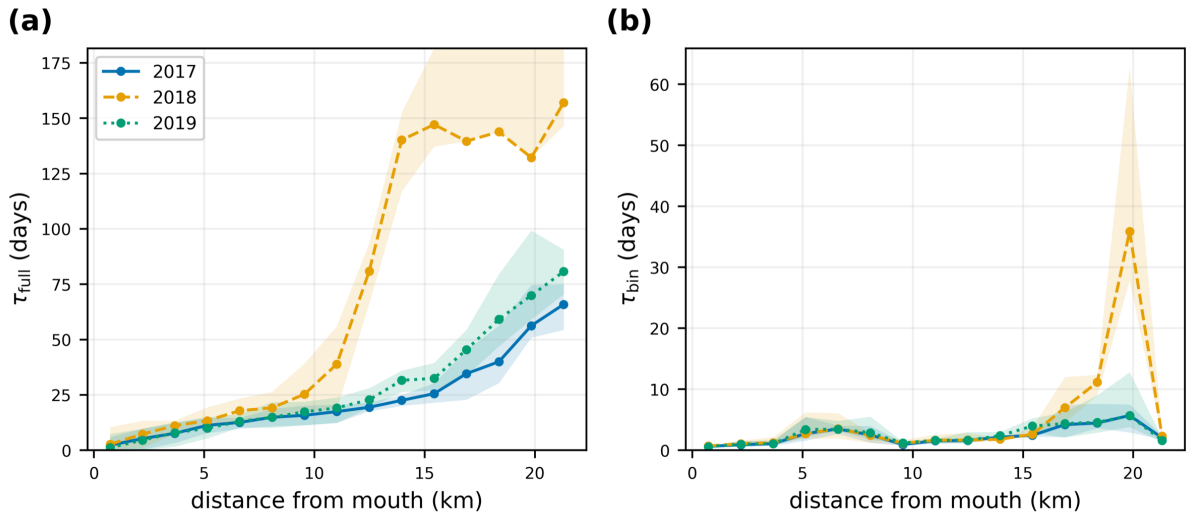


Figure 3.9. Residence times **(a)** τ_{full} and **(b)** τ_{bin} for years 2017 (solid blue), 2018 (dashed yellow), and 2019 (dotted green) as a function of along-channel distance from SDB's mouth. Shaded regions indicate the upper and lower residence time values from the four independent 3-hour staggered particle simulations each year.

3.4 Discussion

3.4.1 Recruitment Temporal Variability

Of the significant regressions found, *M. gigas* recruitment was related to the medians of two atmospheric variables during the previous winters to tile deployment (positive relationship with minimum air temperature and negative relationship with wind speed), while *O. lurida* recruitment was related to the medians of two water variables (positive relationship with winter SST and negative relationship with water-year upwelling). Given the previously found preference of *M. gigas* for higher tidal elevations, and the preference of *O. lurida* for lower tidal elevations (Perog et al. 2022), these relationships make sense: *M. gigas* had more aerial exposure and responded to atmospheric conditions, and *O. lurida* spent more time underwater and responded more to water conditions.

However, most univariate regressions performed here were not significant. Two relationships that were particularly expected but not seen were with precipitation and with salinity (Chang et al. 2016). This could be in part due to the small sample size, and due to environmental

measurements not having been collected at the recruitment sites. Given this weak correspondence between environmental variables and oyster recruitment found in this study, there is strong motivation for co-located sensors with recruitment tiles during deployments (Cheng et al. 2015). This is supported by multiple previous recruitment and settlement studies that found significant relationships with measurements from co-located sensors (Lagarde et al. 2017; Farmer et al. 2023; Dutertre et al. 2010; O'Beirn et al. 1995). However, other studies with co-located sensors did not (Seale and Zacherl 2009; Valdez and Ruesink 2017). These studies also used different statistics and data integration periods than in this study, and these may also change the significant relationships found. Higher temporal resolution of settlement and recruitment would possibly show clearer relationships, as in Chang et al. (2016).

The longer decadal decline in recruitment qualitatively observed at E Street and Grand Caribe is not neatly explained by any of the environmental variables examined in this study. This could be a transient trend, which more years of data would clarify. It should also be noted that this trend reversed the trend reported in (Wolfe et al. 2024) from oyster density measurements 2013, 2017, and 2020 at Grand Caribe, Glorietta Bay, and Chula Vista Wildlife Reserve, which those authors associate with increased SST.

3.4.2 Recruitment Spatial Variability

Generally, recruitment density increases further into SDB from the mouth, verifying the pattern found in Deck (2010). This is expected, as there is increased larval retention near the bay head where the residence time is higher (Deck 2010). Comparing the three years when residence time has been calculated, *M. gigas* recruitment density at E Street increases over all three years, while *O. lurida* density peaks in 2018. However, recruitment values for both species at Grand Caribe do not share the same pattern, and instead show decreased recruitment in 2018. There are no studies that the author is aware of that compare interannual variability of residence time with oyster recruitment. This would be an important step for long term estuarine oyster habitat management.

3.4.3 Residence Time Interannual Variability

The elevated residence times found in 2018 indicate significant differences in SDB forcing and resulting hydrodynamics. This year was the driest year in the 2016 through 2025 record Fig. 3.7, leading to reduced connectivity between the head and the mouth (as seen in Chapter 2), hypersalinity near the head (Fig. 3.5) and increased back bay residence times.

3.5 Conclusion

This study compared recruitment patterns of the native *O. lurida* and invasive *M. gigas* across a decade of settlement tile deployments at five sites in San Diego Bay, using environmental time series, hydrodynamic model output, and Lagrangian particle tracking. Recruitment density increased toward the bay head for both species, consistent with the longitudinal increase in bay-exit residence time from tidal timescales near the mouth to 60–180 days near the head. E Street and Grand Caribe supported recruitment densities more than an order of magnitude greater than sites nearer the mouth, indicating the back bay is important habitat for both species. Relationships between recruitment and environmental conditions were limited and distinct for each species, and involved winter conditions preceding deployment rather than conditions during deployment itself. *M. gigas*, which recruited most successfully at +0.6 m MLLW, was related to atmospheric variables (winter minimum air temperature and wind speed), while *O. lurida*, which recruited most successfully at 0.0 m MLLW, was related to water variables (winter sea surface temperature and water-year upwelling), consistent with differing aerial exposure. However, expected relationships with salinity and precipitation were not found, and no interquartile range predictor was significant for either species. Interannual variability in residence time also did not explain interannual variability in recruitment. Residence times in 2018 were substantially longer than in 2017 or 2019, reflecting that year's minimal precipitation and reduced connectivity between the mouth and head. Yet recruitment in 2018 was elevated for *O. lurida* at E Street but reduced for both species at Grand Caribe, showing no clear temporal correspondence between

long residence time and high recruitment.

These results are limited by the ten years of annual regression data, which gives low statistical power and makes it difficult to separate correlated predictors; by the three simulated years available for the residence time comparison; by environmental observations drawn from stations several kilometers from the recruitment sites in a bay with strong longitudinal gradients; and by the exclusion of substrate type and predation, both known to influence recruitment elsewhere. Co-located sensors deployed alongside future tile deployments would test whether the weak environmental correspondence found here reflects genuinely weak responses or spatial decorrelation of the tested variables, and extending the hydrodynamic simulations across the full recruitment record would allow residence time to be used as a quantitative predictor rather than a qualitative comparison. Resolving these questions matters for management of low-inflow estuaries generally, where the same physical processes that influence oyster recruitment near the head also control transport and retention of heat, salt, and contaminants.

3.6 Authors' Contributions

Niv Anidjar: conceptualization, data curation, formal analysis, investigation, methodology, validation, visualization, writing (original draft)

Sarah N. Giddings: conceptualization, formal analysis, funding acquisition, investigation, methodology, project administration, resources, supervision, validation, writing (review & editing)

Danielle C. Zacherl: conceptualization, data curation, funding acquisition, investigation, methodology, project administration, resources, supervision, validation, writing (review & editing)

Chelsea M. Bowers-Doerning: data curation, investigation, project administration, validation, writing (review & editing)

3.7 Acknowledgements

Chapter 3, in full, is currently being prepared for submission for publication of the material. Anidjar, Niv; Giddings, Sarah N; Zacherl, Danielle C.; Bowers-Doerning, Chelsea M. The dissertation author was the primary investigator and author of this material.

Chapter 4

Conclusion

Low-inflow estuaries (LIEs) are globally distributed systems in which freshwater input is small enough during at least part of the year such that heating, evaporation, tidal mixing or waves can dominate the buoyancy forcing (Largier et al. 1997; Largier 2023). How water circulates through them, how long it stays, and what biological communities that circulation supports, directly impacts coastal communities and ecosystems. These properties can influence contaminant retention, eutrophication, water quality, mouth closures, habitat restoration, and the response of these systems to a changing climate. Because LIE density gradients can be jointly driven by salinity and temperature, they are poorly described by the classical theories that dominate estuarine research (Geyer and MacCready 2014). This dissertation examined the hydrodynamics, oyster ecology and biophysical interactions of two Southern California LIEs.

Conditions in LIEs shift rapidly across tidal, diurnal, and seasonal timescales, and the organisms living in them must track those shifts continuously. In Chapter 1, oyster valve gape was measured continuously alongside physical and chemical conditions in the regularly stratified, mostly classical, Los Peñasquitos Lagoon (LPL) to determine how *Magallana gigas* responds to this environment. Near-surface oysters responded most strongly to salinity and dissolved oxygen, opened and closed in phase with insolation, and closed consistently during higher low tides. Near-bottom oysters responded weakly to all measured variables, had a lagged response to insolation, and showed little coherent response to tidal phase. These differing responses dependent on water

column vertical position are consistent with stratification producing more variable near-surface conditions. Of the multivariate models tested, the nonlinear S-Map model performed best, and identified simultaneous dissolved oxygen and salinity as the dominant predictors, indicating state dependence in the system dynamics that linear analyses did not represent. These results support the use of oysters in biological early warning systems (BEWS), but also show that such systems require local calibration and nonlinear treatment. Covariance among the water quality variables during storm conditions limited attribution to any single driver, and future deployments should therefore include a larger number of oysters, colocated chlorophyll, pH, and turbidity sensors, and moorings at multiple locations within and across estuaries. Most importantly, continuous observations spanning an inlet closure from before onset through reopening would establish the timescales on which biological damage occurs, which would provide critical information for estuary managers to decide when intervention is warranted.

The time varying tidally averaged circulation of San Diego Bay (SDB) had not previously been described, despite well documented longitudinal gradients and tidal exchange. In Chapter 2, three years of output from a high resolution numerical model were analyzed using the Total Exchange Flow (TEF) framework in salinity, temperature, and density coordinates. A seasonally shifting two cell structure was found: during summer, a thermally driven classical cell near the mouth and a salinity driven inverse cell near the head, with the boundary between them set by the local balance of temperature and salinity contributions to the density gradient. Fall and winter cooling acting on hypersaline water accumulating near the head through the preceding summer produced inverse circulation throughout the bay, consistent with the observations of Chadwick et al. (1996). Entire-bay classical circulation occurred only during winter precipitation events, persisting in the wetter years (2017 and 2019) and appearing only transiently in the driest year (2018). Circulation strength scaled with tidal inflow rate and was largely independent of circulation state, consistent with tidal pumping as the dominant forcing mechanism. However a clear transition to decreased exchange flow is coincident with the location in the bay where gradients invert. That the seasonal state depends on salt accumulated months earlier indicates

that the storage term in the salt budget is of leading order importance, and that these systems are never in steady balance with instantaneous surface forcing. Applying TEF to this seasonally inverse system also revealed that the conventional order of operations for time-integrating bulk transports can introduce cancellation errors where transport-weighted properties vary rapidly in time, an issue that warrants further investigation. Future work should involve decomposing the exchange flow by mechanism (MacCready and Geyer 2024), and simulating additional years to verify the relationship between interannual differences of circulation and precipitation.

Chapter 3 brought the physical and biological components together, comparing a decade of settlement tile deployments at five sites in SDB with local environmental time series and with residence times estimated from offline Lagrangian particle tracking through the same model used in Chapter 2. Recruitment density of both the native *Ostrea lurida* and the invasive *M. gigas* generally increased from the mouth toward the head, indicating that the back bay in important habitat for both species. This spatial pattern is consistent with bay-exit residence times increasing towards the head (from less than 10 days near the mouth to 60-140 days near the head) and temperature increasing towards the head, both expected to favor recruitment. The environmental relationships that emerged were species specific and consistent with tidal elevation. *M. gigas*, had greater recruitment higher in the intertidal zone, and responded to atmospheric conditions during the winter preceding deployment. *O. lurida*, recruited better at lower elevations, responded clearly to water conditions during the preceding winter. Both sets of relationships involved conditions preceding deployment rather than during it, possibly reflecting the importance of larval development to recruitment. Expected relationships with salinity and precipitation were not found, and residence times, although substantially longer in 2018 than in adjacent years, did not explain interannual variability in recruitment. These results are limited by ten years of annual values, by three simulated years for the residence time comparison, by environmental observations drawn from stations several kilometers from the recruitment sites, and by the exclusion of substrate and predation. Colocated sensors deployed alongside future tile deployments would test whether the weak correspondence found here reflects genuinely weak

responses or spatial decorrelation, and extending the hydrodynamic simulations across the full recruitment record would allow residence time to be used as a quantitative predictor rather than a qualitative, largely spatial, comparison. Resolving these questions matters for management of LIEs generally, where the same processes that influence oyster recruitment near the head also control the transport and retention of heat, salt, and contaminants.

Estuaries are sites of indistinct boundaries. Ultimately, in my view, the fate of Southern California LIEs is determined by where we (those who participate in their stewardship) set their boundaries. What do we include in our models and decision making processes, and what do we exclude? Who benefits from particular boundaries, and who is marginalized and made invisible (Arriola 2020)? What futures are made possible by our choice of boundaries (Goodyear-Ka'ōpua 2018; Chevalier 2026)? Estuaries are sites of indistinct boundaries. Where are we?

Bibliography

(1960). Sikes Act.

Andersen, T., Carstensen, J., Hernández-García, E., and Duarte, C. M. (2009). Ecological thresholds and regime shifts: Approaches to identification. *Trends in Ecology & Evolution*, 24(1):49–57.

Andrewartha, SJ., Elliot, NG., McCulloch, JW., and Frappell, PB. (2015). Aquaculture Sentinels: Smart-farming with Biosensor Equipped Stock. *Journal of Aquaculture Research & Development*, 07(01).

Arriola, T. H. (2020). *Securing Nature: Militarism, Indigeneity and the Environment in the Northern Mariana Islands*. PhD thesis.

Arroyo, C. L., Dionela, M., Ann Bautista, M. G., Concepcion, R., Vicerra, R. R., and Duarte, B. (2022). Biomonitoring Technologies Used in Aquatic Ecosystems: A Systematic and Trend Analysis. In *2022 IEEE 14th International Conference on Humanoid, Nanotechnology, Information Technology, Communication and Control, Environment, and Management (HNICEM)*, pages 1–5.

Bae, M.-J. and Park, Y.-S. (2014). Biological early warning system based on the responses of aquatic organisms to disturbances: A review. *Science of The Total Environment*, 466–467:635–649.

Barillé, L., Haure, J., Cognie, B., and Leroy, A. (2000). Variations in pallial organs and eulaterofrontal cirri in response to high particulate matter concentrations in the oyster Crassostrea gigas. *Canadian Journal of Fisheries and Aquatic Sciences*, 57(4):837–843.

Beck, M. W., Brumbaugh, R. D., Airoldi, L., Carranza, A., Coen, L. D., Crawford, C., Defeo, O., Edgar, G. J., Hancock, B., Kay, M. C., Lenihan, H. S., Luckenbach, M. W., Toropova, C. L., Zhang, G., and Guo, X. (2011). Oyster Reefs at Risk and Recommendations for Conservation, Restoration, and Management. *BioScience*, 61(2):107–116.

Behrens, D. K., Bombardelli, F. A., Largier, J. L., and Twohy, E. (2013). Episodic closure of the tidal inlet at the mouth of the Russian River — A small bar-built estuary in California.

Geomorphology, 189:66–80.

Beller, E., Baumgarten, S., Grossinger, R., Longcore, T., Stein, E., Dark, S., and Dusterhoff, S. (2014). Northern San Diego County Lagoons Historical Ecology Investigation: Regional Patterns, Local Diversity, and Landscape Trajectories. Technical Report 722, San Fransisco Estuary Institute.

Booij, N., Ris, R. C., and Holthuijsen, L. H. (1999). A third-generation wave model for coastal regions: 1. Model description and validation. *Journal of Geophysical Research: Oceans*, 104(C4):7649–7666.

Borcherding, J. (2006). Ten Years of Practical Experience with the Dreissena-Monitor, a Biological Early Warning System for Continuous Water Quality Monitoring. *Hydrobiologia*, 556(1):417–426.

Brasseale, E., Feddersen, F., Wu, X., Zimmer-Faust, A. G., and Giddings, S. N. (2023). Performance of a One-Dimensional Model of Wave-Driven Nearshore Alongshore Tracer Transport and Decay with Applications for Dry Weather Coastal Pollution. *Environmental Science & Technology*, 57(39):14674–14683.

Bremer, S. and Meisch, S. (2017). Co-production in climate change research: Reviewing different perspectives. *WIREs Climate Change*, 8(6):e482.

Browning, B. M., Speth, J. W., and Gayman, W. (1973). THE NATURAL RESOURCES OF SAN DIEGO BAY THEIR STATUS AND FUTURE.

Bub, S., Petschick, L. L., Stehle, S., Wolfram, J., and Schulz, R. (2025). Limitations of chemical monitoring hinder aquatic risk evaluations on the macroscale. *Science*, 388(6753):1301–1305.

California Coastal Commission (1998). Tu 15f Staff Recommendation On Consistency Determination CD-9-98. Technical report.

California Regional Water Control Board, San Diego Region (2012). Cleanup and Abatement Order No. R9-2012-0024.

Carson, H. S. (2010). Population connectivity of the Olympia oyster in southern California. *Limnology and Oceanography*, 55(1):134–148.

Casas, S. M., Filgueira, R., Lavaud, R., Comeau, L. A., La Peyre, M. K., and La Peyre, J. F. (2018). Combined effects of temperature and salinity on the physiology of two geographically-distant eastern oyster populations. *Journal of Experimental Marine Biology and Ecology*, 506:82–90.

Chadwick, D. B. and Largier, J. L. (1999a). The influence of tidal range on the exchange between

San Diego Bay and the ocean. *Journal of Geophysical Research: Oceans*, 104(C12):29885–29899.

Chadwick, D. B. and Largier, J. L. (1999b). Tidal exchange at the bay-ocean boundary. *Journal of Geophysical Research: Oceans*, 104(C12):29901–29924.

Chadwick, D. B., Largier, J. L., and Cheng, R. T. (1996). The Role of Thermal Stratification in Tidal Exchange at the Mouth of San Diego Bay. In *Buoyancy Effects on Coastal and Estuarine Dynamics*, chapter 12, pages 155–174. American Geophysical Union (AGU).

Chadwick, D. B., Zirino, A., Rivera-Duarte, I., Katz, C. N., and Blake, A. C. (2004). Modeling the mass balance and fate of copper in San Diego Bay. *Limnology and Oceanography*, 49(2):355–366.

Chang, A. L., Deck, A. K., Sullivan, L. J., Morgan, S. G., and Ferner, M. C. (2016). Upstream—Downstream Shifts in Peak Recruitment of the Native Olympia Oyster in San Francisco Bay During Wet and Dry Years. *Estuaries and Coasts*, 41(1):65–78.

Chen, S.-N., Geyer, W. R., Ralston, D. K., and Lerczak, J. A. (2012). Estuarine Exchange Flow Quantified with Isohaline Coordinates: Contrasting Long and Short Estuaries.

Cheng, B. S., Bible, J. M., Chang, A. L., Ferner, M. C., Wasson, K., Zabin, C. J., Latta, M., Deck, A., Todgham, A. E., and Grosholz, E. D. (2015). Testing local and global stressor impacts on a coastal foundation species using an ecologically realistic framework. *Global Change Biology*, 21(7):2488–2499.

Cheng, C. and Nagoda, C. (2015). Strategy for a Healthy San Diego Bay. Technical report.

Chevalier, C. (2026). The Ocean Is Not a Machine: A Feminist Media Analysis of Oceanographic Models, Simulations, and Futures. *World Futures Review*, page 19467567261443105.

Chu, P. and Armstrong, A. (2005). Instantaneous current prediction for naval operations. In *Proceedings of OCEANS 2005 MTS/IEEE*, pages 884–890 Vol. 1.

Chu, P. C. and Kyriakidis, K. (2011). Chemical Spill Characteristics in the San Diego Bay. *Marine Technology Society Journal*, 45(2):52–58.

Chu, P. C., Kyriakidis, K., Haeger, S. D., and Ward, M. (2006). TWO CHEMICAL SPILL PATTERNS IN TIDALLY DOMINATED SAN DIEGO BAY.

Cloern, J. E. and Jassby, A. D. (2012). Drivers of change in estuarine-coastal ecosystems: Discoveries from four decades of study in San Francisco Bay. *Reviews of Geophysics*, 50(4).

Codiga, D. L. (2011). Unified Tidal Analysis and Prediction Using the UTide Matlab Functions.

Technical report, Graduate School of Oceanography, University of Rhode Island, Narragansett, RI.

Costanza, R., d'Arge, R., de Groot, R., Farber, S., Grasso, M., Hannon, B., Limburg, K., Naeem, S., O'Neill, R. V., Paruelo, J., Raskin, R. G., Sutton, P., and van den Belt, M. (1997). The value of the world's ecosystem services and natural capital. *Nature*, 387(6630):253–260.

Costanza, R., de Groot, R., Sutton, P., van der Ploeg, S., Anderson, S. J., Kubiszewski, I., Farber, S., and Turner, R. K. (2014). Changes in the global value of ecosystem services. *Global Environmental Change*, 26:152–158.

Cotter, P. J. and Cunniff, S. E. (1987). Environmental Impact Statement for San Diego (LA-5) Ocean Dredged Material Disposal Site. Technical report.

Cousins, M., Stacey, M. T., and Drake, J. L. (2010). Effects of seasonal stratification on turbulent mixing in a hypereutrophic coastal lagoon. *Limnology and Oceanography*, 55(1):172–186.

Crooks, J., Crooks, K. R., and Crooks, A. J. (2015). Observations of the non-native Pacific oyster (*Crassostrea gigas*) in San Diego County, California. *California Fish and Game*, 101(2).

Crooks, J., McCullough, J., Almeida, M., and Uyeda, K. (2019). The Physical, Chemical and Biological Monitoring of Los Penasquitos Lagoon. Technical report, Southwest Wetlands Interpretative Association and the Tijuana River National Estuarine Research Reserve.

Dagestad, K.-F., Röhrs, J., Breivik, Ø., and Ådlandsvik, B. (2018). OpenDrift v1.0: A generic framework for trajectory modelling. *Geoscientific Model Development*, 11(4):1405–1420.

Dame, R. F. and Olenin, S., editors (2005). *The Comparative Roles of Suspension-Feeders in Ecosystems*, volume 47 of *NATO Science Series IV: Earth and Environmental Series*. Springer-Verlag, Berlin/Heidelberg.

de Groot, R., Brander, L., van der Ploeg, S., Costanza, R., Bernard, F., Braat, L., Christie, M., Crossman, N., Ghermandi, A., Hein, L., Hussain, S., Kumar, P., McVittie, A., Portela, R., Rodriguez, L. C., ten Brink, P., and van Beukering, P. (2012). Global estimates of the value of ecosystems and their services in monetary units. *Ecosystem Services*, 1(1):50–61.

de Zwart, D., Kramer, K. J. M., and Jenner, H. A. (1995). Practical experiences with the biological early warning system "mosselmonitor". *Environmental Toxicology and Water Quality*, 10(4):237–247.

Deck, A. K. (2010). *Effects of Interspecific Competition and Coastal Oceanography on Population Dynamics of the Olympia Oyster, Ostrea Lurida, along Estuarine Gradients*. M.S., University of California, Davis, United States – California.

Deheyn, D. D. and Latz, M. I. (2006). Bioavailability of metals along a contamination gradient in San Diego Bay (California, USA). *Chemosphere*, 63(5):818–834.

Delaney, L. (1965). Removal of Waste Discharges from San Diego Bay. Technical report.

Delgadillo-Hinojosa, F., Zirino, A., Holm-Hansen, O., Hernández-Ayón, J. M., Boyd, T. J., Chadwick, B., and Rivera-Duarte, I. (2008). Dissolved nutrient balance and net ecosystem metabolism in a Mediterranean-climate coastal lagoon: San Diego Bay. *Estuarine, Coastal and Shelf Science*, 76(3):594–607.

Dern, G. H. (1934). San Diego Harbor, Calif. - Letter from the secretary of war.

Deyle, E. R. and Sugihara, G. (2011). Generalized Theorems for Nonlinear State Space Reconstruction. *PLOS ONE*, 6(3):e18295.

Dutertre, M., Barillé, L., Beninger, P. G., Rosa, P., and Gruet, Y. (2009). Variations in the pallial organ sizes of the invasive oyster, *Crassostrea gigas*, along an extreme turbidity gradient. *Estuarine, Coastal and Shelf Science*, 85(3):431–436.

Dutertre, M., Beninger, P. G., Barillé, L., Papin, M., and Haure, J. (2010). Rising water temperatures, reproduction and recruitment of an invasive oyster, Crassostrea gigas, on the French Atlantic coast. *Marine Environmental Research*, 69(1):1–9.

Elwany, M. H. S. (2011). Characteristics, Restoration, and Enhancement of Southern California Lagoons. *Journal of Coastal Research*, 2011(10059):246–255.

EPA (1991). Ocean Dumping; Designation of Site. Technical Report FRL 3896-5.

ESA Associates and Merkel & Associates (2022). San Diego Bay Eelgrass Blue Carbon Study. Technical report.

Fairall, C. W., Bradley, E. F., Hare, J. E., Grachev, A. A., and Edson, J. B. (2003). Bulk Parameterization of Air–Sea Fluxes: Updates and Verification for the COARE Algorithm.

Farmer, M. A., Klick, S. A., Cullen, D. W., and Stevens, B. G. (2023). Eastern oysters *Crassostrea virginica* settle near inlets in a lagoonal estuary: Spatial and temporal distribution of recruitment in Mid-Atlantic Coastal Bays (Maryland, USA). *PeerJ*, 11:e15114.

Feddersen, F., Boehm, A. B., Giddings, S. N., Wu, X., and Liden, D. (2021). Modeling Untreated Wastewater Evolution and Swimmer Illness for Four Wastewater Infrastructure Scenarios in the San Diego-Tijuana (US/MX) Border Region. *GeoHealth*, 5(11):e2021GH000490.

Felt, U., Fouché, R., Miller, C. A., and Smith-Doerr, L., editors (2017). *The Handbook of Science and Technology Studies*. MIT press, Cambridge, 4th ed edition.

Fong, P. and Kennison, R. L. (2010). Chapter 10: Phase Shifts, Alternative Stable States, and the Status of Southern California Lagoons. In Kennish, M. J. and Paerl, H. W., editors, *Coastal Lagoons: Critical Habitats of Environmental Change*. CRC Press.

Fournier, E., Tran, D., Denison, F., Massabuau, J.-C., and Garnier-Laplace, J. (2004). Valve closure response to uranium exposure for a freshwater bivalve (*Corbicula fluminea*): Quantification of the influence of pH. *Environmental Toxicology and Chemistry*, 23(5):1108–1114.

Fuentes, C. M., Whitcraft, C. R., and Zacherl, D. C. (2020). Adaptive Restoration Reveals Potential Effect of Tidal Elevation on Oyster Restoration Outcomes. *Wetlands*, 40(1):93–99.

Gaines, S. D. and Bertness, M. D. (1992). Dispersal of juveniles and variable recruitment in sessile marine species. *Nature*, 360(6404):579–580.

Gale, E., Pattiaratchi, C., and Ranasinghe, R. (2007). Processes driving circulation, exchange and flushing within intermittently closing and opening lakes and lagoons. *Marine and Freshwater Research*, 58(8):709–719.

Garrison, L. M. (1916). San Dieg Harbor, Cal. - Letter from the Secretary of War.

Getz, E. and Eckert, C. (2023). Effects of Salinity on Species Richness and Community Composition in a Hypersaline Estuary. *Estuaries and Coasts*, 46(8):2175–2189.

Geyer, W. R. and MacCready, P. (2014). The Estuarine Circulation. *Annual Review of Fluid Mechanics*, 46(1):175–197.

Giddings, S. N., Monismith, S. G., Fong, D. A., and Stacey, M. T. (2014). Using Depth-Normalized Coordinates to Examine Mass Transport Residual Circulation in Estuaries with Large Tidal Amplitude Relative to the Mean Depth.

Godin, G., Candela, J., and de la Paz-Vela, R. (1981). On the feasibility of detecting net transports in and out of Georgia strait with an array of current meters. *Atmosphere-Ocean*, 19(2):148–157.

Gomez, A. R. (2024). (Re)riteing the Land: Sogorea Te' Land Trust, Amah Mutsun Land Trust, and Indigenous Resurgence in California. *American Indian Culture and Research Journal*, 47(2).

Goodyear-Ka'ōpua, N. (2018). Indigenous Oceanic Futures - Challenging Settler Colonialisms and Militarization. In *Indigenous and Decolonizing Studies in Education*. Routledge, 1st edition.

Gosling, E. (2015). Reproduction, settlement and recruitment. In *Marine Bivalve Molluscs*, chapter 5, pages 157–202. John Wiley & Sons, Ltd.

Grabowski, J. H., Brumbaugh, R. D., Conrad, R. F., Keeler, A. G., Opaluch, J. J., Peterson, C. H., Piehler, M. F., Powers, S. P., and Smyth, A. R. (2012). Economic Valuation of Ecosystem Services Provided by Oyster Reefs. *BioScience*, 62(10):900–909.

Griggs, G. and Patsch, K. (2019). The Protection/Hardening of California's Coast: Times Are Changing. *Journal of Coastal Research*, 35(5):1051–1061.

Grossinger, R., Stein, E. D., Cayce, K., Askevold, R., Dark, S., and Whipple, A. (2011). Historical Wetlands of the Southern California Coast.

Grovhoug, J., Seligman, P., Vafa, G., and Fransham, R. (1986). Baseline Measurements of Butyltin in U.S. Harbors and Estuaries. In *OCEANS '86*, pages 1283–1288.

Hall, N. S., Whipple, A. C., and Paerl, H. W. (2015). Vertical spatio-temporal patterns of phytoplankton due to migration behaviors in two shallow, microtidal estuaries: Influence on phytoplankton function and structure. *Estuarine, Coastal and Shelf Science*, 162:7–21.

Hammond, R. R. and Wallace, W. J. (1982). Seabed drifter movement in San Diego Bay and adjacent waters. *Estuarine, Coastal and Shelf Science*, 14(6):623–634.

Harding, K. J., Nagarkar, M., Wang, M., Ramsing, K., Anidjar, N., Giddings, S., Brahamsha, B., and Palenik, B. (2025). Temporal and Spatial Dynamics of Synechococcus Clade II and Other Microbes in the Eutrophic Subtropical San Diego Bay. *Environmental Microbiology*, 27(2):e70043.

Harding, S. (1992). After the Neutrality Ideal: Science, Politics, and "Strong Objectivity". *Social Research*, 59(3):567–587.

Harvey, M. E., Giddings, S. N., Pawlak, G., and Crooks, J. A. (2023a). Hydrodynamic Variability of an Intermittently Closed Estuary over Interannual, Seasonal, Fortnightly, and Tidal Timescales. *Estuaries and Coasts*, 46(1):84–108.

Harvey, M. E., Giddings, S. N., Pawlak, G., and Crooks, J. A. (2023b). Hydrodynamic Variability of an Intermittently Closed Estuary over Interannual, Seasonal, Fortnightly, and Tidal Timescales. *Estuaries and Coasts*, 46(1):84–108.

Harvey, M. E., Giddings, S. N., Stein, E. D., Crooks, J. A., Whitcraft, C., Gallien, T., Largier, J. L., Tiefenthaler, L., Meltzer, H., Pawlak, G., Thorne, K., Johnston, K., Ambrose, R., Schroeter, S. C., Page, H. M., and Elwany, H. (2020). Effects of Elevated Sea Levels and Waves on Southern California Estuaries During the 2015–2016 El Niño. *Estuaries and Coasts*, 43(2):256–271.

Hearn, C. J. (1998). Application of the Stommel model to shallow Mediterranean estuaries and their characterization. *Journal of Geophysical Research: Oceans*, 103(C5):10391–10404.

Huff, A. and Brock, A. (2023). Introduction: Accumulation by restoration and political ecologies of repair. *Environment and Planning E: Nature and Space*, 6(4):2113–2133.

Jacobsen, T. R., Milutinovic, J. D., and Miller, J. R. (1990). Recruitment in Estuarine Benthic Communities: The Role of Physical Processes. In *Residual Currents and Long-Term Transport*, pages 512–525. American Geophysical Union (AGU).

Jacox, M. G., Edwards, C. A., Hazen, E. L., and Bograd, S. J. (2018). Coastal Upwelling Revisited: Ekman, Bakun, and Improved Upwelling Indices for the U.S. West Coast. *Journal of Geophysical Research: Oceans*, 123(10):7332–7350.

Jasanoff, S. (2004). Ordering Knowledge, Ordering Society. In *States of Knowledge: The Co-production of Science and the Social Order*. Routledge.

Kalansky, J., Cayan, D., Barba, K., Walsh, L., Brouwer, K., and Boudreau, D. (2018). California's Fourth Climate Change Assessment - San Diego Region Report. Technical Report SUM-CCCA4-2018-009, University of California, San Diego.

Kelleghan, D. B., O'Callaghan, L., Huggard, F., Crowe, T. P., and Brooks, P. R. (2023). Using valve gape analysis to compare sensitivity of native *Mytilus edulis* to invasive *Magallana gigas* when exposed to heavy metal contamination. *Marine Environmental Research*, 189:106043.

Kennedy, V. S., Breitburg, D. L., Christman, M. C., Luckenbach, M. W., Paynter, K., Kramer, J., Sellner, K. G., Dew-Baxter, J., Keller, C., and Mann, R. (2011). Lessons Learned from Efforts to Restore Oyster Populations in Maryland and Virginia, 1990 to 2007. *Journal of Shellfish Research*, 30(3):719–731.

Kennish, M. J., editor (2004). *Estuarine Research, Monitoring, and Resource Protection*. CRC Press.

Komoroske, L. M., Lewison, R. L., Seminoff, J. A., Deustchman, D. D., and Deheyn, D. D. (2012). Trace metals in an urbanized estuarine sea turtle food web in San Diego Bay, CA. *Science of The Total Environment*, 417–418:108–116.

Kumar, N., Voulgaris, G., Warner, J. C., and Olabarrieta, M. (2012). Implementation of the vortex force formalism in the coupled ocean-atmosphere-wave-sediment transport (COAWST) modeling system for inner shelf and surf zone applications. *Ocean Modelling*, 47:65–95.

Lagarde, F., Roque D'Orbcastel, E., Ubertini, M., Mortreux, S., Bernard, I., Fiandrino, A., Chiantella, C., Bec, B., Roques, C., Bonnet, D., Miron, G., Richard, M., Pouvreau, S., and Lett, C. (2017). Recruitment of the Pacific oyster Crassostrea gigas in a shellfish-exploited Mediterranean lagoon: Discovery, driving factors and a favorable environmental window. *Marine Ecology Progress Series*, 578:1–17.

Largier, J. (1995). San Diego Bay Circulation: A Study of the Circulation of Water in San Diego Bay for the Purpose of Assessing, Monitoring and Managing the Transport and Potential Accumulation of Pollutants and Sediment in San Diego Bay.

Largier, J. L. (2023). Recognizing Low-Inflow Estuaries as a Common Estuary Paradigm. *Estuaries and Coasts*, 46(8):1949–1970.

Largier, J. L., Hearn, C. J., and Chadwick, D. B. (1996). Density Structures in "Low Inflow Estuaries". In *Buoyancy Effects on Coastal and Estuarine Dynamics*, chapter 16, pages 227–241. American Geophysical Union (AGU).

Largier, J. L., Hollibaugh, J. T., and Smith, S. V. (1997). Seasonally Hypersaline Estuaries in Mediterranean-climate Regions. *Estuarine, Coastal and Shelf Science*, 45(6):789–797.

Lemagie, E. P., Giddings, S. N., MacCready, P., Seaton, C., and Wu, X. (2022). Measuring Estuarine Total Exchange Flow From Discrete Observations. *Journal of Geophysical Research: Oceans*, 127(10):e2022JC018960.

Lemagie, E. P. and Lerczak, J. A. (2015). A Comparison of Bulk Estuarine Turnover Timescales to Particle Tracking Timescales Using a Model of the Yaquina Bay Estuary. *Estuaries and Coasts*, 38(5):1797–1814.

Levin, L. A., Mendoza, G. F., Neira, C., Giddings, S. N., and Crooks, J. A. (2023). Consequences of Mouth Closure and Hypoxia-Induced State Changes in Low-Inflow Estuaries: Benthic Community and Trait-Based Response. *Estuaries and Coasts*, 46(8):2128–2147.

Lorenz, M., Klingbeil, K., and Burchard, H. (2020). Numerical Study of the Exchange Flow of the Persian Gulf Using an Extended Total Exchange Flow Analysis Framework. *Journal of Geophysical Research: Oceans*, 125(2):e2019JC015527.

Lorenz, M., Klingbeil, K., MacCready, P., and Burchard, H. (2019). Numerical issues of the Total Exchange Flow (TEF) analysis framework for quantifying estuarine circulation. *Ocean Science*, 15(3):601–614.

Los Peñasquitos Lagoon Foundation (2018). Los Peñasquitos Lagoon Enhancement Plan.

MacCready, P. (2011). Calculating Estuarine Exchange Flow Using Isohaline Coordinates*. *Journal of Physical Oceanography*, 41(6):1116–1124.

MacCready, P. and Geyer, W. R. (2024). Estuarine Exchange Flow in the Salish Sea. *Journal of Geophysical Research: Oceans*, 129(1):e2023JC020369.

MacCready, P., McCabe, R. M., Siedlecki, S. A., Lorenz, M., Giddings, S. N., Bos, J., Albertson, S., Banas, N. S., and Garnier, S. (2021). Estuarine Circulation, Mixing, and Residence Times

in the Salish Sea. *Journal of Geophysical Research: Oceans*, 126(2):e2020JC016738.

Marceau, F. (1909). Recherches sur la morphologie, l'histologie et la physiologie comparées de muscles adducteurs des mollusques acéphales. *Archives de zoologie experimentale et generale*.

Martin, J. (2017). San Diego's Zuniga Shoals Jetty: Icon and Enigma. *The Journal of San Diego History*, 63(3+4).

McSweeney, S. L., Kennedy, D. M., Rutherfurd, I. D., and Stout, J. C. (2017). Intermittently Closed/Open Lakes and Lagoons: Their global distribution and boundary conditions. *Geomorphology*, 292:142–152.

Meira, A., Carvalho, F., Castro, P., and Sousa, R. (2024). Applications of biosensors in non-native freshwater species: A systematic review. *NeoBiota : advancing research on alien species and biological invasions*, 96:211–236.

Meyer, D. L., Townsend, E. C., and Thayer, G. W. (1997). Stabilization and Erosion Control Value of Oyster Cultch for Intertidal Marsh. *Restoration Ecology*, 5(1):93–99.

Miller, L. P. (2022). Monitoring Bivalve Behavior and Physiology in the Laboratory and Field Using Open-Source Tools. *Integrative and Comparative Biology*, 62(4):1096–1110.

Miller, L. P. and Dowd, W. W. (2017). Multimodal in situ datalogging quantifies inter-individual variation in thermal experience and persistent origin effects on gaping behavior among intertidal mussels (*Mytilus californianus*). *Journal of Experimental Biology*, 220(22):4305–4319.

Mistry, J. and Berardi, A. (2016). Bridging indigenous and scientific knowledge. *Science*, 352(6291):1274–1275.

Mladenov, N., Biggs, T., Ford, K., Garcia, S., Yuan, Y., Grant, A., Piazza, E., Rivera, E., Pinongcos, F., Keely, S. P., Summerlin, C., Crooks, J. A., and Liden, D. (2024). Evaluation of real-time fluorescence sensors and benchtop fluorescence for tracking and predicting sewage contamination in the Tijuana River Estuary at the US-Mexico border. *Science of The Total Environment*, 950:175137.

Moranta, J., Torres, C., Murray, I., Hidalgo, M., Hinz, H., and Gouraguine, A. (2022). Transcending capitalism growth strategies for biodiversity conservation. *Conservation Biology*, 36(2):e13821.

Nader, L. (1972). Up the Anthropologist: Perspectives Gained From Studying Up. Technical report.

National Research Council (1990). *Monitoring Southern California's Coastal Waters*. National Academies Press, Washington, D.C.

Neira, C., Vales, M., Mendoza, G., Hoh, E., and Levin, L. A. (2018). Polychlorinated biphenyls (PCBs) in recreational marina sediments of San Diego Bay, southern California. *Marine Pollution Bulletin*, 126:204–214.

Nidzieko, N. J. and Monismith, S. G. (2013). Contrasting Seasonal and Fortnightly Variations in the Circulation of a Seasonally Inverse Estuary, Elkhorn Slough, California. *Estuaries and Coasts*, 36(1):1–17.

Norris, J., Hall, A., Chen, D., Thackeray, C. W., and Madakumbura, G. D. (2021). Assessing the Representation of Synoptic Variability Associated With California Extreme Precipitation in CMIP6 Models. *Journal of Geophysical Research: Atmospheres*, 126(6):e2020JD033938.

Novoa, A., Talley, T. S., Talley, D. M., Crooks, J. A., and Reyns, N. B. (2016). Spatial and Temporal Examination of Bivalve Communities in Several Estuaries of Southern California and Northern Baja California, MX. *PLOS ONE*, 11(2):e0148220.

O'Beirn, F. X., Heffernan, P. B., and Walker, R. L. (1995). Preliminary recruitment studies of the eastern oyster, *Crassostrea virginica*, and their potential applications, in coastal Georgia. *Aquaculture (Amsterdam, Netherlands)*, 136(3):231–242.

O'Donnell, E. (2023). Water sovereignty for Indigenous Peoples: Pathways to pluralist, legitimate and sustainable water laws in settler colonial states. *PLOS Water*, 2(11):e0000144.

Orescanin, M. M. and Scooler, J. (2018). Observations of episodic breaching and closure at an ephemeral river. *Continental Shelf Research*, 166:77–82.

Ortega, S. and Sutherland, J. P. (1992). Recruitment and growth of the Eastern oyster, Crassostrea virginica, in North Carolina. *Estuaries*, 15(2):158–170.

Padilla, D. K. (2010). Context-dependent Impacts of a Non-native Ecosystem Engineer, the Pacific Oyster Crassostrea gigas. *Integrative and Comparative Biology*, 50(2):213–225.

Peeling, T. J. (1975). A Proximate Biological Survey of San Diego Bay, California.

Perog, B., Bowers-Doerning, C., Wolfe, M., and Zacherl, D. (2022). Bay-wide abundance estimates of native (*Ostrea lurida*) and nonnative (*Magallana gigas*) oysters in San Diego Bay, CA.

Perog, B. D., Bowers-Doerning, C., Lopez Ramirez, C. Y., Marks, A. N., Torres Jr., R. F., Wolfe, M. L., and Zacherl, D. C. (2023). Shell cover, rugosity, and tidal elevation impact native and non-indigenous oyster recruitment: Implications for reef ball design. *Ecological Engineering*, 192:106969.

Piazza, B. P., Banks, P. D., and La Peyre, M. K. (2005). The Potential for Created Oyster

Shell Reefs as a Sustainable Shoreline Protection Strategy in Louisiana. *Restoration Ecology*, 13(3):499–506.

Pierce, K. A., Nelson, D. P., and Leue, M. C. (2001). Deepening of the San Diego Harbor & Study to Remove UXO from Large Quantities of Dredge Spoils. pages 1–10.

Planning and Environment Division (2024). Port Master Plan. Technical Report 76469, San Diego Unified Port District.

Port of San Diego (1980). Environmental impact report on master plan, San Diego Unified Port District final environmental impact report. Technical report.

Porter, E. T. and Breitburg, D. L. (2016). Eastern oyster, *Crassostrea virginica*, valve gape behavior under diel-cycling hypoxia. *Marine Biology*, 163(10):218.

Pratt, J. (2014). California Inlets: A Coastal Management "No Man's Land". Technical report, Surfrider Foundation.

Pritchard, C., Shanks, A., Rimler, R., Oates, M., and Rumrill, S. (2015). The Olympia Oyster *Ostrea lurida* : Recent Advances in Natural History, Ecology, and Restoration. *Journal of Shellfish Research*, 34(2):259–271.

Rasmussen, L. L., Carter, M. L., Flick, R. E., Hilbern, M., Fumo, J. T., Cornuelle, B. D., Gordon, B. K., Bargatze, L. F., Gordon, R. L., and McGowan, J. A. (2020). A Century of Southern California Coastal Ocean Temperature Measurements. *Journal of Geophysical Research: Oceans*, 125(5):e2019JC015673.

Ridlon, A. D., Marks, A., Zabin, C. J., Zacherl, D., Allen, B., Crooks, J., Fleener, G., Grosholz, E., Peabody, B., Toft, J., and Wasson, K. (2021). Conservation of Marine Foundation Species: Learning from Native Oyster Restoration from California to British Columbia. *Estuaries and Coasts*, 44(7):1723–1743.

Robertson, M. M. (2000). No Net Loss: Wetland Restoration and the Incomplete Capitalization of Nature. *Antipode*, 32(4):463–493.

Robinson, J. M., Gellie, N., MacCarthy, D., Mills, J. G., O'Donnell, K., and Redvers, N. (2021). Traditional ecological knowledge in restoration ecology: A call to listen deeply, to engage with, and respect Indigenous voices. *Restoration Ecology*, 29(4):e13381.

Rodriguez, A. R. (2019). *Buoyancy Transport Mechanisms at Continental Shelf, Surf Zone, and Estuarine Scales*. PhD thesis, UC San Diego.

Roegner, G. C. (2000). Transport of molluscan larvae through a shallow estuary. *Journal of Plankton Research*, 22(9):1779–1800.

Roegner, G. C., Diefenderfer, H. L., Borde, A. B., Thom, R. M., Dawley, E. M., Whiting, A. H., Zimmerman, S. A., and Johnson, G. E. (2008). Protocols for Monitoring Habitat Restoration Projects in the Lower Columbia River and Estuary. Technical Report PNNL-15793, 927720.

Rouleau, T., Colgan, C., Adkins, J., Anthony, C., Patty, D., Lyons, S., and Stevens, H. (2021). The Economic Value of America's Estuaries: 2021 Report. *Publications*.

Ruesink, J. L., Lenihan, H. S., Trimble, A. C., Heiman, K. W., Micheli, F., Byers, J. E., and Kay, M. C. (2005). Introduction of Non-Native Oysters: Ecosystem Effects and Restoration Implications. *Annual Review of Ecology, Evolution, and Systematics*, 36(Volume 36, 2005):643–689.

San Diego Unified Port District and City of Chula Vista (2016). Chula Vista Bayfront Master Plan Natural Resources Management Plan. https://pantheonstorage.blob.core.windows.net/ceqa/Chula-Vista-Bayfront-Master-Plan-Natural-Resources-Management-Plan.pdf.

SANDAG (2025). San Diego LOSSAN Rail Realignment Project Final Value Analysis Study Report.

Sanjeeva Raj, P. J. (2008). Oysters in a new classification of keystone species. *Resonance*, 13(7):648–654.

Sarabia, H., Alo, T., Quetin, L., and Boyd, D. (2024). San Diego Bay Sediment Pollutants: Evaluation of Contemporary Ambient Concentrations to Inform Water Quality Management. Technical report.

Scheffer, M., Carpenter, S., Foley, J. A., Folke, C., and Walker, B. (2001). Catastrophic shifts in ecosystems. *Nature*, 413(6856):591–596.

Schettini, C. A. F., Valle-Levinson, A., and Truccolo, E. C. (2017). Circulation and transport in short, low-inflow estuaries under anthropogenic stresses. *Regional Studies in Marine Science*, 10:52–64.

Schiff, K. and Carter, S. (2007). Monitoring and Modeling of Chollas, Paleta, and Switzer Creeks. Technical Report 513, Southern California Coastal Water Research Project and Tetra Tech, Inc.

Schulte, D. M. and Burke, R. P. (2014). Recruitment Enhancement as an Indicator of Oyster Restoration Success in Chesapeake Bay. *Ecological Restoration*, 32(4):434–440.

Seale, E. M. and Zacherl, D. C. (2009). Seasonal Settlement of Olympia Oyster Larvae, Ostrea lurida Carpenter 1864 and Its Relationship to Seawater Temperature in Two Southern California Estuaries. *Journal of Shellfish Research*, 28(1):113–120.

Senos, R., Lake, F. K., Turner, N., and Martinez, D. (2006). Traditional Ecological Knowledge and Restoration Practice. In *Restoring the Pacific Northwest: The Art and Science of Ecological Restoration in Cascadia*.

Shatkin, G., Shumway, S., and Hawes, R. (1997). Considerations regarding the possible introduction of the Pacific oyster, Crassostrea gigas, to the Gulf of Maine: A review of global experience. *Journal of Shellfish Research*, 16:463–478.

Shchepetkin, A. F. and McWilliams, J. C. (2005). The regional oceanic modeling system (ROMS): A split-explicit, free-surface, topography-following-coordinate oceanic model. *Ocean Modelling*, 9(4):347–404.

Shrestha, P. L., Orlob, G. T., and King, I. P. (1997). Comparison of one- and two-dimensional models for simulation of hydrodynamics and water quality in shallow bays. *Journal of Environmental Science and Health . Part A: Environmental Science and Engineering and Toxicology*, 32(4):979–999.

Siedlecki, S. A., Pilcher, D., Howard, E. M., Deutsch, C., MacCready, P., Norton, E. L., Frenzel, H., Newton, J., Feely, R. A., Alin, S. R., and Klinger, T. (2021). Coastal processes modify projections of some climate-driven stressors in the California Current System. *Biogeosciences (Online)*, 18(9):2871–2890.

Simons, R. D., Siegel, D. A., and Brown, K. S. (2013). Model sensitivity and robustness in the estimation of larval transport: A study of particle tracking parameters. *Journal of Marine Systems*, 119–120:19–29.

Skelton, Z. R., McCormick, L. R., Kwan, G. T., Lonthair, J., Neira, C., Clements, S. M., Martz, T. R., Bresnahan, P. J., Send, U., Giddings, S. N., Sevadjian, J. C., Jaeger, S., Feit, A., Frable, B. W., Zerofski, P. J., Torres, M., Crooks, J. A., McCullough, J., Carter, M. L., Ternon, E., Miller, L. P., Kalbach, G. M., Wheeler, D. C., Parnell, P. E., Swiney, K. M., Seibert, G., Minich, J. J., Hyde, J. R., Hastings, P. A., Smith, J. E., Komoroske, L. M., Tresguerres, M., Levin, L. A., and Wegner, N. C. (2024). Organismal responses to deteriorating water quality during the historic 2020 red tide off Southern California. *Elementa: Science of the Anthropocene*, 12(1):00067.

Smith, R. R. (2018). Application for Corps Mitigation Bank & Prospectus Review Port of San Diego - South San Diego Bay Pond 20 Wetland Mitigation Bank.

Smythe, W. E. (1908). Part Seven - Chapter Two - San Diego Bay, Harbor, and River. In *History of San Diego, 1542-1908*.

Sorensen, K., Swope, B., and Kirtay, V. (2013). Marine Ecological Index Survey of San Diego Bay.

Southern California Wetlands Recovery Project (2018). Wetlands on the Edge: The Future of Southern California's Wetlands: Regional Strategy 2018. Technical report, California State Coastal Conservancy.

Sponaugle, S., Cowen, R. K., Shanks, A., Morgan, S. G., and Leis, J. M. (2002). Predicting self-recruitment in marine populations: Biophysical correlates and mechanisms. *Bulletin of Marine Sceince*, 70(1).

Stacey, M. T., Burau, J. R., and Monismith, S. G. (2001). Creation of residual flows in a partially stratified estuary. *Journal of Geophysical Research: Oceans*, 106(C8):17013–17037.

Stein, E. D., Cayce, K., Salomon, M., Liza, D., Mello, D. D., Grossinger, R., and Dark, S. (2014). Wetlands of the Southern California Coast – Historical Extent and Change Over Time.

Stimson, H. L. (1941). San Diego Harbor, Calif. - Letter from the secretary of war.

Sugihara, G. (1994). Nonlinear forecasting for the classification of natural time series. *Philosophical Transactions of the Royal Society of London. Series A: Physical and Engineering Sciences*.

Sugihara, G., May, R., Ye, H., Hsieh, C.-h., Deyle, E., Fogarty, M., and Munch, S. (2012). Detecting Causality in Complex Ecosystems. *Science*, 338(6106):496–500.

Sugihara, G. and May, R. M. (1990). Nonlinear forecasting as a way of distinguishing chaos from measurement error in time series. *Nature*, 344(6268):734–741.

Sylman, S., Steen, M., Stevens, L., Lyles, W., and Deer, S. (2026). Planning for Land Back: An empirical examination of the Land Back Movement with implications for land use and environmental planning. *Frontiers in Sustainable Resource Management*, 5:1783142.

Taherkhani, M., Vitousek, S., Walter, R. K., O'Leary, J., and Khodadoust, A. P. (2023). Flushing time variability in a short, low-inflow estuary. *Estuarine, Coastal and Shelf Science*, 284:108277.

Tedford-Callahan, K. N., Smith, R. S., Lusk, B. W., and Castorani, M. C. N. (2025). Hydrodynamics, elevation, and restoration history structure intertidal oyster recruitment. *Landscape Ecology*, 40(6):114.

Thode, H. C. (2002). *Testing for Normality*. Number v. 164 in Statistics, Textbooks and Monographs. Marcel Dekker, New York.

Thornton, T. F. and Scheer, A. M. (2012). Collaborative Engagement of Local and Traditional Knowledge and Science in Marine Environments: A Review. *Ecology and Society*, 17(3):art8.

Torres, T. (2024). California 2024 303d List EPA Partial Approval Disapproval. Technical report.

Touchstone, V., Crooks, J., Nordby, C., and Toomey, E. (2021). South San Diego Bay Coastal Wetland Restoration and Enhancement Project - Restoring the Western Salt Ponds. Technical report, Southwest Wetlands Interpretative Association.

Tran, D., Fournier, E., Durrieu, G., and Massabuau, J.-C. (2004). Copper detection in the Asiatic clam *Corbicula fluminea*: Optimum valve closure response. *Aquatic Toxicology*, 66(3):333–343.

Tran, D., Fournier, E., Durrieu, G., and Massabuau, J.-C. (2007). Inorganic mercury detection by valve closure response in the freshwater clam *Corbicula fluminea*: Integration of time and water metal concentration changes. *Environmental Toxicology and Chemistry*, 26(7):1545–1551.

Tran, D., Haberkorn, H., Soudant, P., Ciret, P., and Massabuau, J.-C. (2010). Behavioral responses of *Crassostrea gigas* exposed to the harmful algae Alexandrium minutum. *Aquaculture (Amsterdam, Netherlands)*, 298(3):338–345.

Tran, D., Nadau, A., Durrieu, G., Ciret, P., Parisot, J.-P., and Massabuau, J.-C. (2011). Field Chronobiology of a Molluscan Bivalve: How the Moon and Sun Cycles Interact to Drive Oyster Activity Rhythms. *Chronobiology International*, 28(4):307–317.

Tronske, N. B., Parker, T. A., Henderson, H. D., Burnaford, J. L., and Zacherl, D. C. (2018). Densities and Zonation Patterns of Native and Non-Indigenous Oysters in Southern California Bays. *Wetlands*, 38(6):1313–1326.

Tuck, E. and Yang, K. W. (2012). Decolonization is not a metaphor. *Decolonization: Indigeneity, Education & Society*, 1(1):1–40.

U. S. Department of the Navy (2024). Final Environmental Assessment for Eelgrass Habitat Expansion in San Diego Bay, California. https://media.defense.gov/2024/Aug/28/2003534386/-1/-1/0/SD%20BAY%20EELGRASS%20FINAL%20EA-FONSI_22AUG2024_508.PDF.

Uncles, R. J., Stephens, J. A., and Smith, R. E. (2002). The dependence of estuarine turbidity on tidal intrusion length, tidal range and residence time. *Continental Shelf Research*, 22(11):1835–1856.

Unified Port of San Diego (2010). Chula Vista Bayfront Master Plan: Final Environmental Impact Report. Technical report.

U.S. Congress (1968). 90th Congress 2nd Session Serial Set Vol. No. 128156 Session Vol. No. 11-6 H.Doc. 365.

U.S. Department of the Navy, Naval Facilities Engineering Command Southwest and Port of

San Diego (2013). San Diego Bay Integrated Natural Resources Management Plan. Technical report, Tierra Data Inc., San Diego, CA, USA.

U.S. Navy (2013a). Integrated Natural Resources Management Plan: Naval Base Coronado, California. Technical report.

U.S. Navy (2013b). San Diego Bay Integrated Natural Resources Management Plan. Technical report.

Valdez, S. R. and Ruesink, J. L. (2017). Scales of recruitment variability in warming waters: Comparing native and introduced oysters in Hood Canal, Washington, USA. *Marine Ecology*, 38(3):e12435.

Vereycken, J. E. and Aldridge, D. C. (2023). Bivalve molluscs as biosensors of water quality: State of the art and future directions. *Hydrobiologia*, 850(2):231–256.

Wagner, H. R. (1929). *Spanish Voyages to the Northwest Coast of America*. California Historical Society.

Walker, J. B., O'Connor, K., Wasson, K., Crain, C., Johnston, K. K., Ambrose, R. F., Whitcraft, C. R., Crooks, J. A., Beheshti, K., Hall, M., Nichols, K., Clemens, M., and Stein, E. D. (2025). Sentinel site networks as a mechanism to evaluate progress toward meeting restoration goals in altered and unaltered landscapes. *Restoration Ecology*, 33(5):e70062.

Wallace, A. (2023). *Assessing the Effectiveness of Integrated Multi-Trophic Aquaculture for Growing West Coast Venus Clams*. PhD thesis, University of San Diego.

Walter, R. K., Rainville, E. J., and O'Leary, J. K. (2018). Hydrodynamics in a shallow seasonally low-inflow estuary following eelgrass collapse. *Estuarine, Coastal and Shelf Science*, 213:160–175.

Wang, P. F., Cheng, R. T., Richter, K., Gross, E. S., Sutton, D., and Gartner, J. W. (1998). Modeling Tidal Hydrodynamics of San Diego Bay, California. *JAWRA Journal of the American Water Resources Association*, 34(5):1123–1140.

Wang, P.-F., Liao, Q., George, R., and Wild, W. (2011). Release Rate and Transport of Munitions Constituents from Breached Shells in Marine Environment. In *Environmental Chemistry of Explosives and Propellant Compounds in Soils and Marine Systems: Distributed Source Characterization and Remedial Technologies*, volume 1069 of *ACS Symposium Series*, chapter 16, pages 317–340. American Chemical Society.

Warner, J. C., Armstrong, B., He, R., and Zambon, J. B. (2010). Development of a Coupled Ocean–Atmosphere–Wave–Sediment Transport (COAWST) Modeling System. *Ocean Modelling*, 35(3):230–244.

Wasson, K., Hughes, B. B., Berriman, J. S., Chang, A. L., Deck, A. K., Dinnel, P. A., Endris, C., Espinoza, M., Dudas, S., Ferner, M. C., Grosholz, E. D., Kimbro, D., Ruesink, J. L., Trimble, A. C., Vander Schaaf, D., Zabin, C. J., and Zacherl, D. C. (2016). Coast-wide recruitment dynamics of Olympia oysters reveal limited synchrony and multiple predictors of failure. *Ecology*, 97(12):3503–3516.

Wasson, K., Zabin, C., Bible, J., Briley, S., Ceballos, E., Chang, A., Cheng, B., Deck, A., Grosholz, T., Helms, A., Latta, M., Yednock, B., Zacherl, D., and Ferner, M. (2015). A Guide to Olympia Oyster Restoration and Conservation. Technical report, Elkhorn Slough National Estuarine Research Reserve.

Water Resources Control Board State of California (1990). 305(b) Water Quality Report for Water Years 1988 and 1989. Technical report.

Wickliffe, L. C., Jossart, J. A., Theuerkauf, S. J., Jensen, B. M., King, J. B., Henry, T., Sylvia, P. C., Morris, J. A., and Riley, K. L. (2024). Balancing conflict and opportunity - spatial planning of shellfish and macroalgae culture systems in a heavily trafficked maritime port. *Frontiers in Marine Science*, 10:1294501.

Williams, B. K., Szaro, R. C., and Shapiro, C. D. (2009). Adaptive Management: The U.S. Department of the Interior Technical Guide.

Williams, G. D. and Zedler, J. B. (1999). Fish assemblage composition in constructed and natural tidal marshes of San Diego Bay: Relative influence of channel morphology and restoration history. *Estuaries*, 22(3):702–716.

Willmott, C. J. (1981). On the Validation of Models. *Physical Geography*, 2(2):184–194.

Wilson, R., Reuter, P., and Wahl, M. (2005). Muscling in on mussels: New insights into bivalve behaviour using vertebrate remote-sensing technology. *Marine Biology*, 147(5):1165–1172.

Wolanski, E. (1986). An evaporation-driven salinity maximum zone in Australian tropical estuaries. *Estuarine, Coastal and Shelf Science*, 22(4):415–424.

Wolfe, M. L., Bowers-Doerning, C. M., Espinosa, A., Frantz, T., Hoese, W. J., Lam, J. G., Lamp, K. R., Lyons, R. A., Nguyen, J. K., Keyes, B. D., Smith, J., Suther, H. L., Swintek, M., Vannordstrand, J. C., and Zacherl, D. C. (2024). Intra-decadal increase in globally-spread Magallana gigas in southern California estuaries. *PLOS ONE*, 19(5):e0302935.

Wu, X., Feddersen, F., and Giddings, S. N. (2021a). Automated Temporal Tracking of Coherently Evolving Density Fronts in Numerical Models.

Wu, X., Feddersen, F., and Giddings, S. N. (2021b). Characteristics and Dynamics of Density Fronts over the Inner to Midshelf under Weak Wind Conditions.

Wu, X., Feddersen, F., and Giddings, S. N. (2021c). Diagnosing Surfzone Impacts on Inner-Shelf Flow Spatial Variability Using Realistic Model Experiments with and without Surface Gravity Waves.

Wu, X., Feddersen, F., Giddings, S. N., Kumar, N., and Gopalakrishnan, G. (2020). Mechanisms of Mid- to Outer-Shelf Transport of Shoreline-Released Tracers. *Journal of Physical Oceanography*, 50(7):1813–1837.

Xiu, P., Chai, F., Curchitser, E. N., and Castruccio, F. S. (2018). Future changes in coastal upwelling ecosystems with global warming: The case of the California Current System. *Scientific Reports*, 8(1):2866.

Zaba, K. D., Rudnick, D. L., Cornuelle, B. D., Gopalakrishnan, G., and Mazloff, M. R. (2018). Annual and Interannual Variability in the California Current System: Comparison of an Ocean State Estimate with a Network of Underwater Gliders.

Zacherl, D. C., Moreno, A., and Crossen, S. (2015). Exploring Restoration Methods for the Olympia Oyster Ostrea lurida Carpenter, 1864: Effects of Shell Bed Thickness and Shell Deployment Methods on Shell Cover, Oyster Recruitment, and Oyster Density. *Journal of Shellfish Research*, 34(3):819–830.

Zedler, J. B. and Callaway, J. C. (2000). Evaluating the progress of engineered tidal wetlands. *Ecological Engineering*, 15(3):211–225.

Zedler, J. B. and Stevens, M. L. (2018). Western and Traditional Ecological Knowledge in Ecocultural Restoration. *San Francisco Estuary and Watershed Science*, 16(3).